

PROBING THE REACTION MECHANISM OF METHYL COENZYME M  
REDUCTASE

Except where reference is made to the work of others, the work described in this dissertation is my own or was done in collaboration with my advisory committee. This dissertation does not include proprietary or classified information.

---

Mi Wang

Certificate of Approval:

---

Edward J. Parish  
Professor  
Chemistry and Biochemistry

---

Evert C. Duin, Chair  
Assistant Professor  
Chemistry and Biochemistry

---

Douglas C. Goodwin  
Associate Professor  
Chemistry and Biochemistry

---

Holly R. Ellis,  
Associate Professor  
Chemistry and Biochemistry

---

Joe F. Pittman  
Interim Dean  
Graduate School

PROBING THE REACTION MECHANISM OF METHYL COENZYME M  
REDUCTASE

Mi Wang

A Dissertation

Submitted to

the Graduate Faculty of

Auburn University

in Partial Fulfillment of the

Requirements for the

Degree of

Doctor of Philosophy

Auburn, Alabama  
August 9, 2008

PROBING THE REACTION MECHANISM OF METHYL COENZYME M  
REDUCTASE

Mi Wang

Permission is granted to Auburn University to make copies of this dissertation at its discretion, upon request of individuals or institutions and at their expense. The author reserves all publication rights.

---

Signature of Author

---

Date of Graduation

## VITA

Mi Wang, Son of Ji Wang and Guizhen Qin, was born on October 17, 1979, in Zhenjiang, Jiangsu Province, the People's Republic of China. He graduated with a Bachelor's degree in Biochemical Engineering in 2000 from Nanjing University of Technology. From 2000 to 2002, he entered the Graduate School at Nanjing University of Technology in College of Life Science and Pharmaceutical Engineering. In fall 2002, he entered the Graduate School at Auburn University in the Department of Chemistry and Biochemistry and is currently pursuing the Ph.D degree.

## DISSERTATION ABSTRACT

### PROBING THE REACTION MECHANISM OF METHYL COENZYME M REDUCTASE

Mi Wang

Doctor of Philosophy, August 9, 2008  
(B.S., Nanjing University of Technology, 2000)

194 Typed Pages

Directed by Evert C. Duin

Methyl coenzyme M reductase (MCR) is the key enzyme in both microbial methane production and anaerobic methane oxidation. MCR catalyzes the reaction of methyl-coenzyme M ( $\text{CH}_3\text{-SCoM}$ ) and coenzyme B ( $\text{HS-CoB}$ ) to methane and the corresponding heterodisulfide  $\text{CoM-S-S-CoB}$ . MCR is a large heterohexameric protein complex  $(\alpha\beta\gamma)_2$  containing two 50 Å long active sites channels. Central to this activity is the nickel-containing tetrapyrrole factor 430 ( $\text{F}_{430}$ ). Coenzyme  $\text{F}_{430}$  is embedded at the channel bottom and the substrates  $\text{CH}_3\text{-S-CoM}$  and  $\text{HS-CoB}$  bind in front of  $\text{F}_{430}$  into a solvent free and hydrophobic channel. Two principally different catalytic mechanisms are currently discussed. Mechanism I is based on a nucleophilic attack of Ni(I) onto the methyl group of  $\text{CH}_3\text{-SCoM}$  yielding methyl-Ni(III) and mechanism II on an attack of

Ni(I) onto the thioether sulfur of  $\text{CH}_3\text{-SCoM}$  generating a Ni(II)-SCoM intermediate. However, both mechanisms have been criticized because the forming Ni-Me bond is much weaker than the breaking S-Me bond (in  $\text{CH}_3\text{-SCoM}^-$ ), which would make that step in the cycle unrealistic. Recently there is a new DFT-based mechanism proposed. This mechanism the full  $\text{F}_{430}$  cofactor of MCR along with a coordinated  $\text{O}=\text{CH}_2\text{CH}_2\text{C}(\text{H})\text{NH}_2\text{C}(\text{H})\text{O}$  (surrogate for glutamine) as a model of the active site for conversion of  $\text{CH}_3\text{SCoM}^-$  ( $\text{CH}_3\text{SCH}_2\text{CH}_2\text{SO}_3^-$ ) and HSCoB to methane plus the corresponding heterodisulfide.

We studied on the interaction of MCR with bromo-alkyl compounds that inhibit the enzyme. X-ray absorption and ENDOR studies show the presence of a Ni-C bond after incubation with bromomethane (BrMe), bromomethane (BES) and 3-bromopropane sulfonate (BPS). In addition we showed that the geometry around the nickel becomes highly asymmetric when the propyl-sulfonate group is bound to the nickel. We studied on heterodisulfide. Data shows that back reaction is present. These are in line with the new DFT-based mechanism that predicts that the nickel atom protrudes from the tetrapyrrole plane during the reaction.

## ACKNOWLEDGEMENTS

I would like to firstly express my deepest appreciation to my advisor, Dr. Evert C. Duin, for his consistent support and invaluable academic guidance. My dissertation would not be possible without his support and guidance. Secondly, I would like to thank my knowledgeable committee members, Dr. Holly Ellis Dr. Edward Parish and Dr. Douglas Goodwin for their constructive comments. I also want to thank my lab colleagues, Dr. Dolapo Adedeji, Dr. Na Yang, and Weiya Xu for their meaningful discussions and help. I also give my thanks to my many friends not only in Auburn but also across the U.S. for their kindly help to me during my graduate study here. Last but not least, I want to thank the Department of Chemistry and Biochemistry, Auburn University for their financial support of my research.

Style manual used: Biochemical and Biophysical Research Communications

Computer software used: Microsoft Word, ChemDraw, Microsoft Excel, Origin,

Endnote

## TABLE OF CONTENTS

LIST OF TABLE.....	xiv
LIST OF FIGURES .....	xv
CHAPTER ONE LITERATURE REVIEW.....	1
1.1 Methane.....	1
1.2 Methanogens.....	2
1.3 Methanogenesis.....	4
1.4 Nickel Enzymes.....	7
1.5 Methyl Coenzyme M Reductase.....	9
1.5.1 Structural properties of the enzyme.....	9
1.5.2 In Vitro Assays.....	14
1.5.3 Substrate Analogs and Inhibitors.....	16
1.5.4 Structure and Properties of Coenzyme F <sub>430</sub> .....	18
1.5.5 EPR Studies of different MCR forms.....	19

1.5.6 XAS Studies of different MCR forms.....	24
1.5.7 The Activation Cycle of Methyl-Coenzyme M Reductase.....	27
1.5.8 Anaerobic Oxidation of Methane (AOM).....	29
1.5.9 Catalytic Mechanism of MCR.....	30
1.5.10 MCRred2, the key to understanding the catalytic mechanisms of MCR?.....	37
CHAPTER TWO ANALYTICAL TECHNIQUES.....	41
2.1 Electron Paramagnetic Resonance spectroscopy.....	41
2.1.1 Introduction and Background.....	41
2.1.2 Basic Principles.....	44
2.2 Electron Nuclear Double Resonance Spectroscopy .....	59
2.3 X-ray Absorption Spectroscopy.....	64
CHAPTER THREE MATERIALS AND METHODS.....	73
3.1 Biochemical and Chemical Reagents.....	73
3.2 Synthesis and Purification of 2-methylthioethane sulfonate	

(Methyl-coenzyme M).....	74
3.3 Synthesis of (+)-(2 <i>S</i> ,3 <i>R</i> )- <i>N</i> -[7-Mercaptoheptanoyl]- <i>O</i> -phospho-L-threonine	
(Coenzyme B) .....	75
3.3.1 7, 7'-Dithioheptanoic Acid.....	75
3.3.2 7,7'-Dithiobis (succinimido-oxyheptanoate) .....	78
3.3.3 (+)- <i>N,N'</i> -(7,7'-Dithio-diheptanyl) bis ( <i>O</i> -phospho-L-threonine).....	79
3.3.4 (+)-(2 <i>S</i> ,3 <i>R</i> )- <i>N</i> -[7-Mercaptoheptanoyl]- <i>O</i> -phospho-L-threonine.....	80
3.3.5 Determination of the Concentration of Coenzyme B.....	83
3.4 Synthesis of CoM-S-S-CoB.....	84
3.5 Purification of MCR.....	85
3.6 Induction of the MCRred1 forms in whole cells.....	86
3.7 Protein Determination.....	87
3.8 Activity Assay.....	87
3.9 EPR Experiments .....	88
3.10 ENDOR measurements.....	89

3.11 UV-visible spectroscopy.....	89
3.12 X-ray absorption spectroscopy.....	90
3.13 Assays for Bromide.....	92
3.14 Anaerobic saturated BrCH <sub>3</sub> solution.....	92
CHAPTER FOUR RESULTS.....	93
4.1 Purification of MCR .....	93
4.1.1 Induction of the MCRred1 Form.....	96
4.1.2 Activity Assay .....	98
4.2 Observations on MCR Made under Turnover Conditions.....	100
4.3 Using labeling studies to detect the positions of selected atoms of substrates and analogs that are bound in the active site of MCR.....	104
4.4 Studies with Bromo-alkyl Compounds.....	109
4.4.1 EPR Studies with Bromomethane (BrMe).....	111
4.4.2 Stability of the MCR-BrMe Form.....	114
4.4.3 Reactivity of the MCR-BrMe form.....	115

4.4.4 Studies with BPS.....	119
4.4.5 Studies with 2-Bromoethanesulfonate (BES).....	123
4.5 X-ray Absorption Spectroscopy Measurements on the MCR-BPS, MCR-BES and MCR-BrMe Forms.....	128
4.6 Detection of Bromide.....	136
4.7 ENDOR results of radical in MCR-BES.....	138
4.8 Effect of other substrate analogs on the red1 and red2 forms of MCR.....	140
CHAPTER FIVE DISCUSSION AND CONCLUSION.....	145
5.1 Studies with Bromo-alkyl Species.....	145
5.2 Origin of the radical species.....	149
5.3 Effect of coenzyme B.....	153
5.4 A new mechanism.....	157
REFERENCES .....	162

## LIST OF TABLES

Table 1-1: Substrate Analogs for Methyl Coenzyme M Reductase.....	17
Table 1-2: Inhibitors of Methyl Coenzyme M Reductase.....	17
Table 3-1: XAS samples.....	91
Table 2-1: Nuclear spin of some nuclei that are important for the research presented in this dissertation .....	57
Table 5-1: Comparison of g-Values and Isotropic Hyperfine Values of the RNR, PFL, and BSS Glycyl Radical with Those of the N-Acetyl Glycine Radical, Tyrosyl Radical, and Tryptophan Radical.....	151
Table 5-2: <sup>14</sup> N hyperfine parameters of the pyrrole nitrogens of F <sub>430</sub> of MCRred1 and MCRred2.....	154

## LIST OF FIGURES

Figure 1-1: Hydrogenotrophic Pathway of Methanogenesis.....	5
Figure 1-2: Coenzymes used in the hydrogenotrophic pathway.....	6
Figure 1-3: Crystal structure of MCR.....	10
Figure 1-4: Crystal structure of the active site channel of MCR.....	11
Figure 1-5: Schematic representation of the active-site channels.....	13
Figure 1-6: EPR spectra of the pentamethylester form of $F_{430}(F_{430}M)$ in different oxidation states .....	20
Figure 1-7: EPR spectra of methyl-coenzyme M reductase in different forms.....	21
Figure 1-8: X-ray absorption spectra of MCR.....	26
Figure 1-9: Conversion cycle between three forms of MCR.....	28
Figure 1-10: Hypothetical mechanism model I .....	32
Figure 1-11: Hypothetical mechanism model Ib.....	34

Figure 1-12: Hypothetical mechanism model II .....	35
Figure 1-13: Induction of the red2 form with different coenzyme B analogs .....	39
Figure 1-14: Induction of the red2 form with coenzyme B analogs .....	40
Figure 2-1: Schematic representation of a continuous-wave EPR spectrometer .....	43
Figure 2-2: Minimum and maximum energy orientations of $\mu$ with respect to the magnetic field $B_0$ .....	46
Figure 2-3: Induction of the spin state energies as a function of the magnetic field $B_0$ .....	47
Figure 2-4: Schematic illustration of the splitting of the electron spin states with absorption and first-order derivative .....	49
Figure 2-5: A paramagnetic metal molecule coordinated by two equal ligands in the z direction and two different but equal ligands in both the x and y directions .....	51
Figure 2-6: The basic spectral envelopes to be found with $S = 1/2$ paramagnets.....	53

Figure 2-7: Permanent local fields arising from the magnetic moments of magnetic nuclei ( $I=1/2$ ) .....	54
Figure 2-8: EPR experiment for a single electron interacting with a magnetic nucleus with nuclear spin ( $I=1/2$ ) .....	55
Figure 2-9: EPR spectra of methyl-coenzyme M from <i>Methanothemobacter marburgensis</i> in the red1 state.....	58
Figure 2-10: The effect of electronic and nuclear Zeeman interactions and of the hyperfine interaction.....	61
Figure 2-11: An X-ray absorption spectrum plotted as absorption coefficient versus photon energy.....	65
Figure 2-12: Schematic diagram relating the X-ray absorption spectrum to the atomic energy level diagram.....	67
Figure 2-13: Example of data reduction for EXAFS analysis.....	69
Figure 2-14: Comparison of Ni K X-ray absorption edge spectra for a series of Ni(II) compounds of varying site symmetry.....	72

Figure 3-1: NMR spectra of methyl-coenzyme M. ....	76
Figure 3-2: NMR spectra of coenzyme B.....	82
Figure 4-1: Growth curve of <i>Methanothermobacter marburgensis</i> grown in 10 L medium at 65°C.....	94
Figure 4-2: SDS-PAGE of MCR in different stages of the purification.....	95
Figure 4-3: Time dependency of the induction of the MCRred1 and MCRred2 forms by changing the gas phase to 100% hydrogen gas.....	97
Figure 4-4: Activity assay of MCRred1.....	99
Figure 4-5: Change in EPR spectra detected for MCR under turn-over conditions. ....	102
Figure 4-6: Effect of different concentration of heterodisulfide (CoM-S-S-CoB) on the MCRred1 form.....	103
Figure 4-7: Overview of the EPR signals of the different MCR forms measured at W-band.....	105
Figure 4-8: Effect of substrate analogs of MCRred1.....	107

Figure 4-9: Effect of 3-bromopropylsulfonate (BPS), 2-bromoethanesulfonate (BES), and bromomethane (BrMe) on MCR in the active MCRred1 form.....	110
Figure 4-10: EPR spectra following the BrMe dependent conversion of MCRred1 into MCR-BrMe.....	112
Figure 4-11: Titration curve showing the increase of the intensity of the MCR-BrMe EPR signal as a function of the BrMe concentration .....	113
Figure 4-12: Decrease of the signal intensity of the MCR-BrMe EPR signal.....	116
Figure 4-13: EPR spectra of the conversion of MCRred1 into MCR-BrMe.....	118
Figure 4-14: Titration of MCRred1 with 3-bromopropane sulfonate (BPS).....	120
Figure 4-15: Titration of MCRred2 with 3-bromopropane sulfonate (BPS).....	121
Figure 4-16: Effect of coenzyme M on MCR-BPS formed from MCRred1 (A) and MCRred2 (B).....	122
Figure 4-17: Titration of MCRred1 with 2-bromoethane sulfonate (BES).....	124
Figure 4-18: Titration of MCRred2 with 2-bromoethane sulfonate (BES).....	125

Figure 4-19: Detailed X-band EPR spectrum of the radical-type EPR signal detected after treatment of MCRred2 with 2-bromoethane sulfonate (BES). .....	126
Figure 4-20: XAS data for MCR-BPS.....	129
Figure 4-21: XAS data for MCR-BES .....	130
Figure 4-22: EPR data for the XAS samples from Figure 4-22.....	131
Figure 4-23: Overlay of the XAS data for MCR-BPS, MCR-BES and MCR-BrMe.....	132
Figure 4-24: Overlay of the XAS data for MCR-BrMe, MCR-BES, MCRsilent and MCRox1.....	133
Figure 4-25: Assay for bromide.....	137
Figure 4-26: Two-pulse echo-detected EPR spectrum.....	139
Figure 4-27: Effect of bromopropionic acid on MCRred2.....	141
Figure 4-28: Effect of several substrate analogs and inhibitors on the MCRred1 form in the presence of 5 mM coenzyme B.....	143

Figure 5-1: Models for the coordination around the nickel ion in MCR-BrCH <sub>3</sub> , MCR-BPS, MCR-BES, and MCR-CH <sub>3</sub> -CoM .....	148
Figure 5-2: Two proposed structures of MCR-BES species .....	152
Figure 5-3: The active site of the MCR-red1-silent structure.....	155
Figure 5-4: Proposed mechanism III.....	158
Figure 5-5: Water channel present in the crystal structure of MCR.....	159

## CHAPTER ONE

### LITERATURE REVIEW

#### 1.1 Methane

Methane ( $\text{CH}_4$ ) is a greenhouse gas that is over 20 times more effective in trapping heat in the atmosphere than carbon dioxide ( $\text{CO}_2$ ) [1]. Methane remains in the atmosphere for approximately 9-15 years. Methane is emitted from a variety of both human-related (anthropogenic) and natural sources [2]. Human-related activities include fossil fuel production, animal husbandry (enteric fermentation in livestock and manure management), rice cultivation, biomass burning, and waste management. Human-related activities release almost 60% of the global methane emissions. Natural sources of methane include wetlands, gas hydrates, (thawing) permafrost, termites, oceans, freshwater bodies, non-wetland soils, and other sources such as wildfires.

Once methane is in the atmosphere, it absorbs terrestrial infrared radiation that would otherwise escape to space and contributes to the warming of the atmosphere. Since 1750, the global average atmospheric concentration of methane has increased by 150 percent from approximately 700 to 1,745 parts per billion by volume (ppbv) in 1998 [3].

Methane is also a primary constituent of natural gas and an important energy source. Methane is important for electrical generation of electricity in a gas turbine or steam boiler. Burning methane produces less carbon dioxide for each unit of heat released compared to other hydrocarbon fuels. Also, methane's heat of combustion is about 802 kJ/mol, which is lower than any other hydrocarbon. However, comparison of the ratio of the molecular mass (16.0 g/mol) divided by the heat of combustion (802 kJ/mol), shows that methane actually produces the most heat per unit mass than any other complex hydrocarbon. In many cities, methane is piped into homes for domestic heating and cooking purposes. It is considered to have an energy content of 39 megajoules per cubic meter, or 1,000 BTU per standard cubic foot [2].

Methane in the form of compressed natural gas is used as a fuel for vehicles, and is claimed to be more environmentally friendly than alternatives such as gasoline/petrol and diesel. Research is being conducted by NASA on methane's potential as a rocket fuel. One advantage of methane is that it is abundant in many parts of the solar system and it could potentially be harvested *in situ*, providing fuel for a return journey [2].

As a result, efforts to prevent or utilize methane emissions can provide significant energy, economic and environmental benefits.

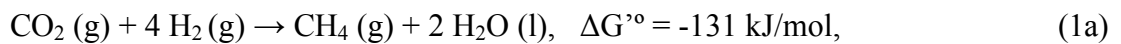
## **1.2 Methanogens**

Among the many types of anaerobic microorganisms, there is a class of strictly anaerobic archaea designated as methanogens [4]. Methanogens are extremely oxygen

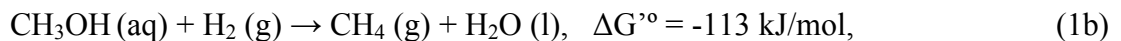
sensitive and are found in anaerobic environments, such as marine sediments, animal intestinal tracts, and sewage. The last one is a particularly rich source of methanogens [4]. Anaerobic bacteria can decompose lipids, carbohydrates, proteins and nucleic acids to hydrogen, carbon dioxide, formic acid and acetic acid. These compounds can all be used by methanogens to form methane. Methanogens are the only organism that can biosynthesize methane [4-6].

For most of the methanogens, the carbon source is carbon dioxide, but a few species such as *Methanosarcina barkeri* can also utilize methanol, methylamines and acetic acid [4, 7, 8].

Overall reaction equations, all methanogens:



*Methanosarcina*



*Methanosarcina*



Under typical biological conditions,  $\Delta G$  for Eq. (1a) is estimated to be -17 kJ/mol and  $\Delta G$  for Eq. (1c) is estimated to be -23 kJ/mol [9].

### 1.3 Methanogenesis

As a result of intensive research, various steps in the methane biogenesis are well understood. This research was carried out mainly by the groups of Ralph Wolfe in Urbana, Illinois, USA [10-12], Rudolph Thauer in Marburg, Germany [13-15], and Gerhard Gottschalk in Göttingen, Germany [16-18]. The hydrogenotrophic pathway for the reduction of carbon dioxide is shown in Figure 1-1. There are six coenzymes involved in this pathway that are only found in methanogens (Figure 1-2).

Figure 1-1 shows that there are 7 steps in this process. In step 1, the carbon dioxide is reduced to a formyl group as part of a carbamate formed by reaction with the primary amine of methanofuran (MFR). This step is catalyzed by W(Tungsten)- or Mo(Molybdenum)-containing formylmethanofuran dehydrogenase. The formyl group is transferred in step 2 to the N-5 of tetrahydromethanopterin (H<sub>4</sub>MPT), catalyzed by formyltransferase. Next, a Schiff base formation reaction of the formyl group with the N-10 yields an imine (step 3) which is then stepwise reduced to a methyl group bound at N-5 in reactions that involve F<sub>420</sub> as an electron donor (step 4 and 5). These three steps are catalyzed by methenyl-H<sub>4</sub>MPT cyclohydrolase (3), methylene- H<sub>4</sub>MPT dehydrogenase (4) and methylene- H<sub>4</sub>MPT reductase (5). In step 6, the methyl group is transferred by methyl transferase to coenzyme M, forming methyl coenzyme M (CH<sub>3</sub>-S-CoM) [10, 19].

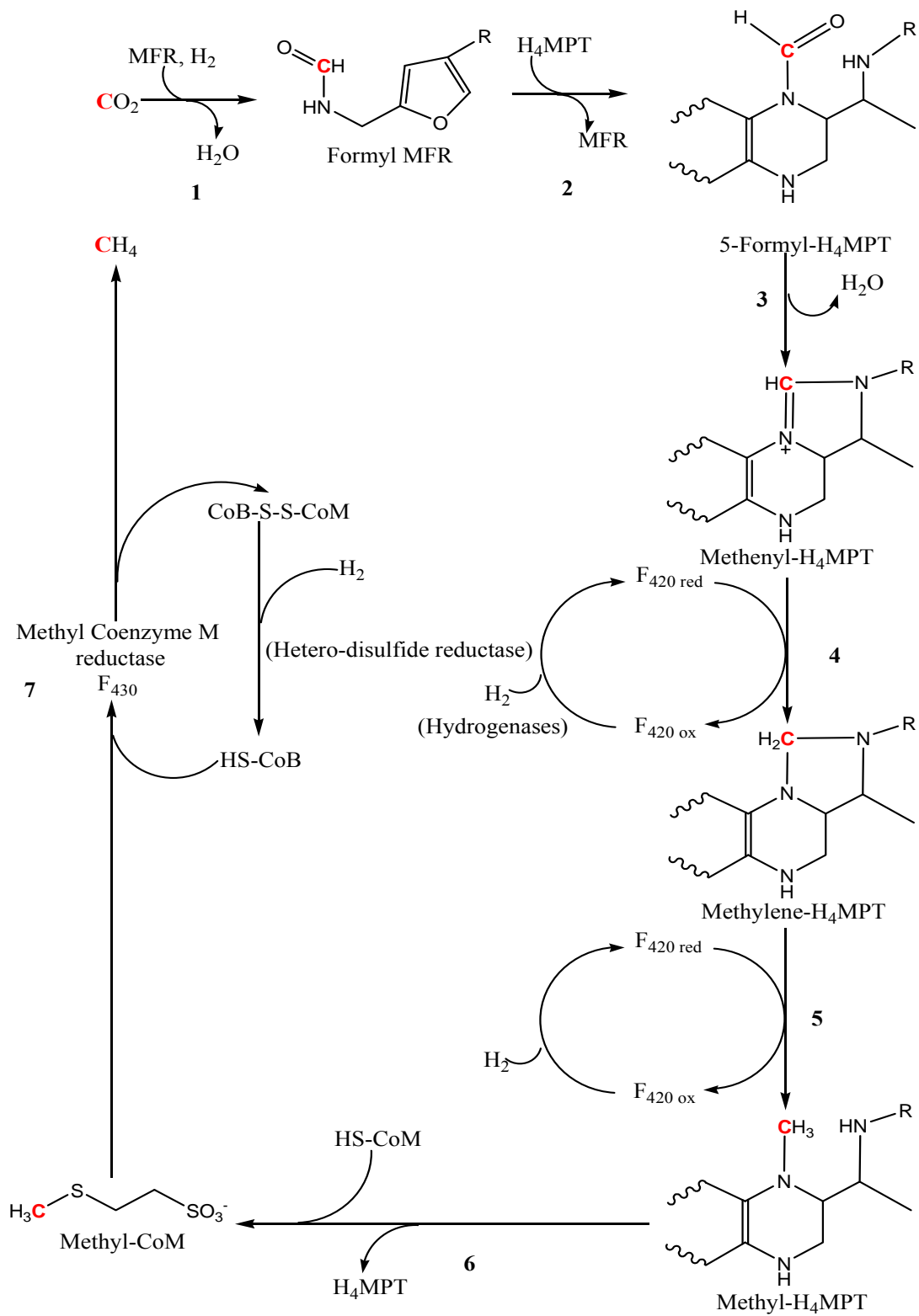


Figure1-1: Hydrogenotrophic Pathway of Methanogenesis

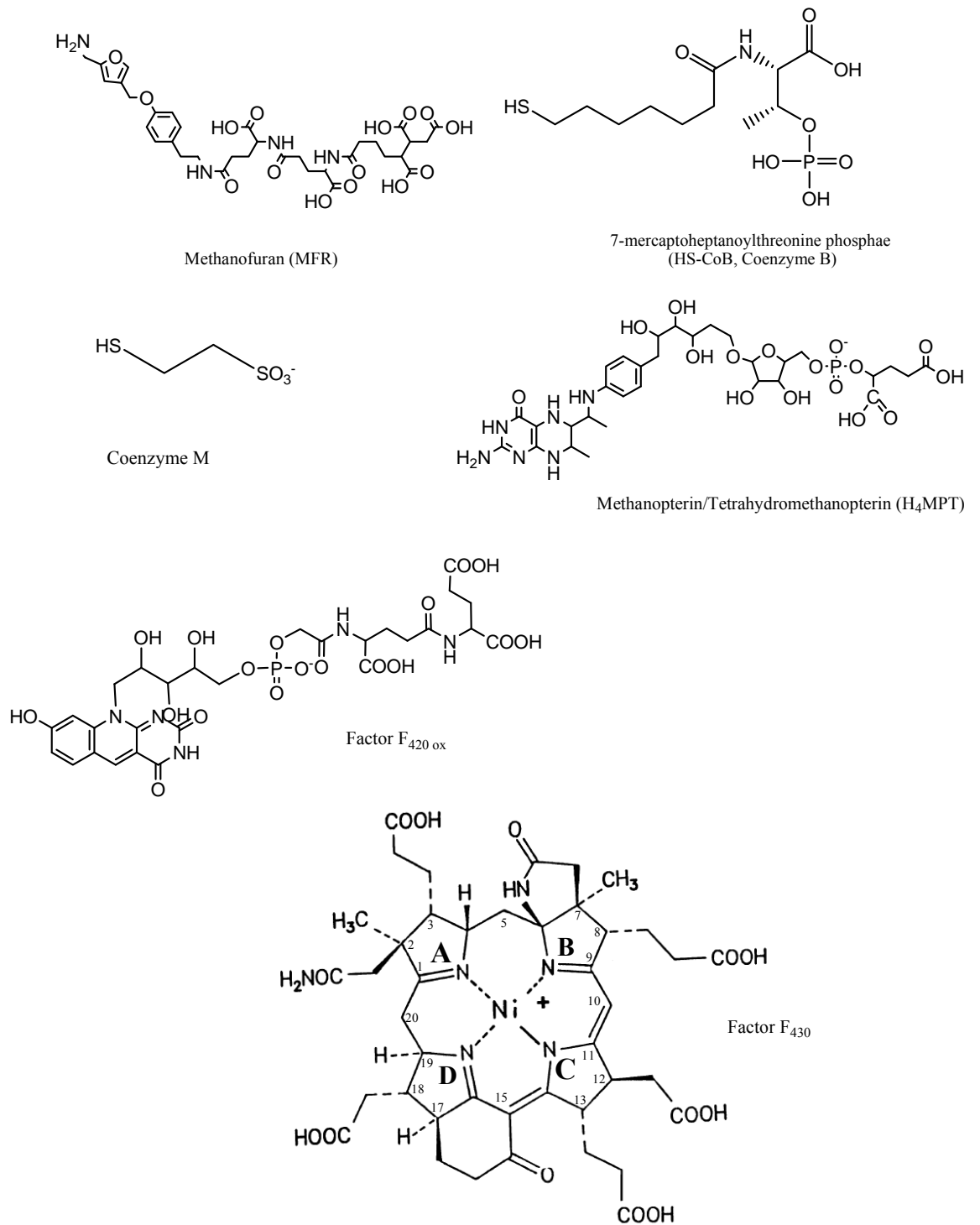


Figure 1-2: Coenzymes used in the hydrogenotrophic pathway

In the final step of methanogenesis,  $\text{CH}_3\text{-S-CoM}$  reacts with coenzyme B (HS-CoB) to yield the unsymmetrical disulfide CoM-S-S-CoB and methane [20, 21]. This reaction is catalyzed by methyl coenzyme M reductase (MCR).

#### 1.4 Nickel Enzymes

Nickel plays an important role in the biological chemistry of the metallic elements, although its occurrence is far less than iron, copper or zinc. There are seven types of Ni-dependent enzymes: urease, carbon monoxide dehydrogenase (CODH) or acetyl-coenzyme A synthase, hydrogenase, nickel superoxide dismutase, nickel-dependent glyoxalase I, acireductone dioxygenase, and the topic of this dissertation MCR. All of these enzymes are found in prokaryotes (bacteria and archaea), although urease is also found in plants [4, 22-25]. Note that most nickel enzymes deal with small gas molecules,  $\text{H}_2$ , CO,  $\text{CH}_4$ ,  $\text{CO}_2$ , and superoxide. The role of nickel in higher organisms is not known yet, although nickel is an essential trace element in animals.

The dependency on nickel of cell growth of *Methanothermobacter marburgensis* was first discovered in 1979. The growth only depends on nickel when cells are grown on hydrogen and carbon dioxide. This was unexpected because at that moment the only enzyme known to contain nickel was urease and it was known that methanogen did not need urea for growth [26]. Shortly, *M. marburgensis* was found to carry eight nickel-containing enzymes based on biochemical and genetic studies [14, 27]: MCR isoenzyme I and II,  $\text{F}_{420}$ -reducing [Ni-Fe]-hydrogenase,  $\text{F}_{420}$ -nonreducing [Ni-Fe]-hydrogenase,

energy converting [Ni-Fe]-hydrogenase isoenzyme I and II, carbon monoxide dehydrogenase and acetyl-CoA synthase.

Among the eight nickel enzymes in strain *M. marburgensis*, MCR isoenzymes, isoenzyme I (McrABG) and isoenzyme II (MrtABG) require the biggest amount of the nickel which is incorporated into the cofactor 430 (F<sub>430</sub>), the prosthetic group of MCR [28]. F<sub>430</sub> is a nickel-containing tetrapyrrole with a unique structure, dubbed corphin (Figure 1-2). The presence of nickel in MCR F<sub>430</sub> was discovered by Ellefson et al. [29].

It is quite interesting that MCR is not only characteristic of methanogenic archaea but also of the methanotrophic archaea which are capable of catalyzing anaerobic oxidation of methane in anoxic marine sediments [30, 31]. The methanogenic archaea are phylogenetically closely related to methanotrophic archaea [32].

## 1.5 Methyl Coenzyme M Reductase

### 1.5.1 Structural properties of the enzyme

MCR was first purified in 1981 [33]. The molecular weight of MCR is about 300,000 Da. MCR is a dimer of  $\alpha\beta\gamma$  protomers ( $\alpha_2\beta_2\gamma_2$ ) [34]. The operon coding for these three peptide chains has been located and sequenced for several species [35].

In 1997, the first crystals of MCR isoenzyme I from *M. Marburgensis* were obtained by Ermler et al [36-38]. Since then the refined crystals of MCR in inactive Ni(II) states were obtained from highly purified MCR from *M. marburgensis* [39]. The overall structure of MCR is arranged by a series of  $\alpha$  helices in a compact and elliptical-shaped form with dimension of 120 by 85 by 80 Å (Figure 1-3) [14, 36]. MCR is a functional dimer with two identical but independent F<sub>430</sub>-containing active sites which are 50 Å apart from each other. Each F<sub>430</sub> is embedded within the protein and could be accessed from the outside by a 50 Å long, pocket-like channel, through which the substrates could reach the cofactor. The term ‘functional dimer’ refers to the fact that it is not possible to separate the  $\alpha\beta\gamma$  protomers without the loss of activity. The  $\alpha$ ,  $\alpha'$ ,  $\beta$ , and  $\beta'$  subunits are tightly associated with each other and seem to form a core area. Additionally, each active-site channel is constructed with strands from four different subunits:  $\alpha$ ,  $\alpha'$ ,  $\beta$ , and  $\gamma$  or  $\alpha'$ ,  $\alpha$ ,  $\beta'$ , and  $\gamma'$ . This arrangement is unique in that the nickel of each F<sub>430</sub> is coordinated on the distal site of the tetrapyrrole ring by the oxygen atom of a Gln residue from the  $\alpha$  subunit of the other protomer (Figure 1-4). This configuration has been proposed to enable the two active sites to “talk to each other” [40].



Figure 1-3: Crystal structure of MCR



The crystal structure of MCROx1-silent and MCRsilent were resolved at 1.16 Å resolution [36]. The reason why the crystallized MCR state is called MCROx1-silent is that upon crystallization, the MCROx1 signal becomes EPR-silent. In this form (Figure 1-5, A), coenzyme B is present in the narrow active site channel with its long aliphatic side-chain about 8Å far away from nickel. Coenzyme M coordinates with the nickel from the proximal side of F<sub>430</sub> by its thiol group. In addition, the oxygen from a glutamine residue (Gln<sup>α147</sup>) coordinates the nickel from the back side, which is observed in all MCR forms crystallized. Figure 1-5 B, shows the crystal structure of MCRsilent. One of the products from the MCR catalytic reaction, the heterodisulfide, coordinates with a sulfonate oxygen to the nickel in the active site [36]. Comparing the position of the heterodisulfide with that of the coenzyme B and the coenzyme M moiety, it can be detected that the coenzyme B moiety of the heterodisulfide in the MCRsilent structure aligns almost perfectly with coenzyme B in the MCROx1-silent structure. The coenzyme M moiety in Fig. 1-5 B has moved to a position where one oxygen atom of the sulfonate is axially coordinated to the nickel. It would be reasonable to picture the structures as the start and finish of the catalytic cycle, with methyl-coenzyme M replacing coenzyme M in structure A [41].

The crystal structures showed some more surprises. They revealed the presence of five modified amino acids near the active-site region. Four of these modifications are methylations [36]. A fifth modification is the insertion of sulfur into the backbone carbonyl of a glycine residue forming a thioglycin [36]. Three of the four methylated amino acid residues were also present in the crystal structure of MCR from

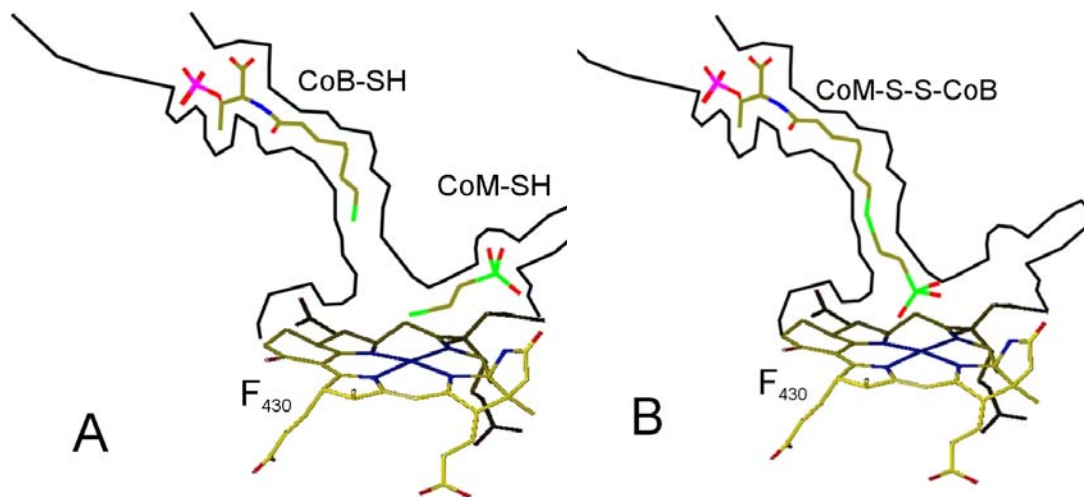


Figure 1-5: Schematic representation of the active-site channels as observed in the crystal structure of MCR in the (A) MCRox1-silent form and (B) MCRsilent form

*Methanosarcina barkeri* [42]. The fact that these residues are completely conserved among the known MCR amino acid sequences already indicates that these modifications are put there on purpose and are not a side effect of the formation of CH<sub>4</sub>. Labeling studies showed that the methyl group of all four amino acids in *M. marburgensis* are posttranslational modifications and are derived from the methyl group of methionine, most likely via S-adenosyl methionine [43]. The glycine residue used to form the thioglycine is also highly conserved. The exact function of these five modifications is not known.

### **1.5.2 in Vitro Assays**

Initially, the work on MCR was very difficult. Without special treatment of the cells and special additives to the purification buffers, 99% of the MCR activity is lost upon cell lysis. Wolfe and his coworkers used an assay for reconstitution of activity that contained several protein fractions (components A1, A2, A3a, A3b and C), coenzyme B and catalytic amounts of ATP, Mg<sup>2+</sup>, NADPH and coenzyme F<sub>420</sub>. With these assays methane was formed from methyl-CoM and hydrogen *in vitro* [44, 45]. Later experiments showed that the complex protein mixture (components A1, A2, A3a, and A3b) could be replaced. Component C was the only one needed for methane formation which revealed that component C was the actual methyl coenzyme M reductase [46]. Later, Ankel-Fuchs and Thauer were able to produce methane in an assay, containing component C, coenzyme B, catalytic amounts of Cob(III)alamin and either dithiothreitol, SnCl<sub>2</sub> or

Ti(III)citrate as electron donors [47]. Finally, in 1988, Thauer and coworkers proved that purified methyl coenzyme M reductase from *M. Marburgensis* is able to catalyze the stoichiometric conversion of coenzyme B and methyl-coenzyme M to heterodisulfide (CoM-S-S-CoB) and methane in the absence of any external reducing agents, thus establishing that the heterodisulfide is the product of the reaction catalyzed by MCR [48].

The activity of MCR, however, was very low. The highest activity observed in cell free assays was only 1 - 5% of the activity for whole cells (based on the known content of MCR). Two possibilities were considered: irreversible deactivation of the enzyme during purification or the destruction of the cell microstructure. Thauer and coworkers found that MCR can be isolated in a much more active form (50% of the *in vivo* activities), if the cells are preconditioned reductively under H<sub>2</sub> and purified under anaerobic conditions [37]. This evidence clearly indicates that irreversible deactivation, presumably by reaction with oxygen, must be the major cause for the low activity observed with the aerobically purified enzyme.

The cellular location of MCR also turned out to be somewhat of a puzzle [9]. Gottschalk and coworkers found that the following step of methanogenesis, heterodisulfide reduction, is coupled to a proton motive force. This finding suggested it is a membrane-associated process [49, 50]. It turned out that in several archaea the heterodisulfide reductase is membrane-bound. However, in *M. marburgensis* the heterodisulfide reductase is found in the cytoplasm. In the purification process, MCR is found in the cell fraction, not in the membranes. Wolfe and coworkers did immunoelectron microscopy using gold-labeled antibodies for MCR in 1986. The results

showed distribution of MCR over the entire cell interior in *M. thermoautotrophicus*, whereas in *Methanococcus voltae* MCR was located near the membranes [51]. Further work on strain Göl showed that MCR activity was associated with membrane associated particles called protoplasts [52, 53]. Protoplasts were isolated by pronase treatment of whole cells [54] and inside-out membrane vesicle were generated which had hollow spherical particles attached to the outer surface (originally the inner side) of the membrane via a short channel-like structures. Gold-labeling of MCR showed that several copies of the enzyme were located in the wall of the spherical part of these particles [55].

### **1.5.3 Substrate Analogs and Inhibitors**

Even with the partly active enzyme, the groups of Wolfe [56], Walsh [57] and Thauer [47, 58] obtained valuable kinetic data on the selectivity of MCR. Gas chromatography is used for assaying MCR activity. Measuring the time dependent formation of methane is the most direct way to measure activity of MCR [47, 56-58]. Most of these studies, however, were done with cell extracts instead of pure protein. Allyl coenzyme M ( $\text{CH}_2=\text{CH}_2\text{CH}_2\text{-S-CoM}$ ), for example turned out not to be an inhibitor of MCR when tested on purified MCR. The compounds listed in table 1-2 all have been shown to have an effect on MCR using the technique of electron paramagnetic resonance (EPR) spectroscopy [59].

**Table 1-1: Substrate Analogs for Methyl Coenzyme M Reductase**

Substrate	Activity as an analog	
	$K_M$ (mM)	$V_{max}^a$
$\text{CH}_3\text{SCH}_2\text{CH}_2\text{SO}_3^-$	0.1	11
<b><math>\text{CH}_3\text{CH}_2\text{SCH}_2\text{CH}_2\text{SO}_3^-</math></b>	1.3	7.4
$\text{CH}_3\text{SeCH}_2\text{CH}_2\text{SO}_3^-$	0.3	35
<b><math>\text{CF}_2\text{HSCH}_2\text{CH}_2\text{SO}_3^-</math></b>	2.5	20
<b><math>\text{CH}_3\text{SCH}_2\text{CH}_2\text{CO}_2^-</math></b>	1.3	1.3

<sup>a</sup>nmol·hr<sup>-1</sup>·(mg protein)<sup>-1</sup>

**Table 1-2: Inhibitors of Methyl Coenzyme M Reductase**

Substrate	Inhibitor $I_{50}$ (mM) <sup>a</sup>
$\text{N}\equiv\text{C-SCH}_2\text{CH}_2\text{SO}_3^-$	0.032
$\text{CF}_3\text{SCH}_2\text{CH}_2\text{SO}_3^-$	7.0
$\text{CH}_3\text{OCH}_2\text{CH}_2\text{SO}_3^-$	>20
<b><math>\text{BrCH}_2\text{CH}_2\text{SO}_3^-</math></b>	0.004
<b><math>\text{BrCH}_2\text{CH}_2\text{CH}_2\text{SO}_3^-</math></b>	$5 \times 10^{-5}$
$\text{N}_3\text{CH}_2\text{CH}_2\text{SO}_3^-$	0.001

<sup>a</sup>Concentration of inhibitor giving 50% of the methane formation rate observed in the absence of the inhibitor with 0.1 M Me-CoM

### 1.5.4 Structure and Properties of Coenzyme F<sub>430</sub>

Coenzyme F<sub>430</sub> was first observed by LeGall as a yellow band in chromatograms of cell extract [8]. Later, F<sub>430</sub> was described as a component of MCR by Ellefson et al. [29]. Following the discovery that growth of methanogens critically depended on the presence of nickel in the culture medium [60], Thauer and coworkers found that a large part of the nickel present in the cells was incorporated into F<sub>430</sub> [61].

Tetrapyrrole biosynthesis proceeds via 6-aminolevulinic acid ( $\delta$ -ALA) and porphobilinogen as intermediates. Growth studies with *M. thermoautotrophicum* showed that factor F<sub>430</sub> becomes labeled when the organism is grown in the presence of  $\delta$ -[4-<sup>14</sup>C] ALA, confirming that the F<sub>430</sub> was a nickel tetrapyrrole [62, 63]. Later, a collaboration between the laboratories in Marburg and the ETH (Eidgenössische Technische Hochschule Zürich) in Zurich was initiated, which led to the determination of the constitution of coenzyme F<sub>430</sub> and the assignment of configuration for all the stereogenic centers (Figure 1-2) [9, 64]

F<sub>430</sub> is a yellow compound which has a maximal absorbance at 430 nm. It has a molecular mass of ~905 Da and is conserved in all of the nickel corphin cofactors in methanogenic archaea [26]. The EPR spectra shown in Figure 1-6 are for the free F<sub>430</sub>M, the pentamethyl ester form of F<sub>430</sub>, in three different oxidation states. In the F<sub>430</sub>M form, the five carboxylic acid groups (Figure 1-2) have been methylated. F<sub>430</sub>M is soluble in nonpolar, noncoordinating solvent. This property helped resolve the structure of F<sub>430</sub> with nuclear magnetic resonance (NMR) spectroscopy since the nickel ion tends to form

coordinated complexes in both  $F_{430}$  and  $F_{430}M$  in the presence of donor ligands. These forms are paramagnetic while the uncoordinated forms are not [41].  $Ni(II)F_{430}$  in acetonitrile could be oxidized to  $Ni(III)F_{430}M$  at a redox potential ( $E^\circ$ ) of 1.94 V (vs. SHE (standard hydrogen electrode) ) [65]. Both  $Ni(II)F_{430}M$  in acetonitrile and  $Ni(II)F_{430}$  in water could be reduced to the  $Ni(I)$  state at a redox potential ( $E^\circ$ ) of -0.650 V (vs. SHE) [66, 67]

### 1.5.5 EPR Studies of different MCR forms

EPR has proven to be very important in the study of MCR and  $F_{430}$  since this technique directly addresses the electronic structure of nickel [5, 68, 69]. The three oxidation states that are accessible in free  $F_{430}M$  show very different EPR spectra (Fig. 1-6).  $Ni(I)F_{430}M$  has a spin state  $S = \frac{1}{2}$  with the unpaired electron residing in the  $d_{x^2-y^2}$  orbital. The four lobes of the orbital point toward the four N-ligands present in the tetrapyrrole ring, which result in the presence of additional superhyperfine structure on the EPR signal. The  $Ni(II)F_{430}M$  state can be  $S = 0$  or  $S = 1$  dependent on the presence and types of axial ligands. Neither form, however, is detectable by EPR spectroscopy. The  $Ni(III)F_{430}M$  state has the spin state  $S = \frac{1}{2}$  and is EPR detectable. In this case the free electron resides in the  $d_{z^2}$  orbital. The superhyperfine structure detectable on the  $g_z$  peak is due to the N-atoms from two axial acetonitrile ligands.

MCR exhibits different EPR signals associated with different states of the enzyme. The conditions of the induction of some important MCR forms are described below. The

different EPR spectra are shown in Figure 1-7. The MCRox1 signal shows highly resolved superhyperfine splitting due to the nitrogen ligands, indicating that the MCRox1 EPR signal arose from the nickel from F<sub>430</sub>. When the ox1 signal was discovered it was found that this state had low activity that did not match with the MCRox1 EPR signal intensity, which suggested the MCRox1 represented an inactive species. This form was originally proposed to have the nickel in the +3 oxidation state, because the signal could be formed under more oxidizing conditions in the cell and is relatively stable against oxygen. However the EPR signal of this state is completely different from that of Ni(III)F<sub>430</sub>M. Comparison of Figure 1-6 and Figure 1-7 shows identical spectra for MCRred1 and Ni(I)F<sub>430</sub>M indicating that the nickel in the MCRred1 form is in the +1 oxidation state.

Based on the similarities between the EPR spectrum of MCRox1 and the one of Ni(I)F<sub>430</sub>M, it was proposed by Ragsdale et al [70], that the nickel in the MCRox1 form was also +1. Initially, this proposal was supported by electron nuclear double resonance (ENDOR) measurements [71]. Further investigation, however, with X-ray absorption spectroscopy (XAS) [40] (see below) and magnetic circular dichroism (MCD) spectroscopy [72, 73] showed that this was not correct. The nickel is formally +3, but a more accurate of description of the MCRox1 form is something that is halfway between a Ni(III) species and a Ni(II)-thiyl radical species. This description is fully supported by density functional theory (DFT) calculations [74].

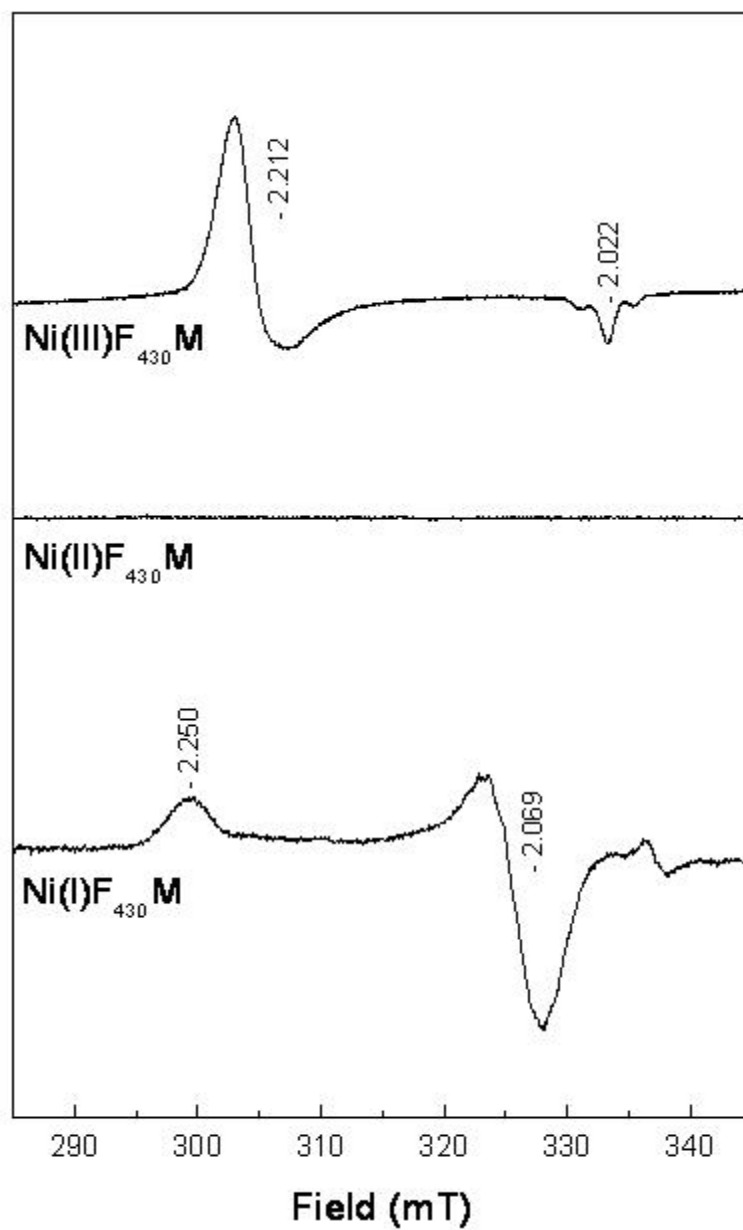


Figure 1-6: EPR spectra of the pentamethyl ester form of F<sub>430</sub> (F<sub>430</sub>M) in different oxidation states

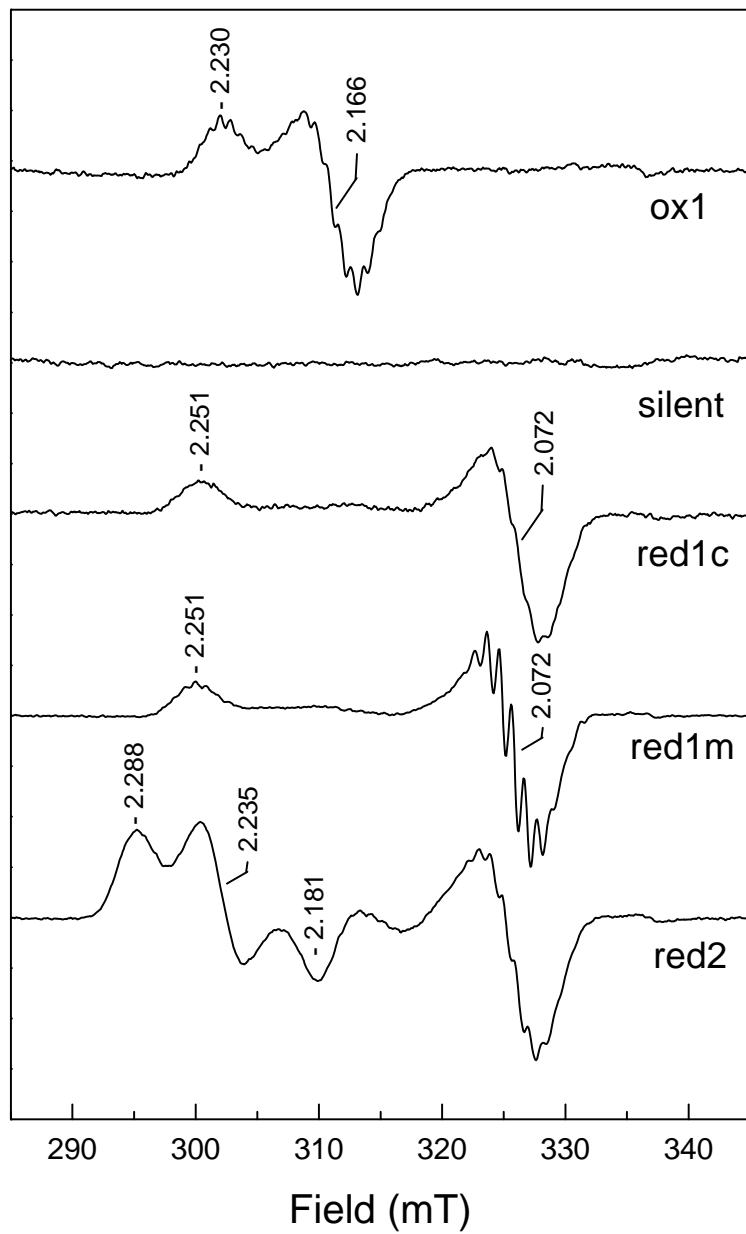


Figure 1-7: EPR spectra of methyl-coenzyme M reductase in different forms.

Albracht and coworkers identified two other very important EPR signals, MCRred1 and MCRred2, in intact cells of *M. Marburgensis* reduced by H<sub>2</sub> [68, 75]. Subsequently, Rospert et al. were able to maintain these signals in cell extracts as well [37]. In contrast to MCRox1, the intensity of the MCRred1 signals matched the enzyme activity [68]. The EPR spectrum of MCRred2 looks more complicated than any of the others since there are two new signals red2 (axial) and red2 (rhombic) and some leftover red1 signal. These two forms can be induced in vitro from the MCRred1 form by addition of coenzyme M and coenzyme B [76]. This conversion is reversible and the nickel is expected to still be Ni(I).

Like Ni(II)F<sub>430</sub>M (Figure 1-6), the silent MCR forms have the nickel in the +2 oxidation state and are not EPR detectable. Depending on the methods of preparation, three different silent forms are distinguished: MCRsilent, MCRred1-silent, and MCRox1-silent [40]. All three forms have a spin state  $S = 1$ , which allows investigations of these forms with the help of MCD spectroscopy [77].

There are several sub-types of MCRred1 signals which look very similar. One is called MCRred1**c**, indicating MCRred1 in presence of **co**enzyme M in the solution. The other is named MCRred1**m**, designating MCRred1 in presence of **methyl**-coenzyme M in the solution. The slight difference between these two is that MCRred1m shows much more resolved superhyperfine structure. Recent ENDOR measurements showed that this is due to the presence of methyl-coenzyme M. The thiol sulfur of this compound approaches the nickel to a distance of 3.08 Å [ref. in press]. This is too far to be

considered a real bond, but close enough to affect the electronic properties of the nickel. MCRred1 in the absence of either compound is called MCRred1a.

### 1.5.6 XAS Studies of different MCR forms

X-ray Absorption Spectroscopy (XAS) is a sensitive technique to probe the coordination and oxidation states of metal ions. Prior XAS studies of cofactor F<sub>430</sub> and MCR showed that the isolated cofactor in solution exists as a mixture of low-spin four coordinate and high-spin six-coordinate Ni(II) species [78, 79]. The Ni(II) center in the cofactor of MCRsilent forms is six-coordinate. Conversion from low-spin four-coordinate Ni(II) to high-spin six-coordinate Ni(II) results in a lengthening of the Ni-N bond in the macrocycle from 1.9 to 2.1 Å [78]. This is due to the flexibility of the F<sub>430</sub> macrocycle, which was shown to be an important parameter in generating Ni(I) species upon reduction (as opposed to macrocycle radicals) [80-83]. These studies concluded that the isolated cofactor in the Ni(I) state was in a distorted four-coordinate geometry in isolated cofactor F<sub>430</sub>.

XAS studies were also performed on the different forms of MCR. To make strong conclusions based on this technique it is important to have enough of other data available for comparison. In this case it was already known from the crystal structure that the MCRsilent and MCRox1silent forms had six-coordinated Ni(II) forms where the sixth ligand was an oxygen in the case of MCR silent, and a sulfur in the case of MCRox1silent. The MCRred1c and MCRred1m edge spectra (Figure 1-8, blue lines) are similar and shifted to lower energy relative to those of the MCRsilent and MCRox1silent

spectra, indicating that the Ni in MCRred1 has a valence electron density expected for  $d^9$  Ni(I). However, the edge position of the MCROx1 spectrum is similar to that of the two silent Ni(II) forms, indicating that the valence electron density on the nickel in these forms is comparable. Since MCROx1 is EPR active (Figure 1-7), indicating the presence of an unpaired electron, it was expected that the edge position would be very different, either lower for Ni(I) or higher for Ni(III). The MCROx1 spectra are slightly shifted in edge position and have a lower intensity relative to the MCRsilent and MCROx1silent samples, indicating that the electron density on the nickel atom in MCROx1 is only slightly decreased relative to that in the Ni(II) forms.

For MCROx1, MCROx1silent, and MCRsilent, best fits were obtained assuming a sixth ligand, a sulfur ligand in the case of MCROx1 and MCROx1silent and a nitrogen or oxygen ligand in the case of MCRsilent. For MCRred1m and MCRred1c, best fits were obtained assuming five-coordinate nickel with four nitrogen ligands from F<sub>430</sub> and one oxygen ligand from the distal Gln residue (Figure1-9). Although extended x-ray absorption fine structure (EXAFS) has an inherent error of  $\pm 1$  with regards to the number of scatterers, which makes the determination of absolute coordination number impossible, it was apparent from the goodness-of-fit values and Debye–Waller factors that the Ni in MCRred1 samples had fewer ligands in its coordination shell than the Ni in MCROx1 and MCRsilent samples [36].

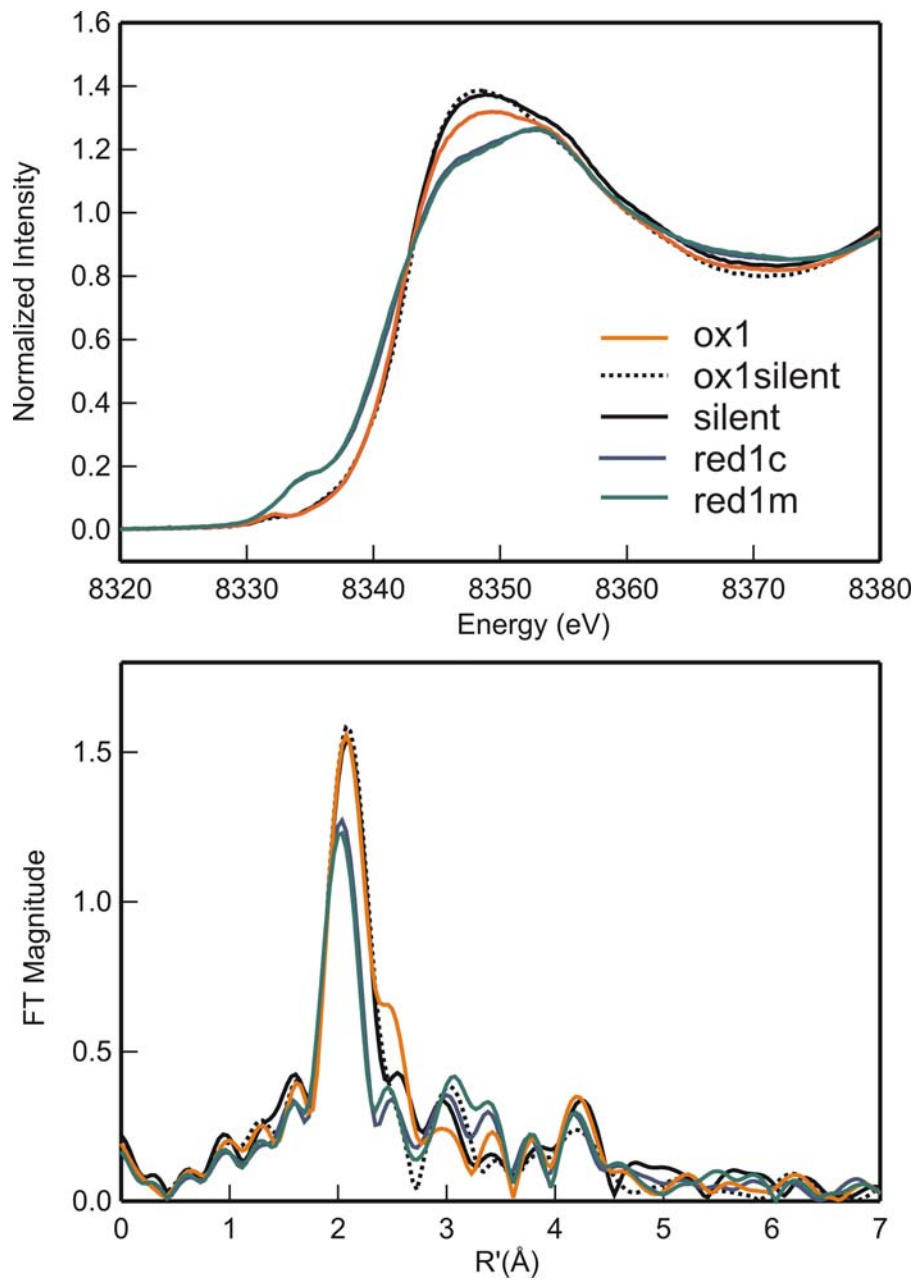


Figure 1-8: X-ray absorption spectra of MCR, adapted from [40].

### 1.5.7 The Activation Cycle of Methyl-Coenzyme M Reductase

MCR has different states as mentioned above. Some have been detected in whole cells, some were artificially prepared *in vitro* and have been characterized with spectroscopic techniques. The forms detected in whole cells might be involved in the reaction mechanism as well as the activation process. Among these forms, only the MCRred1 form is active. Figure 1-9 shows the important relationship between different MCR forms as studied *in vitro*. The active form, MCRred1, can be converted to MCRred2 when incubated with coenzyme M and coenzyme B and this step is reversible [76]. As for MCRred2, it can be converted to an inactive but important form, MCROx1, by addition of the oxidant polysulfide [84]. The MCROx1 form can be activated to form MCRred1 by incubation with the artificial reductant titanium(III) citrate at pH 9.0 and 65°C [85]. It is not clear what reductant and/or oxidant is used by the cell.

MCRred1 is highly oxygen sensitive and it will be converted into a MCRsilent form immediately after contact with oxygen or other oxidants. MCRred2 is oxygen sensitive too. Exposure leads to the formation of MCROx3, which will not be discussed here. MCROx1 is relatively oxygen stable and the signals would quench given longer time. It might be interesting if we look at this behavior in the way that the cell is forced to launch a protection mechanism to keep MCR from oxygen by converting MCRred1 to other MCR forms except MCRsilent. It is safe to assume that when methanogens are under certain microaerobic conditions, hydrogen production from fermentation processes would slow down to some extent, and the pathway for methyl-coenzyme M formation is blocked so that the amount of coenzyme M would start to build up. Together with the

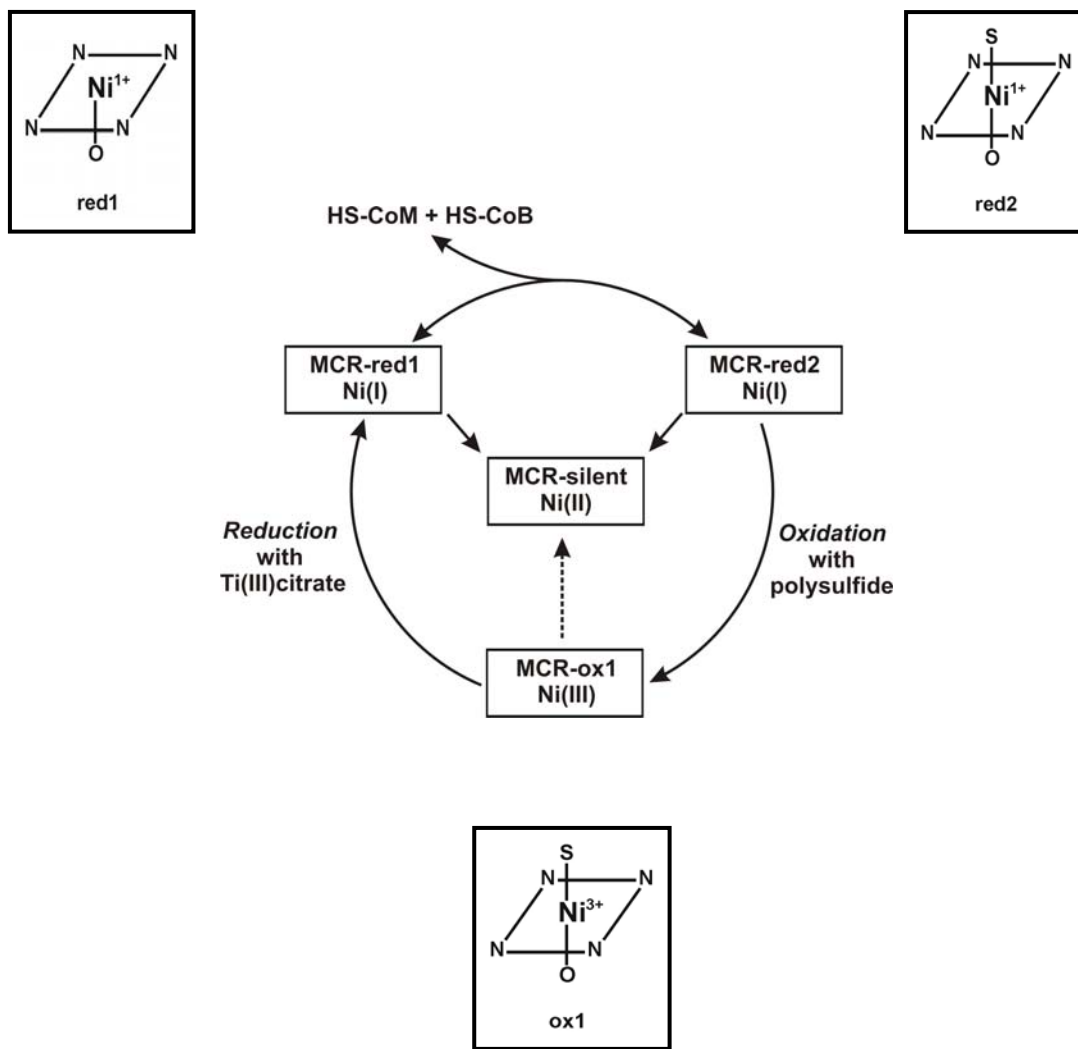


Figure 1-9: Conversion cycle between three forms of MCR: MCRred1, MCRred2, and MCRox1

coenzyme B available in the cell, this could lead to MCRred2 formation and finally MCRox1 formation.

### 1.5.8 Anaerobic Oxidation of Methane (AOM)

Before going into detail about the different hypothetical mechanisms that are discussed in the literature it is important to mention the recent discovery that MCR is probably involved in the anaerobic oxidation of methane (AOM). Methanotrophic archaea that are able to catalyze AOM were discovered on top of methane seeps in the Black Sea [86]. It was found that these archaea contain two methyl-coenzyme M reductases. One contained the regular cofactor F<sub>430</sub> with a molecular mass of 905 Da while the other contained a modified F<sub>430</sub> with a molecular mass of 951 Da, which could be the origin of the differences in catalytic properties of the enzyme from methanotrophic archaea and that from methanogenic archaea [26]. However, recent studies show that some of these methanotrophs contain only the regular 905-Da form of F<sub>430</sub>.

There is a thermodynamic aspect related to the very slow pace of the methane oxidation process [87, 88]. The standard free energy change  $\Delta G^\circ$  associated with the methane production step is about -30 kJ/mol (CH<sub>4</sub>).

Under physiological conditions:

$$\Delta G = \Delta G^\circ + RT \ln \frac{[products]}{[substrates]} = -30 + 5.7 \log \frac{[products]}{[substrates]}$$

From this equation, it can be derived that the reaction catalyzed by MCR will become reversible only when the ratio of the products to substrates concentration is around  $10^5$ , which is physiologically feasible [26]. Additionally, it was proposed that sulfate-reducing bacteria helped to make the methane oxidation process thermodynamically favorable based on the observation that the first-found microbial consortium being responsible for anaerobic methane oxidation contains archaea surrounded by sulfate-reducing bacteria [30, 41]. So the reversibility of the reaction cycle catalyzed by MCR needs to be taken into account for catalytically mechanistic proposals if this is known for certainty.

### **1.5.9 Catalytic Mechanism of MCR**

Although there is a huge number of structural, spectroscopic, kinetic and biochemical as well as computational data available to point out different directions for the catalytic mechanism of MCR, basically it could be narrowed down to two radically different models that are consistent with most findings while still having unsolved problems [14, 70]. All models take into account: (1) that the catalytic cycle starts with enzyme in the Ni(I) oxidation state; (2) that the enzyme exhibits a ternary complex involving methyl-coenzyme M and coenzyme B [89]; and (3) that of the two substrates, methyl-coenzyme M has to enter the active site channel first. The reaction does not start, however, until coenzyme B is present. The difference between the proposed mechanisms is the initial interaction between methyl-coenzyme M and the Ni of F<sub>430</sub>.

Proposed mechanism I is shown in Figure 1-10. Ni(I)-MCRred1 reacts with methyl-coenzyme M to form a methyl-Ni(III) intermediate by nucleophilic attack. The formed methyl-Ni(III) intermediate withdraws an electron from coenzyme M to generate a methyl-Ni(II) intermediate and a coenzyme M thiyl radical. Then methyl-Ni(II) is protonolyzed by electrophilic substitution producing methane. The coenzyme M thiyl radical reacts with coenzyme B to produce the heterodisulfide anion radical. At last, the excess electron goes back to nickel and converts Ni(II) back to Ni(I) [9, 34, 90-92].

Mechanism I was proposed on the basis of cobalamin biochemistry and the fact that (i) ethyl-coenzyme M reduction catalyzed by MCR proceeds with inversion of stereo configuration at the carbon atom of the ethyl group [93], (ii) that Ni(I) F<sub>430</sub> in MCR reacts with 3-bromopropane sulfonate to form an alkyl-Ni(III) species [94]; (iii) that in aprotic solvents, free Ni(I)F<sub>430</sub> reacts with methyl iodide to form methyl-Ni(II) F<sub>430</sub> which is subsequently protonolyzed to methane and Ni(II)F<sub>430</sub> [95, 96]. The catalytic efficiency of methyl-coenzyme M reduction, however, is much lower than the reduction of ethyl-coenzyme M indicating that the catalytic cycle could start with a nucleophilic substitution [97]. Nevertheless, according to density functional studies, mechanism I might be energetically unfavorable [98, 99].

The energetic obstacles of mechanism I in the methane forming step have led to two alternative mechanisms. Mechanism Ib keeps the formation of a CH<sub>3</sub>-Ni intermediate as the key step. But CH<sub>3</sub>-S-CoM is activated prior to the reaction with Ni(I) and the generation of a thiyl radical by reducing Ni(III) is avoided. The basic idea behind this mechanism is the presence of a second redox active group (R) which might be the

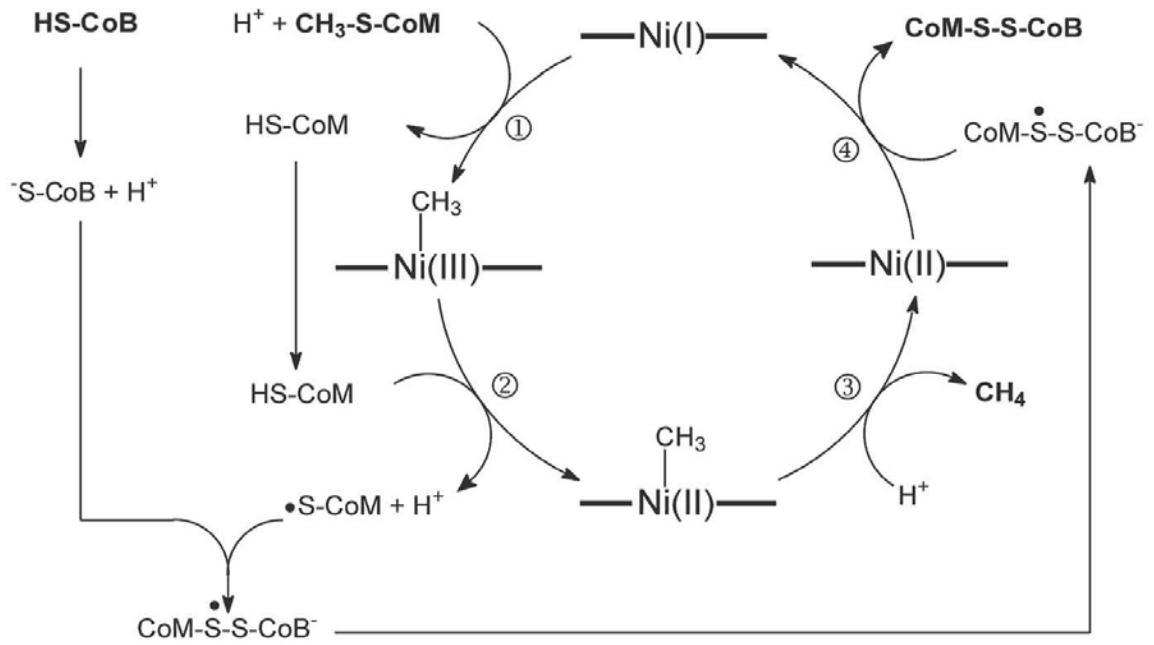


Figure 1-10: Proposed mechanism model I

modified Gly<sup>a445</sup>. The reaction cycle is represented in Figure 1-11: At first, the second redox active group is reduced to an anion radical and HS-CoB is oxidized to a CoB thiyl radical [14, 70]. Then, the CoB thiyl radical reacts with CH<sub>3</sub>-S-CoM to form a sulfuranyl radical that is attacked by Ni(I) generating the heterodisulfide CoM-S-S-CoB and CH<sub>3</sub>-Ni(II) the latter being protonolyzed to methane and Ni(II) [91]. The catalytic cycle would be closed by an electron transfer from the radical anion to Ni(II).

Mechanism Ib evades the weakness of mechanism I. Mechanism Ib matches the inversion of stereoconfiguration and directly integrates HS-CoB into the methane formation process that is suggested by single-turnover experiments on CH<sub>3</sub>-S-CoM using presteady-state kinetic methods [100]. But the participation of a second redox active group (besides nickel) has not been proven and the redox potential for the thioglycine/thioketyl anion radical (of Gly<sup>a445</sup>) of -1.4V and for the thiyl radical/thiol of ~1V is extremely unfavorable for a redox reaction. Moreover, the geometry of the active site implicates a too large distance between the methyl group of the sulfuranyl radical and Ni(I) for an attack. The HS-CoB analogue HS-CoB<sub>8</sub> should fill out this gap but it exhibits no activity at all [43].

Mechanism II (Figure 1-12) was proposed based on quantum mechanical calculations. The key step involves an attack of Ni(I) on the thioether sulfur instead of the methyl group of methyl-coenzyme M, yielding a Ni(II) thiolate and a free methyl radical which withdraws a hydrogen atom from the sulfhydryl group of coenzyme B to form methane. The formed coenzyme B thiyl radical reacts with coenzyme M thiolate to the heterodisulfide radical anion which returns the excess electron to the nickel [90].

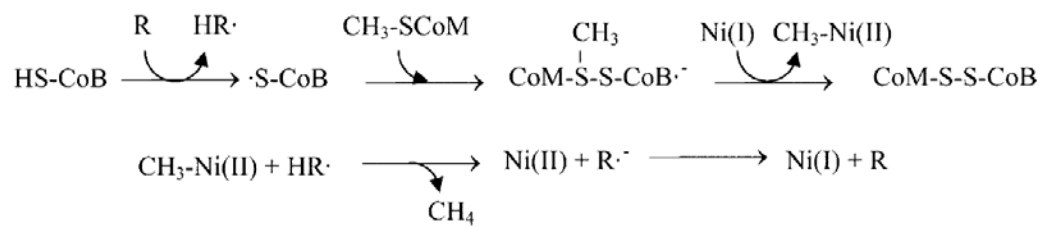


Figure 1-11: Hypothetical mechanism model Ib

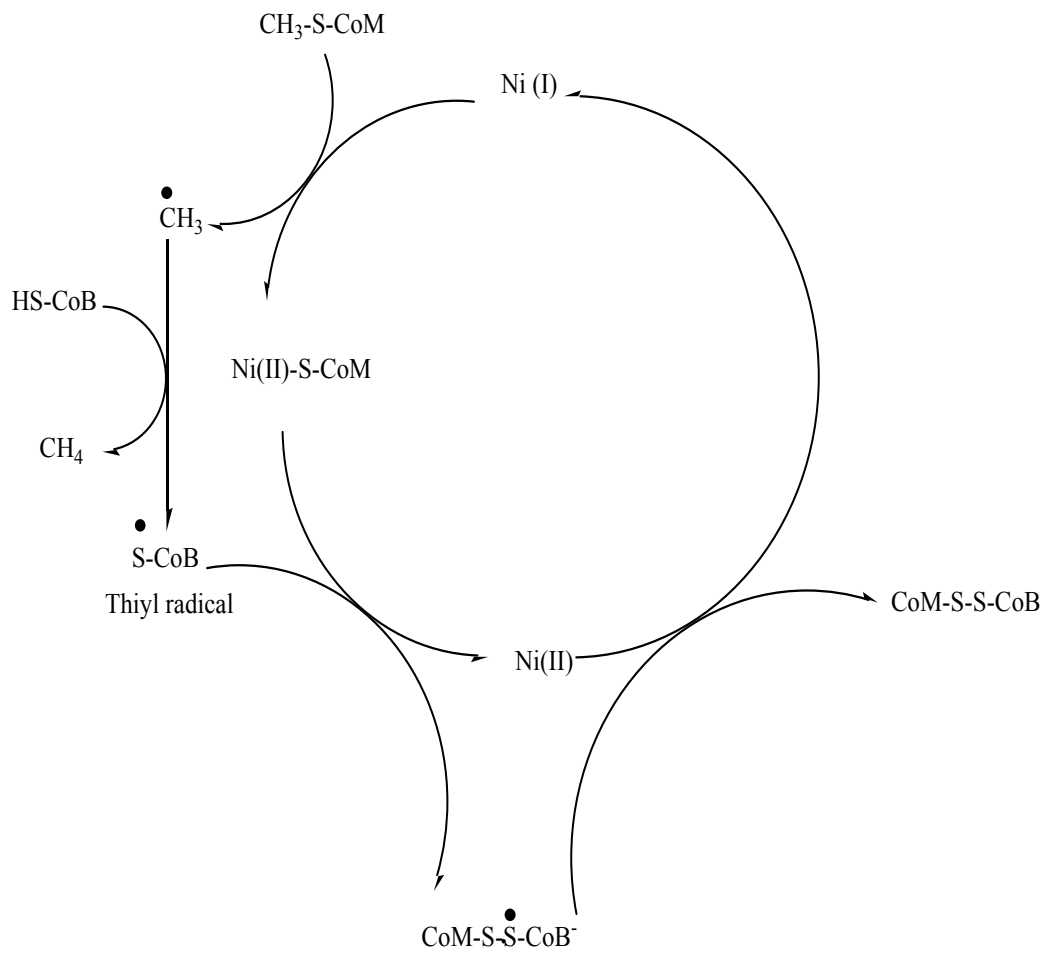


Figure 1-12: Hypothetical mechanism model II

This alternative mechanism is energetically much more favorable than Mechanism I in terms of the formation of the methyl-Ni(II) intermediate [98] and is also consistent with the finding that when coenzyme B is around, coenzyme M reversibly coordinates to Ni(I) F<sub>430</sub> in active MCR with its thiol sulfur [101]. However, it could not explain the finding of the low catalytic efficiency of the reduction of ethyl-coenzyme M [26]. Another problem with this mechanism is the fact that the binding of methyl-coenzyme M to the nickel and the formation of the methyl radical is actually a very low energy step. This would result in a partial reaction even in the absence of coenzyme B. To still stay within the requirement, the authors proposed that there is a binding site for methyl-coenzyme M at the entrance of the active-site channel. Binding of coenzyme B would push this compound further into the channel and the reaction would start. The recent ENDOR data, however, showed that even in the absence of coenzyme B, the thiol sulfur of methyl-coenzyme M comes as close as 3.08 Å to the nickel of F<sub>430</sub>, which according to the model should result in partial reactivity.

If we think about the role methyl-coenzyme M may play in the anaerobic oxidation of methane, both of them are far from being impeccable because of the reversibility of the reaction cycle that we should take into account. For instance, in mechanism I, methane oxidation has to start with the attack on methane by Ni(II)F<sub>430</sub>, which is extremely difficult because of its low electrophilicity suggested by the low redox potential of -650 V (vs. SHE) of the Ni(II)F<sub>430</sub>/Ni(I)F<sub>430</sub> couple [9]. As for mechanism II, likewise, the attack on methane by the coenzyme B thiol radical is also energetically unfavorable since

the bond dissociation energy of the C-H bond in methane is higher than that of the S-H bond [26].

#### **1.5.10 MCRred2, the key to understanding the catalytic mechanisms of MCR?**

In the presence of coenzyme M (HS-CoM) and coenzyme B the MCRred1 state is converted into the MCRred2 state, which shows a mixture of axial and rhombic Ni(I)-based EPR signals (Fig. 1-7). The MCR-red2 state is also induced by several coenzyme B analogues [72, 97]. The rhombic signal was designated MCRred2rhombic. The remaining axial signal detected (Fig. 1-7) is part red1 that is left over, and part a new species designated MCRred2axial. The conversion of the MCRred1 state into the MCRred2 state upon addition of coenzyme B occurs only in the presence of coenzyme M and is associated with the reversible coordination of the thiol group of coenzyme M to the active-site Ni(I) of the MCRred2rhombic form as revealed by EPR and ENDOR spectroscopic data with unlabeled and  $^{33}\text{S}$ -labeled coenzyme M [72, 76, 101]. From the purification of MCR it is known that both coenzyme M and methyl coenzyme M can stabilize the protein during the purification procedures. It would be safe to assume that both compounds bind to MCR to be able to do this. ENDOR studies showed that in the MCRred1m form, the thioether sulfur of methyl coenzyme M approaches the nickel as close as 3.08 Å [76]. In the case of coenzyme M, the molecule seems to be bound further away from the nickel. We propose that the addition of coenzyme B induces a conformational change in MCR-red1c, bringing the thiol group of coenzyme M into

binding distance of the Ni(I). Such a conformational change is probably also required in the reaction of methyl-coenzyme M with the Ni(I), which has been proposed to be the first step in the catalytic cycle of methyl-coenzyme M reduction to methane in all but one mechanism discussed [59, 65, 91, 92, 98-100].

At high temperature MCR displays the highest amount of the MCRred2 rhombic form, but at low temperature this form converts back to the MCRred2 axial form [97]. These changes with temperature were fully reversible [97]. It was found that at most 50% of the enzyme was converted to the two MCR-red2 states under all experimental conditions. It was proposed that in the presence of both coenzyme M and coenzyme B only one of the two active sites of MCR can be in the red2 state (half-of-the-sites reactivity) [97].

The length of the aliphatic arm of coenzyme B is very important (Figure 1-13). When the chain is shortened in C<sub>6</sub>-coenzyme B, this compound shows only 1% of the activity observed with C<sub>7</sub>-coenzyme B. With C<sub>8</sub>-coenzyme B no activity is detectable. Both C<sub>6</sub>-coenzyme B and C<sub>8</sub>-coenzyme B are inhibitors. Interestingly a similar effect is also seen when these compounds are used to induce the red2 state. No red2 is formed with C<sub>8</sub>-coenzyme B, while C<sub>6</sub>-coenzyme B can only induce a small amount of red2 form.

Another set of coenzyme B analogs (Figure 1-14) show that induction of the red2 form is dependent on the presence of the thiol-sulfur of coenzyme B. No red2 is detected with H-C<sub>7</sub>-CoB, while HS-C<sub>7</sub>-CoB and CH<sub>3</sub>-S-C<sub>7</sub>-CoB do induce this form even though the last compound is not a substrate.

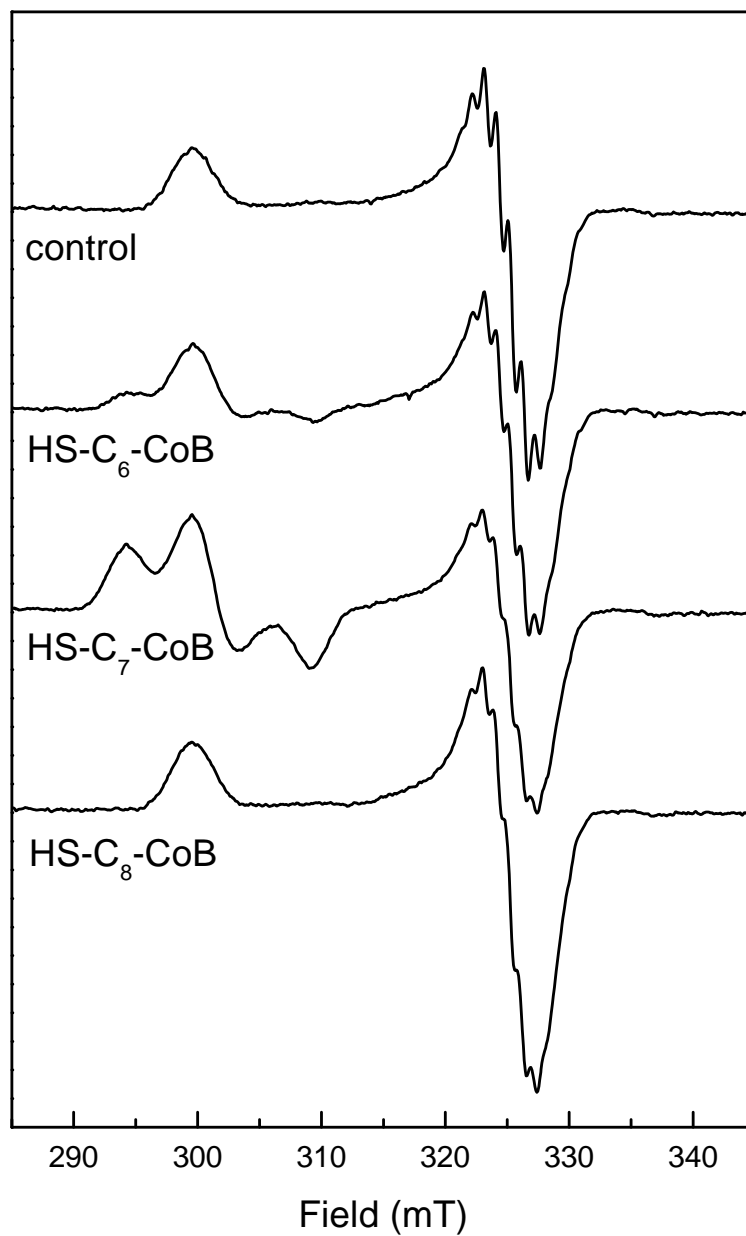


Figure 1-13: Induction of the red2 form with different coenzyme B analogs (Different chain length). All samples contained 10mM coenzyme M.

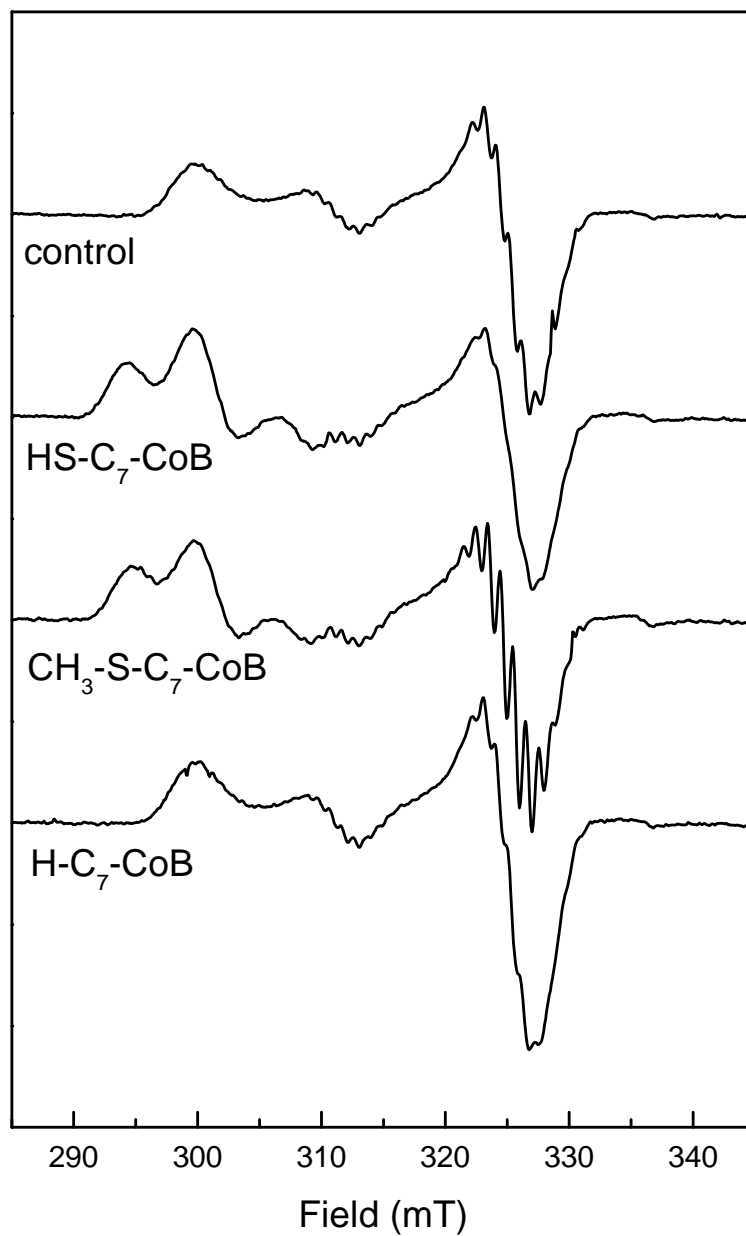


Figure 1-14: Induction of the red2 form with coenzyme B analogs (Different functional groups). All samples contained 10 mM coenzyme M

## CHAPTER TWO

### ANALYTICAL TECHNIQUES

#### 2.1 Electron Paramagnetic Resonance spectroscopy

##### 2.1.1 Introduction and Background

A molecule or atom has discrete (or separate) states, each with a corresponding energy. Spectroscopy is the measurement and interpretation of the energy differences between the atomic or molecular states. With knowledge of these energy differences, you gain insight into the identity, structure, and dynamics of the sample under study.

Electron Paramagnetic Resonance (EPR) spectroscopy or Electron Spin Resonance (ESR) spectroscopy is a technique that involves the absorption of energy from a microwave electromagnetic field by a system containing unpaired electron spins when placed in a strong magnetic field. It probes certain properties and the environment of a paramagnetic center by characterizing the interaction of that center with an applied magnetic field. It involves reorientation of the magnetic moment of an electron as induced by the magnetic field. In principle, EPR is applicable to any species containing one-or-more unpaired electrons. In chemistry and biochemistry, this includes inorganic

and organic free radicals, triplet states (e.g., dioxygen, O<sub>2</sub>), and systems that contain transition metal ions [102].

EPR has been successfully applied to biological systems for studying metal centers, substrate radicals, and redox-active centers in proteins, since the technique can provide information concerning the redox state of the metal, the g-values, ground state, spin hyperfine and zero-field splitting [103].

Since the tertiary structure of metalloproteins is normally diamagnetic, EPR is a standing-out technique to look into the structure of the paramagnetic cofactor in the free enzyme, reaction intermediates and product complexes [104]. It can also be applied to collect kinetic information on reactions that involve paramagnetic species [103].

A diagram of a continuous-wave EPR spectrometer is shown in Figure 2-1. An EPR spectrometer is composed of a main console, magnetic power supply and a microwave bridge. The main console consists of the oscilloscope, detector, and computer field modulation unit that set the center field and sweep range of the applied DC magnetic field. At Auburn University, the microwave cavity is either a high sensitivity perpendicular-mode or a dual-mode. The cavities can be fitted with either a liquid nitrogen finger dewar for measurement at 77 K or with a variable temperature helium flow cryostat for measurements in the 3.8 – 300 K region.

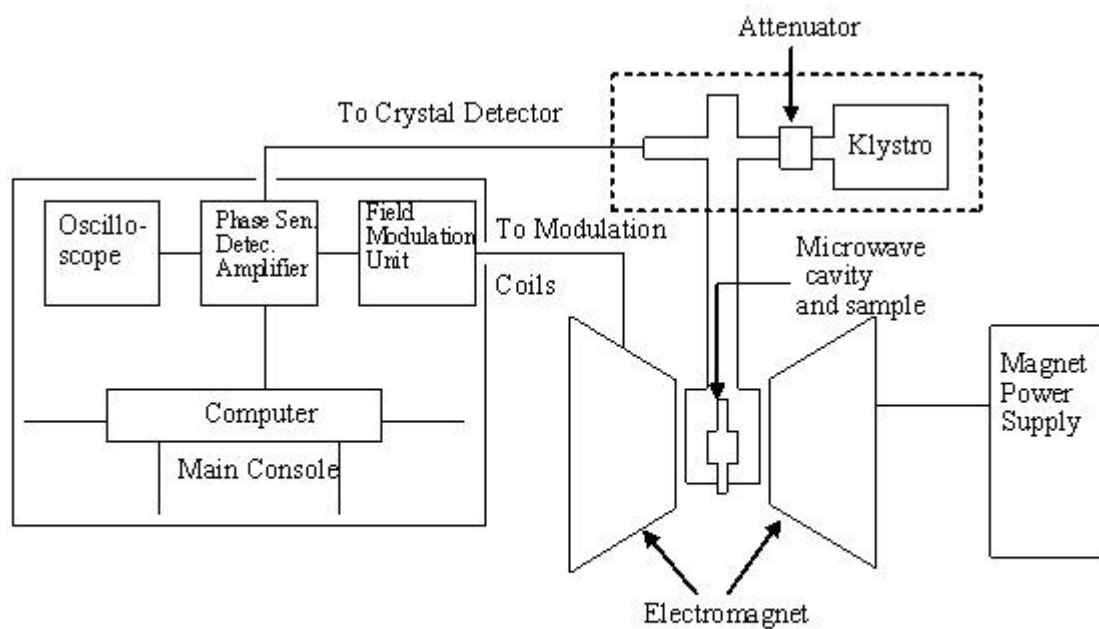


Figure 2-1: Schematic representation of a continuous-wave EPR spectrometer

### 2.1.2 Basic Principles

Spectroscopy provides the way to measure and interpret the energy difference between different atomic and molecular states, following the relationship:

$$E = h\nu \quad (1)$$

In EPR spectroscopy, the energy difference,  $E$ , is dependent on the magnitude of the magnetic moment,  $\mu$ , and on the magnitude of the applied magnetic field,  $B$ :

$$E = -\mu B \quad (2)$$

with

$$\mu = -g\beta S \quad (3)$$

Equation (3) relates the magnetic moment of the electron to the electron spin via the quantities  $g$  and  $\beta$ . The quantity  $\beta$  is the Bohr magneton. It is defined as:

$$\beta = \frac{e}{2m} \frac{h}{2\pi} \quad (4)$$

The first ratio in this definition arises from a derivation of the magnetic moment expected for a classical particle of atomic charge  $e$  and mass  $m$  circulating in a Bohr orbit at the velocity of light. The second ratio, Planck's constant  $h$  divided by  $2\pi$ , is the unit of quantum mechanical angular momentum and is the only correction needed for an orbiting, charged, quantum mechanical particle. The parameter  $\beta$  has the magnitude  $9.285 \times 10^{-21}$  erg<sup>-1</sup> in cgs units and  $9.285 \times 10^{-24}$  CT<sup>-1</sup> in MKS units (1T = 10<sup>4</sup> G).

The  $g$  in equation (3), is called the  $g$  factor or spectroscopic splitting factor. Subsequent to the classical development of the relationship between an electron's magnetic moment and its orbital motion about the nucleus, it was discovered that the electron also had an intrinsic magnetic moment; this usually visualized as arising from the electron spinning about its own axis. The last quantity in equation (3) is  $S$ , the symbol for the total spin associated with the electron; the spin angular momentum.

In the classic description we can say that the magnetic moment of the electron will align itself with the applied field  $B_0$ . The alignment, however, can be parallel or antiparallel. As a result there are two energy levels for the electron in a magnetic field. The two states are labeled by the projection of the electron spin,  $m_s$ , on the direction of the magnetic field. Because the electron is a spin  $\frac{1}{2}$  particle, the parallel state is designated as  $m_s = -\frac{1}{2}$  and the antiparallel state as  $m_s = +\frac{1}{2}$  (Fig. 2-2). The magnitude of this effect varies linearly with the intensity of  $B$ ; the interaction of these magnetic moments with  $B$  is called *Zeeman effect* or *Zeeman interaction*. (Fig. 2-3)

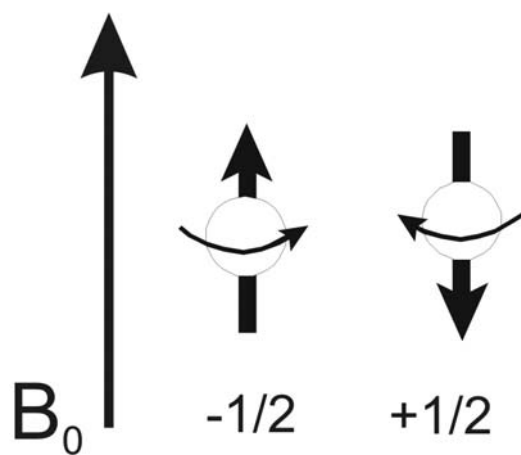


Figure 2-2: Minimum and maximum energy orientations of  $\mu$  with respect to the magnetic field  $B_0$

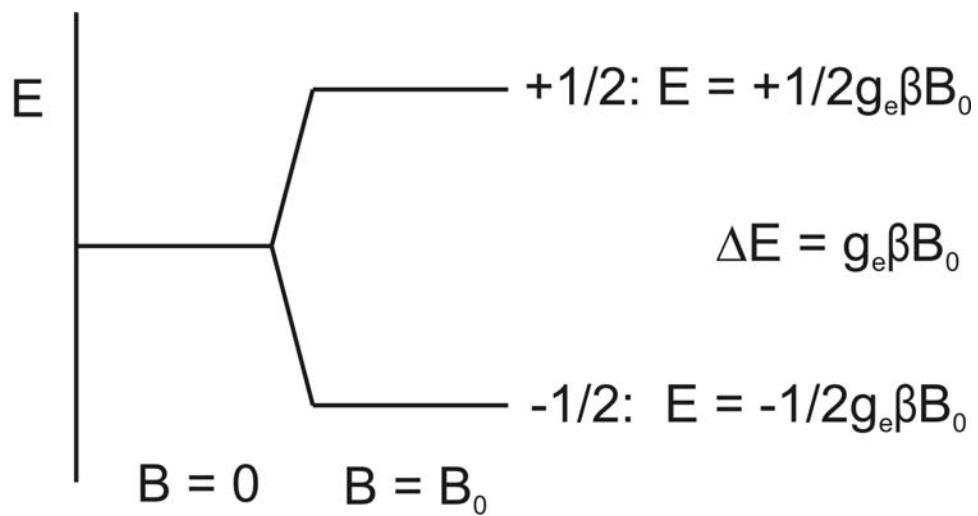


Figure 2-3: Induction of the spin state energies as a function of the magnetic field  $B_0$

The energy of each orientation is the product of  $\mu$  and  $B_0$ . For an electron  $\mu = g_e\beta m_s$ , where  $g_e$  is the spectroscopic  $g$  factor of the free electron and equals 2.0023192778 ( $\approx 2.00$ ). Therefore, the energies for an electron with  $m_s = 1/2$  and  $m_s = -1/2$  are, respectively

$$E_{1/2} = 1/2 g_e\beta B_0 \quad (5)$$

$$E_{-1/2} = -1/2 g_e\beta B_0 \quad (6)$$

In an EPR measurement, the paramagnetic species is placed in a magnetic field that would split the energy levels of the ground states (Fig. 2-4). The  $g$  factor could be determined by the energy different between the two spin levels since  $\beta$  is a constant and  $B_0$  could be obtained. Normally the  $g$  value can be calculated as following [Eq.(7),(8)]:

$$\Delta E = E_{1/2} - E_{-1/2} = h\nu = g\beta B_0 \quad (7)$$

$$g = \frac{h\nu}{\beta B_0} = 714.484 \frac{\nu(GHz)}{B_0(gauss)} \quad (8)$$

Where  $h$  is Planck's constant and  $\nu$  is the microwave frequency.

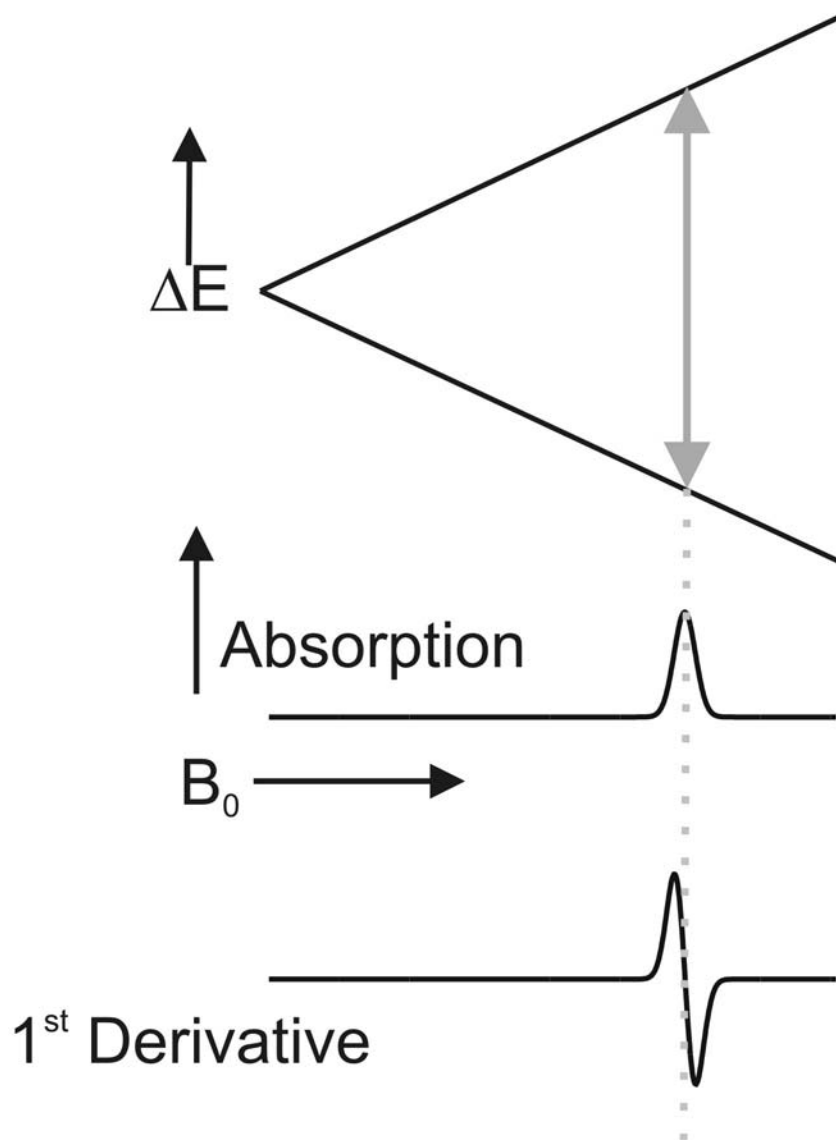


Figure 2-4: Schematic illustration of the splitting of the electron spin states and the resulting absorption signal and its first-order derivative

In the above described EPR experiment we only looked at one molecule in one orientation in a magnetic field. The deviation of the measured  $g$  factor from that of the free electron arises from spin-orbit coupling between the ground state and excited states. Because orbitals are oriented in the molecule, the magnitude of this mixing is direction dependent, or anisotropic. In a low-viscosity solution, all of this anisotropy is averaged out. However, this is not the situation when all the paramagnetic molecules are in a fixed orientation, as in a single crystal. The  $g$  factor of the EPR spectrum of a single crystal would change as the crystal is rotated in the spectrometer, due to  $g$  factor anisotropy. For every paramagnetic molecule, there exists a unique axis system called the principal axis system. The  $g$  factors measured along these axes are called the principal  $g$  factors and are labeled  $g_x$ ,  $g_y$  and  $g_z$ .

Figure. 2-5 shows as an example a molecule where the paramagnetic metal is coordinated by two equal ligands in the  $z$  direction and four different but equal ligands in both the  $x$  and  $y$  directions. As a result the resulting  $g$  factor will be different for the situations where the field  $B_0$  is parallel to the  $z$ -axis or parallel to either the  $x$  or  $y$  axes.

Most EPR spectra of biological transition metals are recorded on frozen solution samples. In these samples, the paramagnets are neither aligned in a set direction, as in an oriented single crystal, nor are they rapidly rotating, as in a low-viscosity solution. The act of freezing fixes the molecules in all possible orientations. Therefore the spectrum of a frozen sample represents the summation of all possible orientations and is called a powder spectrum.

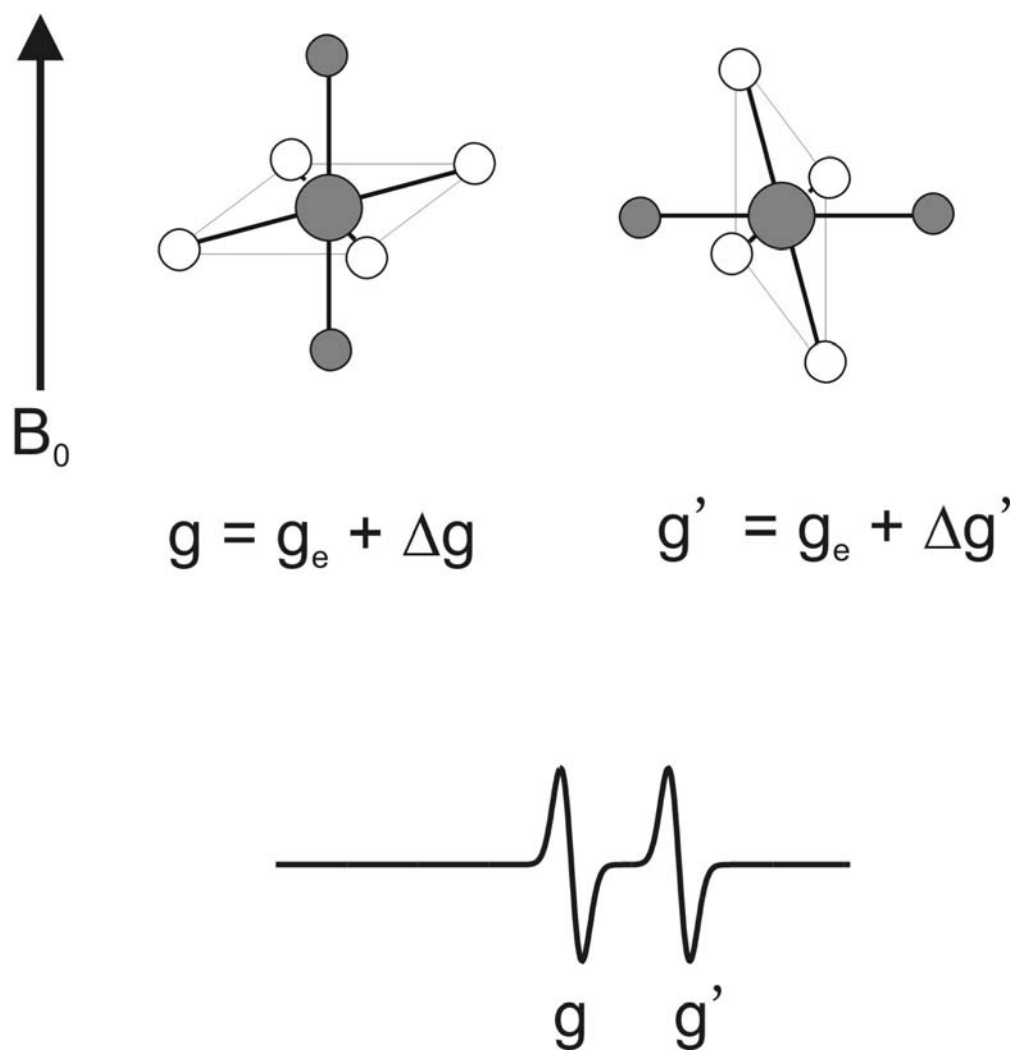


Figure 2-5: A paramagnetic metal molecule coordinated by two equal ligands in the z direction and two different but equal ligands in both the x and y directions

Figure 2-6 shows the absorption and first-derivative spectra for three different classes of anisotropy. In the first class, called isotropic, all of the principal g factors are the same. In the second class, called axial, there is a unique axis that differs from the other two ( $g_x = g_y \neq g_z$ ). This would have been the powder spectrum for our molecule shown in Figure 2-5. The g factor along the unique axis is said to be parallel with axis  $g_z$ :  $g_{//}$ , while the remaining two axes are perpendicular to axis,  $g_z$ :  $g_{\perp}$ . The last class, called rhombic, occurs when all the g factors differ [105-107].

From basic physics theory, we know that a bar magnet would align itself in an outside magnetic field and the energy of the bar magnet could be affected by the interaction with another bar magnet within certain distance. A similar interaction occurs between an unpaired electron and a neighboring magnetic nucleus, which is termed *nuclear hyperfine interaction* (Figs. 2-7 and 2-8). It is called hyperfine interaction if it is due to the nucleus where the unpaired electron originates and it is called superhyperfine interaction if it results from a neighboring nucleus. Therefore we could add this term to the energy expression above (Eq. (7)):

$$\Delta E = h\nu = g\beta B_0 + hAm_I \quad (9)$$

Where A is designated as the Hyperfine Coupling Constant (measured in  $\text{cm}^{-1}$  or MHz),  $m_I$  is the magnetic quantum number for the nucleus and A is called the Hyperfine Splitting Constant. Each nuclear spin would split the EPR line into  $2I+1$  hyperfine lines of equal intensity since there are  $2I+1$  possible  $m_I$  values.

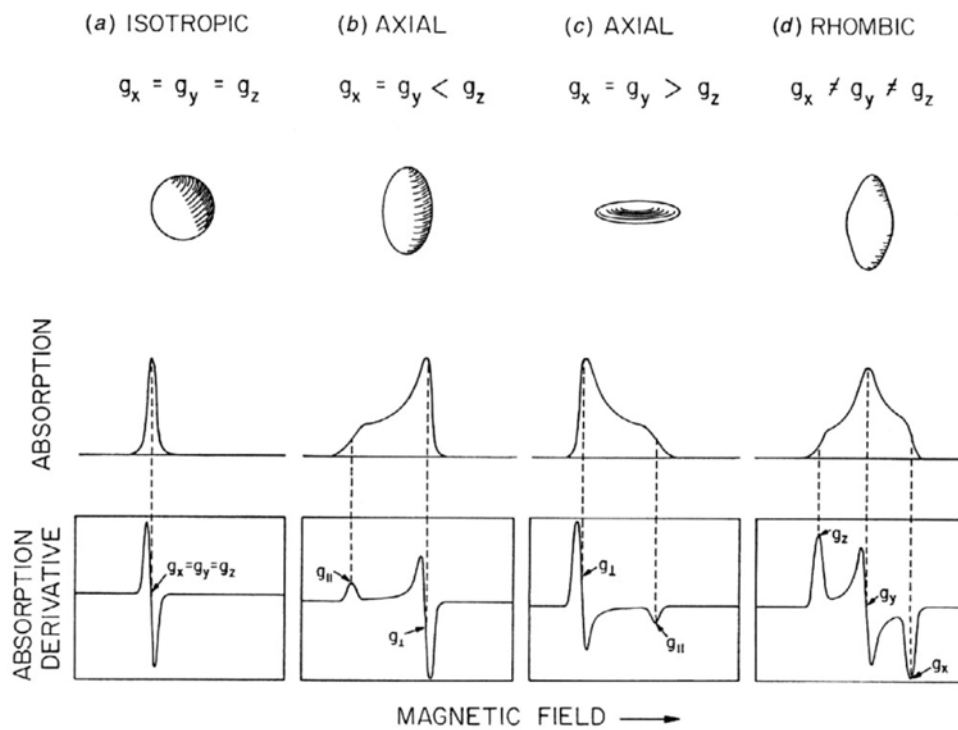


Fig 2-6 The basic spectral envelopes to be found with  $S = 1/2$  paramagnets[102]  
 (Take with permission from [102])

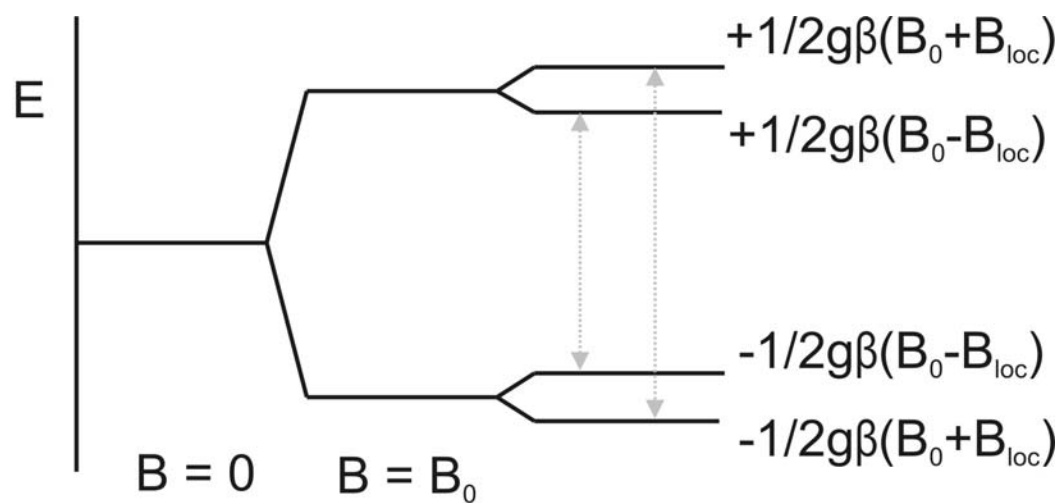


Figure 2-7: Permanent local fields arising from the magnetic moments of magnetic nuclei ( $I=1/2$ )

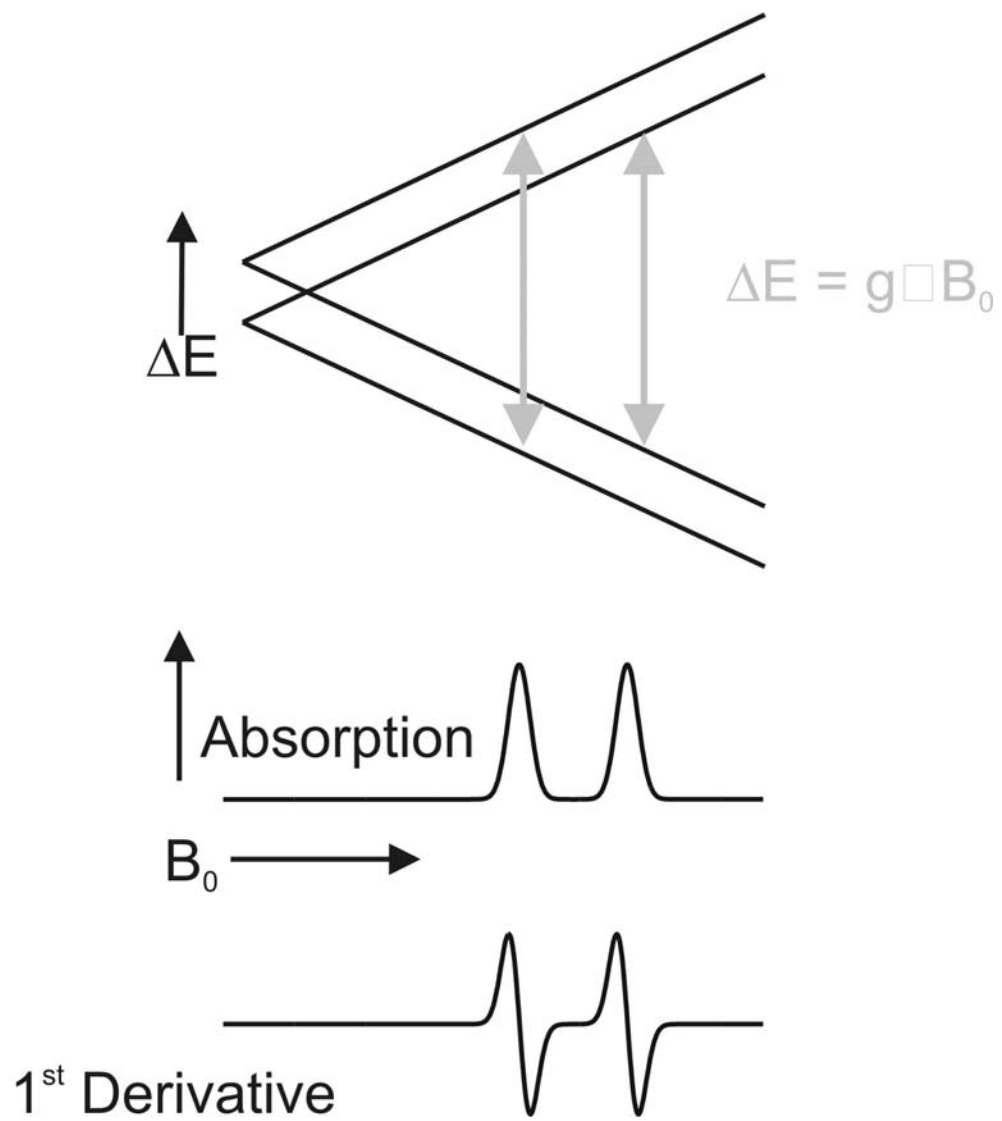


Figure 2-8: EPR experiment for a single electron interacting with a magnetic nucleus with nuclear spin ( $I=1/2$ )

Table 2.1 gives an overview of nuclei and their nuclear spin that have some relevancy to the research presented here.

The nuclear hyperfine interaction contains both an isotropic and an anisotropic contribution. For small molecules in solution, the anisotropic contribution to the nuclear hyperfine interaction is averaged out so that the EPR spectra of small molecules in solution would exhibit finely resolved nuclear hyperfine structure arising only from the isotropic effect [103].

The effects the nuclear spin of the parent nucleus or a neighboring nucleus can have on the shape of the EPR signal is shown in Figure 2-9. The top spectrum shows the spectrum obtained for MCR in the paramagnetic  $\text{Ni}^{1+}$  ( $d^9$ ) state. The spectrum is not smooth like the examples in Figure 2-6, but shows a so-called superhyperfine pattern due to the four nitrogen ligands, that are coordinated to the nickel in  $F_{430}$  (Fig. 1-2). The nitrogen nucleus has a nuclear spin  $I = 1$ . With 4 nitrogen ligands present the hyperfine pattern becomes quite complex. The superhyperfine lines resulting from the four nitrogen ligands are clearly detected on the  $g_{\perp}$  peak. The hyperfine structure on  $g_{//}$  peak is not that obvious but still recognizable. In order to assure the signal detected is from nickel, the enzyme was also obtained from cells grown on  $^{61}\text{Ni}$  ( $I = 2/3$ ) and the spectrum was measured for comparison. The presence of the  $^{61}\text{Ni}$  nucleus causes a clear split of the  $g_{//}$  peak into four peaks. This effect, however, is much smaller for the  $g_{\perp}$  peak. In the last

Table 2-1: Nuclear spin of some nuclei that are important for the research presented in this dissertation [108]

Isotope	Nuclear Spin (I)	% Abundance
$^1\text{H}$	1/2	99.9
$^2\text{H}$	1	0.02
$^{12}\text{C}$	0	98.9
$^{13}\text{C}$	1/2	1.1
$^{14}\text{N}$	1	99.6
$^{15}\text{N}$	1/2	0.37
$^{16}\text{O}$	0	99.8
$^{17}\text{O}$	5/2	0.037
$^{32}\text{S}$	0	95.0
$^{33}\text{S}$	3/2	0.76
$^{61}\text{Ni}$	3/2	1.19

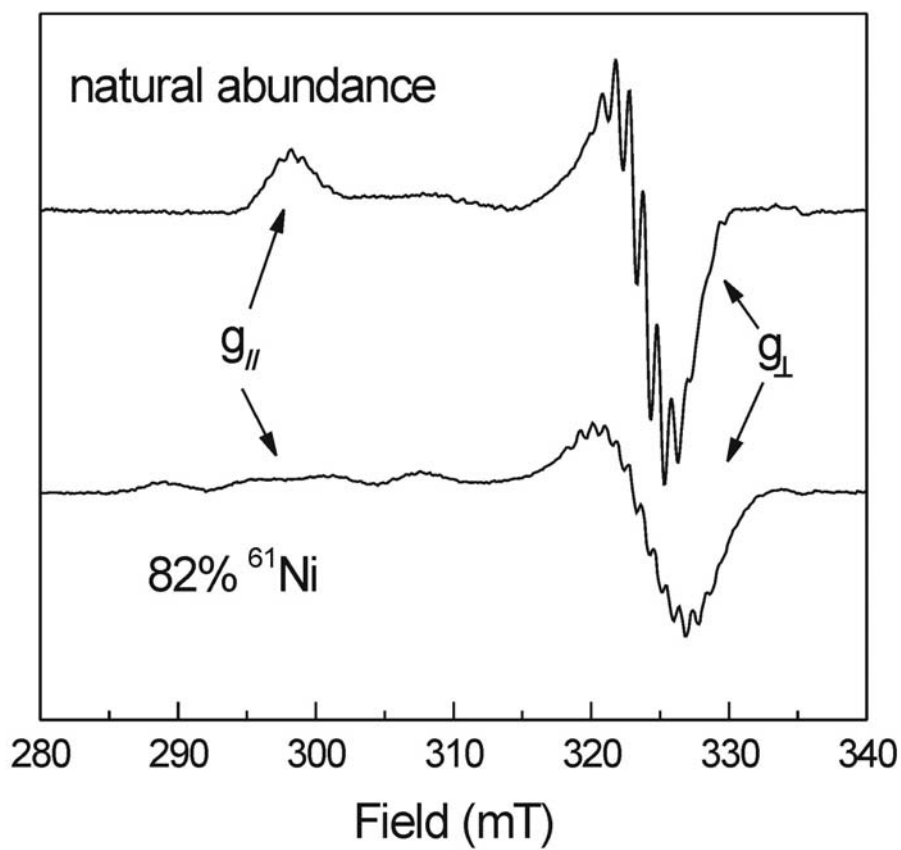


Figure 2-9. EPR spectra of methyl-coenzyme M from *Methanothermobacter marburgensis* in the red1 state. The top spectrum show the spectrum obtained after growing cells with natural abundance nickel isotopes. The bottom spectrum shows the spectrum obtained after growing cells on  $^{61}\text{Ni}$  ( $I = 3/2$ ).

case the hyperfine is unresolved and is mainly detectable as a broadening of the line width of the EPR signal.

In the research presented in chapter 4, isotopic labeling studies are described, that were undertaken to prove the presence of additional ligands to the nickel. As in the example with  $^{61}\text{Ni}$ , introducing an additional nuclear spin in the vicinity of the electron spin does not have to result in a clearly detectable (super)hyperfine pattern. With the complementary technique of electron nuclear double resonance spectroscopy, however, it is still possible to measure the hyperfine coupling constants  $A$ .

## **2.2 Electron Nuclear Double Resonance Spectroscopy**

Electron Nuclear Double Resonance (ENDOR) spectroscopy is an important spectroscopic technique that derives from the basic EPR experiment. ENDOR spectroscopy was first established by Feher in 1956 [109] and was first used on metalloproteins by Eisenberger and Pershan [110]. It complements the EPR technique by recovering the hyperfine coupling constants for nuclei paramagnetic center unresolved on the EPR signal. It measures the nuclear magnetic resonance (NMR) spectra of nuclei associated with the electron spin [111]. The occurrence of a nuclear resonance transition is not detected in a direct form but as an intensity change in the EPR signal. Therefore this technique is classified as a double resonance technique which has two major advantages: direct stimulation of NMR transitions enhances the spectral resolution by orders of magnitude compared with EPR; detection of the effect utilizing the Boltzmann

population difference of electron spin energy levels increases the sensitivity by orders of magnitude compared with NMR [112]. Therefore, ENDOR lines are usually sharper than EPR lines. The hyperfine coupling constants, undetectable by ordinary EPR spectroscopy, can often be determined by ENDOR.

ENDOR has contributed enormously to our understanding of metal coordination in proteins and chelate complexes and of the electronic structure of radicals. The chief use of ENDOR in the metalloprotein investigations is that it enables weaker hyperfine interactions to be resolved. In ENDOR measurements, nuclei can be unambiguously identified by their Larmor frequency. The spectral density can be much lower, because each nuclear interaction adds to the number of lines in an ENDOR spectrum whereas in EPR the effect is multiplicative. This fact is a consequence of the different selection rules for the two spectroscopies,  $\Delta m_s = \pm 1$ ,  $\Delta m_l = 0$  for EPR versus  $\Delta m_s = 0$ ,  $\Delta m_l = \pm 1$  for ENDOR (see Figure 2-10). Quadrupolar interactions (with nuclei having  $I > 1/2$ ) can be measured directly, giving further structural information. In this case, whether all lines are observed depends on the relative magnitudes of the nuclear Zeeman frequency, the nuclear hyperfine and quadrupolar coupling constants, and on the various relaxation processes that govern the ENDOR intensities. Hyperfine interactions can be measured more accurately. In some cases “single-crystal” quality data can be extracted from powder spectra because measuring ENDOR at different parts of an anisotropic EPR spectrum mean that considerably more detail of the environment of the paramagnetic centre up to a distance of 8 Å can be determined by ENDOR.

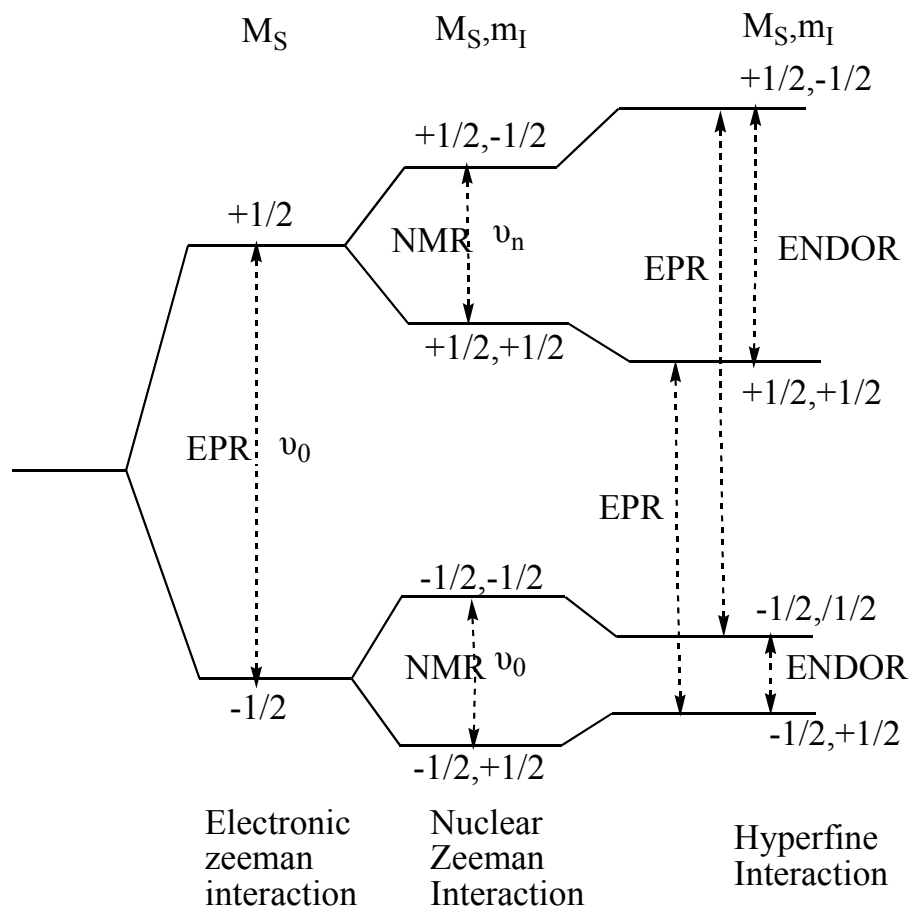


Figure 2-10 The effect of electronic and nuclear Zeeman interactions and of the hyperfine interaction

The principle disadvantage of continuous wave (CW) ENDOR is the greatly reduced sensitivity compared with EPR. This means that samples need to be more than 10 fold concentrated to yield acceptable ENDOR spectra.

The general theory of ENDOR has been covered in detail by Swartz *et al.*, Atherton, Dorio and Freed, and Schweiger [113-116]. Therefore, only the basic theory necessary for understanding the work described in this dissertation will be described here.

Based on the classic Schrödinger equation and the conventional “Spin Hamiltonian” [117] and considering nuclear spins factor, the spin Hamiltonian for the simplest system with effective electron spin  $S' = 1/2$  and a single nuclear with  $I = 1/2$  can be described as:

$$H = g \beta_e B S' - g_n \beta_n B I + S' A I \quad (1)$$

Where  $\beta_e, \beta_n$  are the electronic and nuclear magnetons,  $g, g_n$  are the electronic and nuclear  $g$ -tensor describing the anisotropic interaction between the magnetic field  $B$  and the electronic spin  $S'$ , and  $A$  is the anisotropic hyperfine tensor describing the interaction between the electronic and nuclear spins. In this equation, the first term is the electronic Zeeman interaction, the second is the nuclear Zeeman interaction, and the third is the hyperfine interaction. The effects of these three terms are shown in Figure 2-10.

It is the  $\Delta m_l = \pm 1$  transitions that ENDOR is able to detect while the  $\Delta m_s = \pm 1$  is detected by EPR. The radiofrequencies where the ENDOR lines are observed ( $\nu_{\pm}$ ) are related to the NMR nuclear Lamor frequency ( $\nu_n$ ) of the magnetic nucleus and the hyperfine coupling constant ( $A$ ):

$$\nu_{\pm} = |\nu_n \pm A/2|$$

In the case when  $|\nu_n| > |A/2|$ , it means the nuclei is weakly coupled, whereas  $|\nu_n| < |A/2|$  indicates strongly coupled nuclei. And the intermediate case when  $|\nu_n| = |A/2|$  is named cancellation condition.

In CW ENDOR, the EPR signal at a given field is partially saturated by an increase of microwave power [109]. When the radio frequency matches a nuclear frequency, in another word, when a nuclear transition is induced, the population of the partially saturated EPR transition will be changed and the recovery of this signal will be realized by detecting net mw absorption. This allows the determination of the hyperfine coupling constant. In fact, it results in a better peak separation in the ENDOR spectra due to the magnetic-field dependence of  $\nu_n$  [118].

ENDOR spectra are supposed to be sharper than the original EPR spectra because of the long relaxation times of most nuclei, which provide us with more information of hyperfine splittings that were undetectable in the EPR spectrum. It is indeed a technique with great advantage to interpret broad lines in EPR spectra with better resolved hyperfine structure.

### 2.3 X-ray Absorption Spectroscopy

X-ray absorption spectroscopy is an element-specific probe of the local structure (short range) of elements in a sample. Since X-rays have wavelengths in the order of atomic dimensions, these highly energetic photons can be used to sample the molecular structure of materials. One example of this use is X-ray diffraction from crystalline samples resulting in a complete three-dimensional (3D) crystal structure.

A typical X-ray absorption spectrum is shown in Figure 2-11. At a well-defined X-ray photon energy, a sharp rise in the absorption coefficient is observed. This rise is called an X-ray absorption edge and is due to electron dissociation from a core level of one type of atom (the absorbing atom) in the sample. The photon energy is equal to the ionization potential of a bound electron. Spectral features in the edge region are sensitive to the electronic structure of the absorbing atom and can often be used to identify the geometric arrangement of atoms around the absorbing atom. The exact energy of the edge is dependent on the charge density at the absorbing atom and can be used to determine the valence or oxidation state.

The XAS spectrum is generally divided into 4 sections: 1) pre-edge ( $E < E_0$ ); 2) X-ray absorption near edge structure (XANES), where the energy of the incident X-ray beam is  $E = E_0 \pm 10$  eV; 3) near edge X-ray absorption fine structure (NEXAFS), in the region between 10 eV up to 50 eV above the edge; and 4) extended X-ray absorption fine structure (EXAFS), which starts approximately from 50 eV and continues up to 1000 eV above the edge.

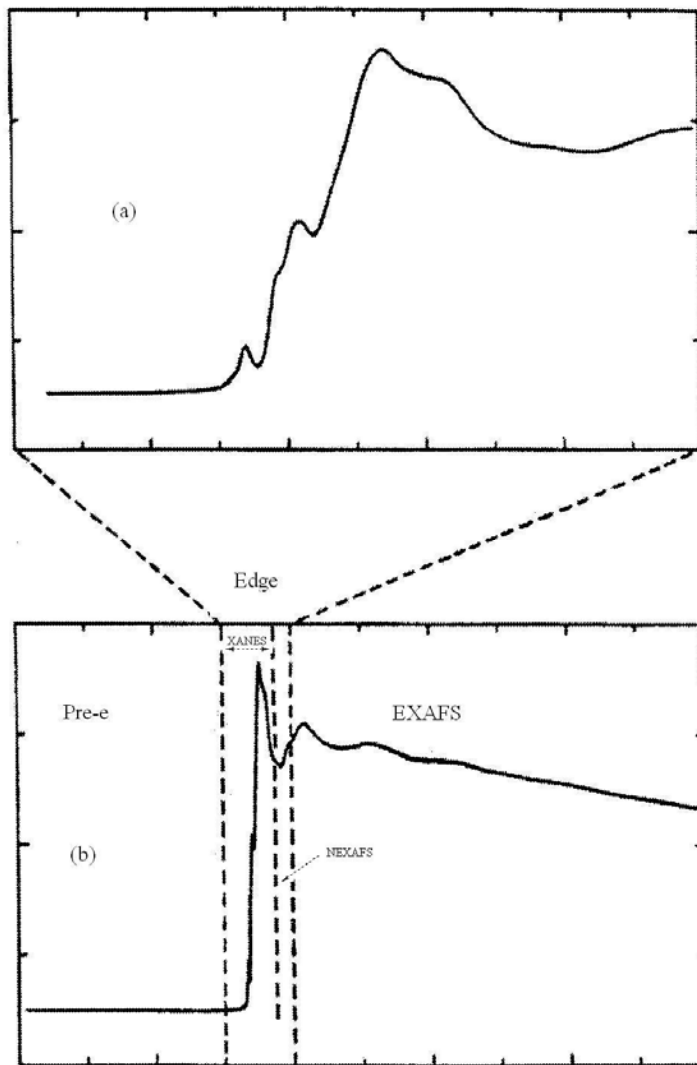


Figure 2-11 An X-ray absorption spectrum plotted as absorption coefficient versus photon energy. (a) Expanded view of the edge region. (b) Full spectrum showing the pre-edge, edge and extended X-ray absorption fine structure (EXAFS) regions[108]. (Take with permission from [108])

The minor features in the pre-edge region are usually due to the electron transitions from the core level to the higher unfilled or half-filled orbitals (e.g.,  $s \rightarrow p$ , or  $p \rightarrow d$ ). In the XANES region, transitions of core electrons to non-bound levels with close energy occur. Because of the high probability of such transition, a sudden raise of absorption is observed. In NEXAFS, the ejected photoelectrons have low kinetic energy ( $E-E_0$  is small) and experience strong multiple scattering by the first and even higher coordinating shells. In the EXAFS region, the photoelectrons have high kinetic energy ( $E-E_0$  is large), and single scattering by the nearest neighboring atoms normally dominates.

As shown in Figure 2-12, scanning the electron energy cause every atom sample to give rise to several absorption edges as the photon energy matches the ionization potential of each bound electron (1s, 2s, 2p<sub>1/2</sub>, 2p<sub>3/2</sub>, ...). These X-ray absorption edges are named for the shells of the Bohr atom (K edges for  $n = 1$ , L edges for  $n = 2$ . etc.) as indicated in Figure 2-12. In general, the higher the oxidation state of the absorbing atom, the higher the energy of X-ray absorption edge.

The X-ray absorption spectrometer required to measure an X-ray absorption spectrum contains all the basic components found in a typical UV-VIS spectrophotometer: a source, a monochromator, and detector. Each of these components is specifically adapted for the X-ray region of the spectrum.

The EXAFS technique is inherently insensitive. The X-ray source must be powerful, because the EXAFS modulations are always less than 1% of the size of the edge. There are four main types of X-ray sources: fixed-anode source; rotating anodes; plasma

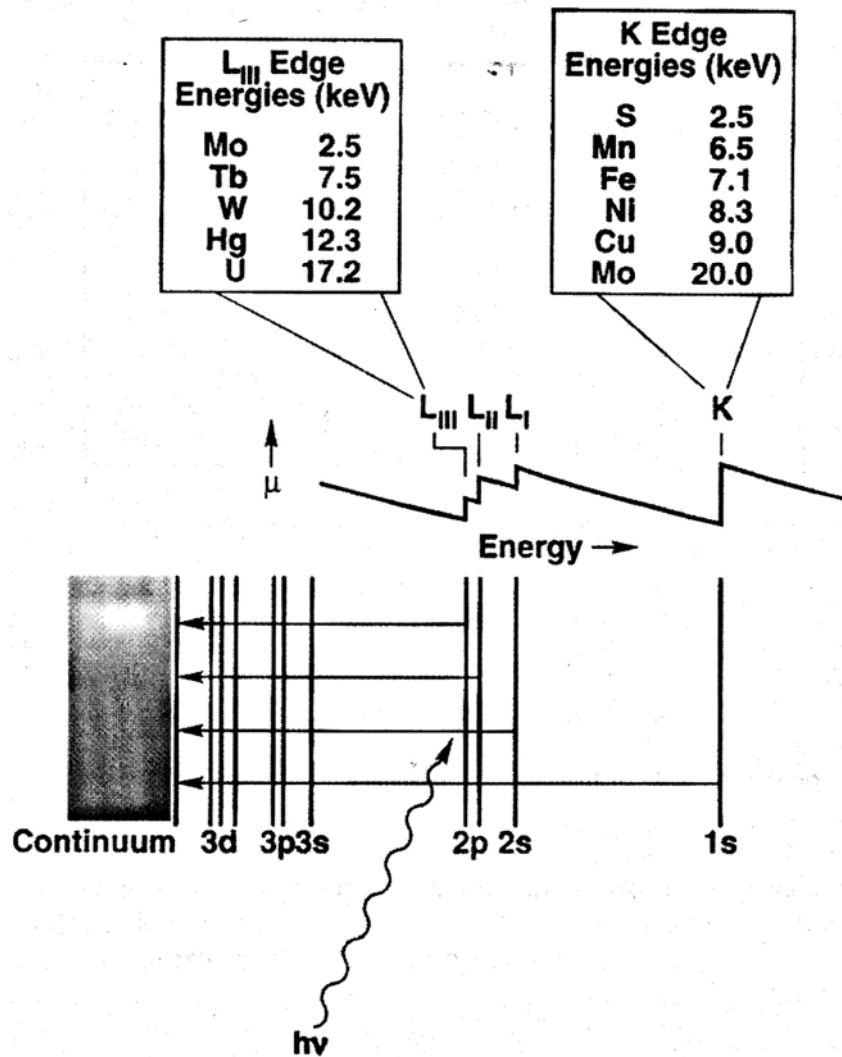


Figure 2-12 Schematic diagram relating the X-ray absorption spectrum to the atomic energy level diagram. X-ray photon absorption is indicated by the arrows in the energy level diagram, each giving rise to an absorption edge in the top spectrum. Some L<sub>III</sub> and K X-ray absorption edge energies are tabulated above the diagram[108]. ( Take with permission from [108] )

sources; and electron (or positron) storage rings. An XAS requires scanning the X-ray photon energy, so a source with high intensity throughout a range of energy is very important.

Because X-rays penetrate most optical materials, dispersive optical elements are not able to be used for the hard X-ray region. For this reason, X-ray monochromators utilize Bragg reflection from single crystals for monochromatization.

For quantitative measurement of XAS, detectors are required to measure the flux of the X-ray beam. Because hard X-rays can ionize gases, a simple detector can be built to measure the amount of ionized gas per unit time which is proportional to X-ray flux.

There are two main types of data collection: transmission XAS and fluorescence excitation XAS. Transmission XAS measures the X-ray photon intensity ( $I_0$ ) incident on the sample and intensity ( $I$ ) transmitted through the sample. The  $\ln(I_0/I)$  is proportional to the absorption coefficient. In fluorescence excitation XAS, fluorescent X-ray photons are counted as the photon energy, and generating a signal proportional to the absorption coefficient ( $F/I_0$ ).

Figure 2-13 shows an example of data reduction for EXAFS analysis; (a) Fluorescence excitation XAS data (solid line) are corrected by subtraction of a pre-edge background (dashed line); (b) a smooth curve (dashed line) is fit to the pre-edge-subtracted data (solid line) by a cubic spline procedure to yield (c) the EXAFS data. (d) The EXAFS data displayed as a function of photoelectron wave vector,  $k$ , and then (e) weighted by  $k^3$ .

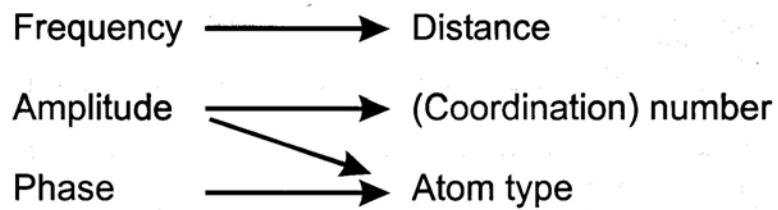
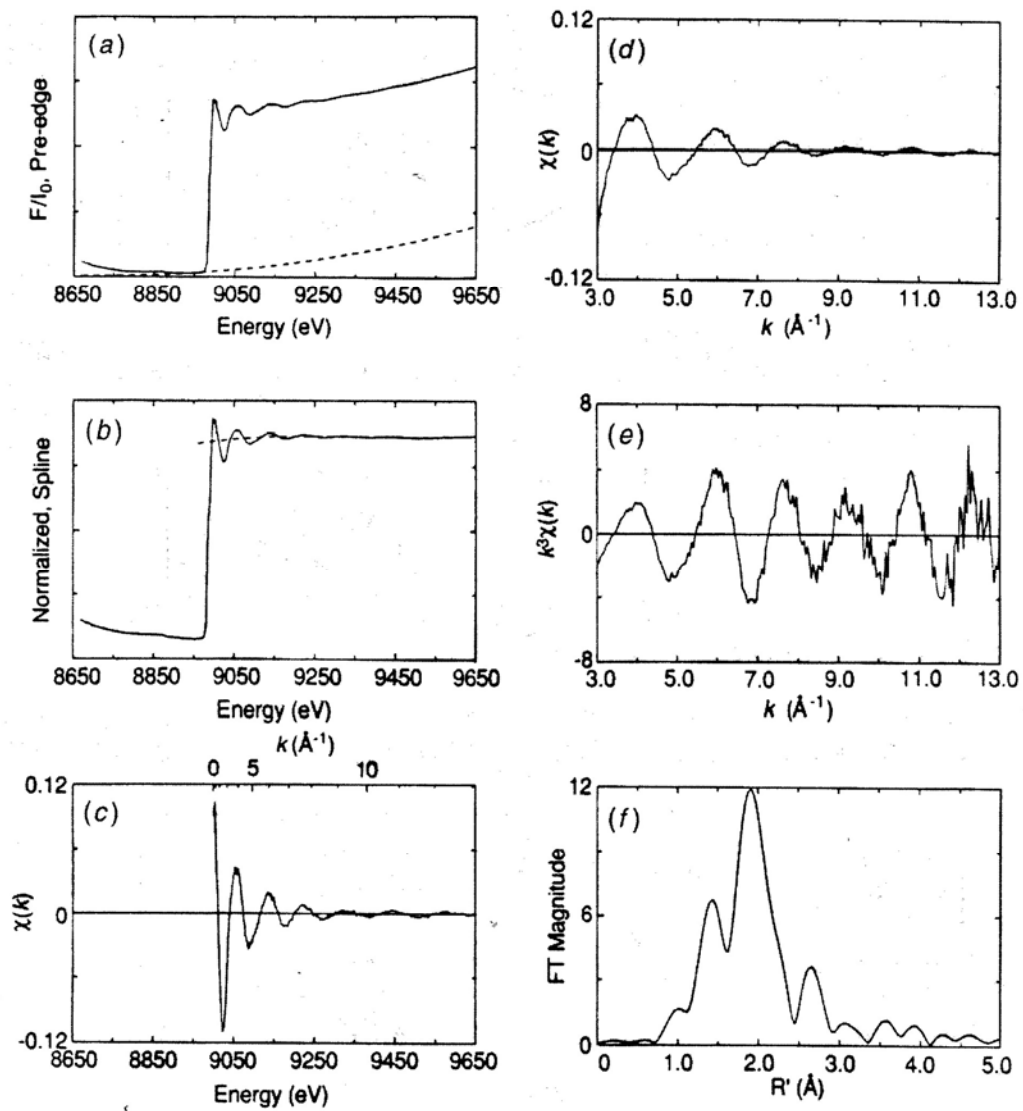


Figure 2-13 Example of data reduction for EXAFS analysis[108]. (Take with permission

from [108])

(f) The magnitude of the FT of  $k^3\chi(k)$  data in (e) displayed as a function of the phase-shifted distance,  $R'$ .

At a given photon energy, a longer atom-atom distance implies that more periods of the photoelectron wave are required to cover the distance from one atom to the other and back. It takes less of a change for a longer distance in photoelectron wavelength to go through one period of the interference. Therefore the absorption coefficient is modulated at a higher frequency. It is the frequency-distance relationship. The absorption coefficient is modulated at a higher frequency in  $E$  (or  $k$ ).

In a coordination site with two identical atoms at the same distance from center atom, each will contribute an identical sine wave to the EXAFS that simple add together to give a sine wave with twice the amplitude. But it only yields radial structural information. So it does not matter how the two atoms are arranged around center atom, only that they are at the same distance. This radial dependence causes the concept of “shells” of atoms, which are defined as a collection of atoms all residing at the same distance from the absorbing atom. One shell of atoms only causes one sine wave in EXAFS.

Since the size of phase shifts depends on the electron density at atoms (a given absorbing atom), different scattering atom types introduce different phase shift, yielding EXAFS components with different phases. The heavier scattering atoms are better scatterers, yielding EXAFS components with larger amplitudes (for a given number of atoms). That is the relationship between amplitude and atom type.

Figure 2-14 shows the comparison of Ni K-edge X-ray absorption spectra for a series of Ni (II) compounds of varying site symmetry. (a) Approximately tetrahedral compounds Ni [tropocoronand-(CH<sub>2</sub>)<sub>6</sub>, (CH<sub>2</sub>)<sub>6</sub>] (solid line) and [Ni (SPh)<sub>4</sub>]<sup>2-</sup> (dotted line). (b) Approximately square pyramidal compound [Ni (tetramethylcyclam) Br]<sup>+</sup>. (c) Approximately octahedral compounds [ Ni (1, 4, 7 – triazacyclononane)<sub>2</sub>]<sup>2+</sup> (solid line) and [ Ni (1, 4, 7 – trithiacyclononane)<sub>2</sub>]<sup>2+</sup> (dotted line). (d) Approximately square planar compounds [Ni (phthalocyanine)] (solid line), [Ni (maleonitriledithiolate)<sub>2</sub>]<sup>2-</sup> (dotted line).

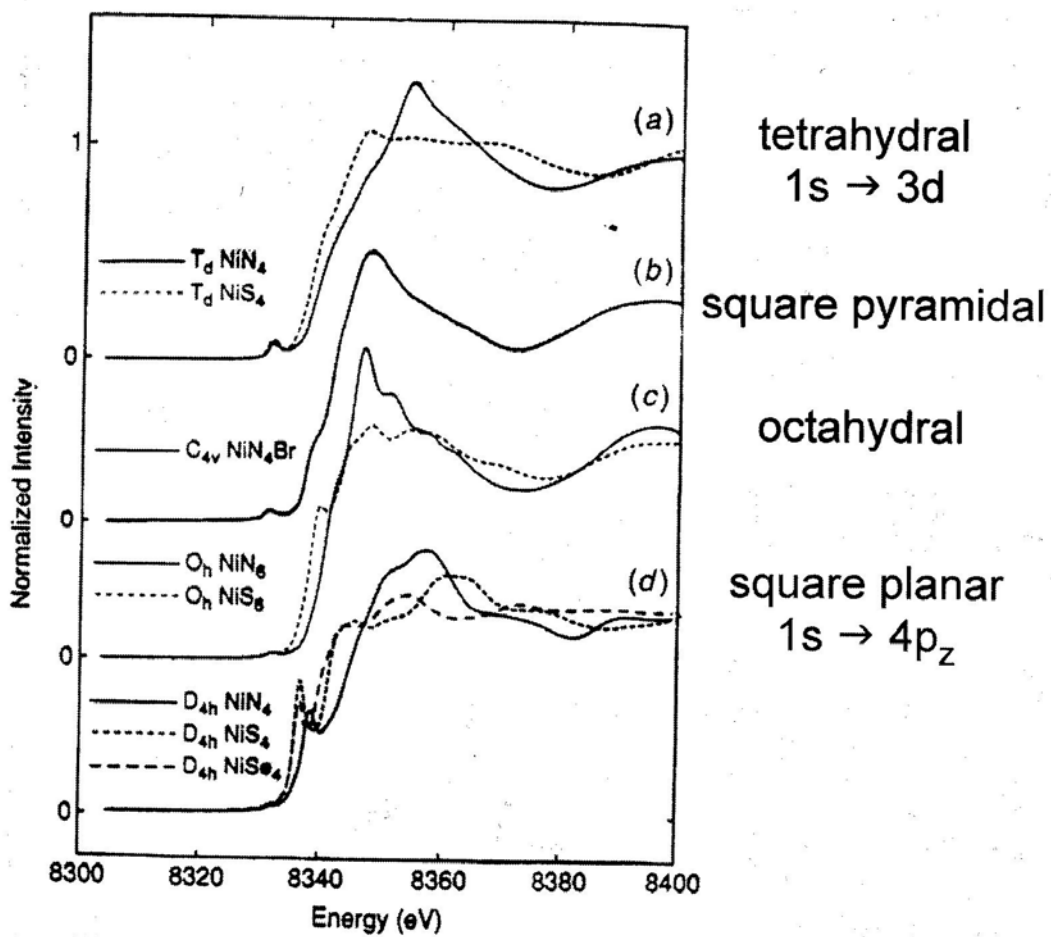


Figure 2-14 Comparison of Ni K X-ray absorption edge spectra for a series of Ni(II) compounds of varying site symmetry [108]. (Take with permission from [108])

## CHAPTER THREE

### MATERIALS AND METHODS

#### 3.1 Biochemical and Chemical Reagents

Tris base, Taps, sodium dithionite, potassium permanganate, ammonium acetate, methyl iodide, thiourea, dichloromethane, sodium bicarbonate, iodine, potassium iodide, sodium thiosulfate, benzene, 1,4-dioxane, *N*-hydroxysuccinimide, *N,N'*-dicyclohexylcarbodiimide, *O*-phospho-L-threonine, 5,5'-dithiobis(2-nitrobenzoic) acid, triethylamine, tetrahydrofuran, acetonitrile, potassium borohydride, anhydrous magnesium sulfate, <sup>13</sup>C-bromomethane, Amberlite XAD-2, Ellman's Reagent (5,5'-dithiobis-(2-nitrobenzoic acid)), nitrilotriacetic acid, iron(II) chloride, Molybdenum(II) chloride, sodium molybdate dihydrate, nickel(II) chloride, resazurin, methyl iodide, Ti(III) chloride and Cob(II)alamin were purchased from Sigma-Aldrich. Potassium phosphate (monobasic anhydrous and dibasic anhydrous), 2-propanol, absolute ethanol, glycerol, magnesium sulfate, magnesium chloride, ammonium chloride, sodium chloride, and ammonium sulfate were from Fisher Biotech. Coenzyme M was from Merck. 7-Bromoheptanoic acid was from Karl Industries Inc. Q-sepharose, and PD-10 columns were purchased from Amersham Biosciences (Piscataway, NJ). Centricon ultrafiltration units were from Millipore (Bedford, MA). Standard anaerobic buffers were used for all purifications and experiments. The buffers were filtered (0.22 μm) and subsequently

boiled under a nitrogen gas flow. The buffers were transferred, under a nitrogen atmosphere, to stoppered bottles and were stirred under vacuum for a period of 1-2 h. This procedure removes all molecular oxygen. The buffers were directly used or were stored after nitrogen gas was added to the head space of the bottles to create an overpressure of 0.3 Atm. Buffers stored this way will stay anaerobic for several months.

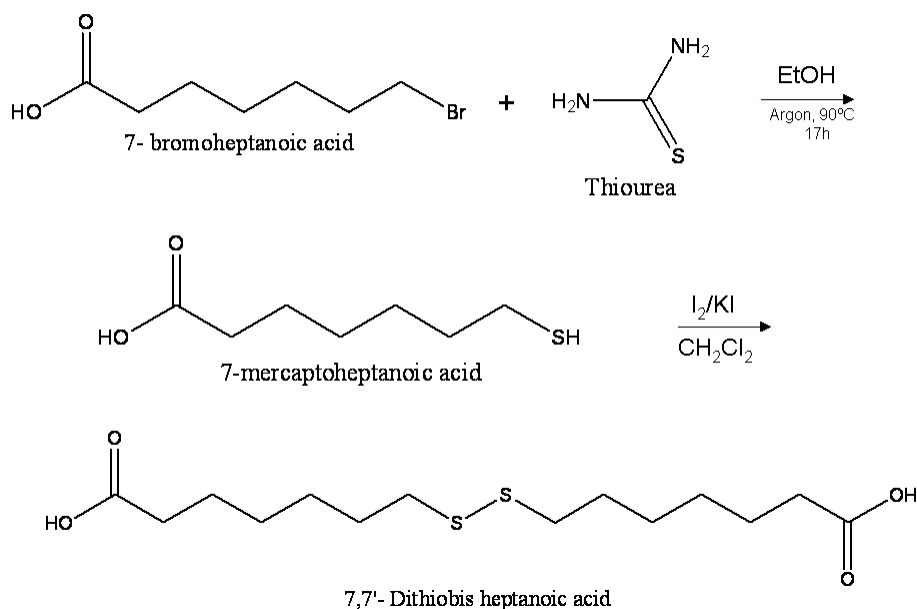
### **3.2 Synthesis and Purification of 2-Methylthioethane Sulfonate (Methyl-coenzyme M)**

Methyl-coenzyme M was synthesized from coenzyme M (2-mercaptoethanesulfonate) by methylation with methyl iodide as described in the literature [119]. Coenzyme M (3 mmol) was incubated for 12 h with 6 mmol of methyl iodide in 5 ml of a 33% aqueous ammonia solution under a 100% N<sub>2</sub> atmosphere. After incubation for 12 h at room temperature the reaction mixture was evaporated to almost dryness and subsequently lyophilized. The dry yellow residue was dissolved in 10 ml distilled water. Aliquots of the solution of 5-ml were loaded on a Q-Sepharose column (volume 30 ml) and a linear gradient of 0 to 1 M ammonium carbonate was applied for elution. Ammonium carbonate was used instead of hydrochloric acid to elute methyl-coenzyme M from the Q-Sepharose column since methyl-coenzyme M in the non-dissociated sulfonic acid form and water form an azeotropic mixture. Eluate was collected and tested for methyl-coenzyme M by thin layer chromatography on Kieselgel 60 F<sub>254</sub> (Merck) with butanol/acetic acid/water (2:1:1) as the mobile phase. Methyl-coenzyme M generally

eluted from the column between 250 mM and 350 mM ammonium carbonate. Fractions containing methyl-coenzyme M were combined and lyophilized, which removes the ammonium carbonate. Subsequently, the powder in the lyophilizer was heated to 60°C to remove remaining traces of iodine. Generally 2 g of a dry white powder was obtained at the end of the procedure. The purity of the compound was checked with NMR spectroscopy (Figure 3-1).

### 3.3 Synthesis of [(+)-(2*S*,3*R*)-*N*-[7-Mercaptoheptanoyl]-*O*-phospho-L-threonine (Coenzyme B)

#### 3.3.1 7, 7'-Dithioheptanoic Acid



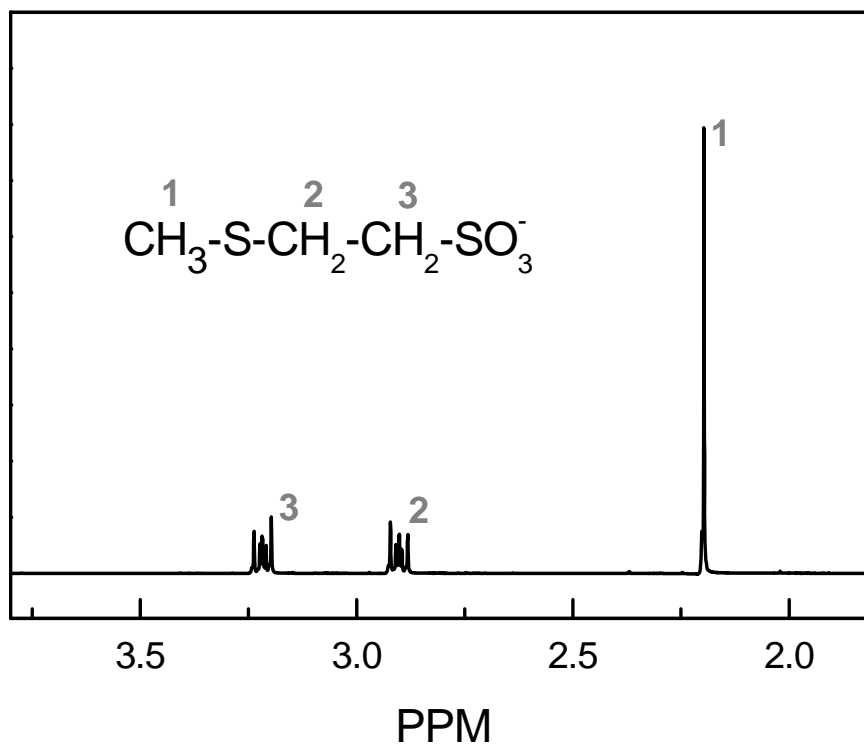
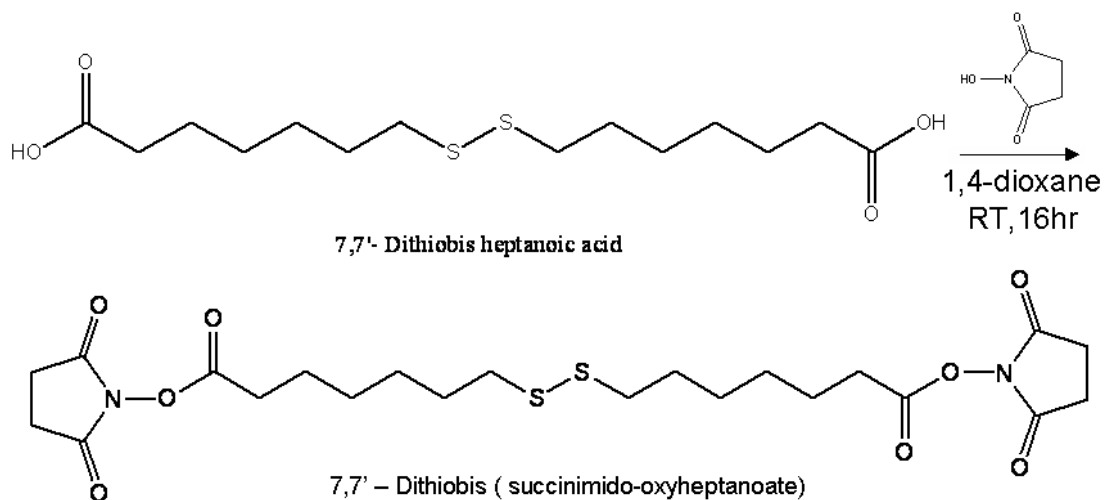


Figure 3-1: NMR spectra of methyl-coenzyme M.

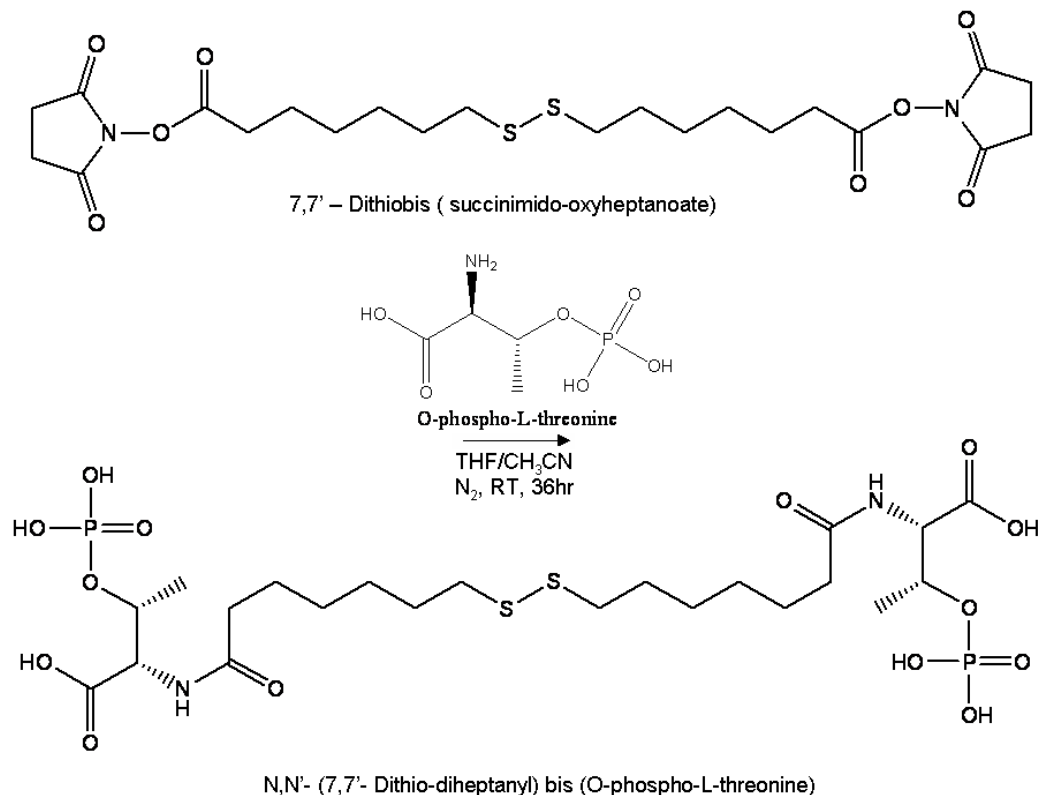
7-Mercaptoheptanoic acid was synthesized by dissolving 17.4 g (228 mmol) of thiourea in a stirred solution of 7-bromoheptanoic acid (9.6 g, 46.6 mmol) in 110 ml of ethanol. This mixture was refluxed under argon at 90°C for 17 h, cooled to room temperature, and 25 ml of a 60% aqueous solution (w/v) of sodium hydroxide was added. The mixture was refluxed under argon for an additional 2 hours, and cooled to room temperature. The yellow/white solution was concentrated. A 100 ml aqueous solution of 1M HCl was added followed by 20 ml concentrated HCl. The thiol was extracted 3 times with 100 ml dichloromethane. The dichloromethane phase was extracted 3 times with 150 ml of an aqueous solution of 1 M sodium bicarbonate. The aqueous extract was acidified with HCl to a pH of 1-2, and extracted 3 times with 200 ml dichloromethane. The organic phase was filtered over cotton and concentrated to 70 ml. The thiol was oxidized to a disulfide by mixing the dichloromethane phase with an aqueous solution of 10% (w/v) iodine and 20% (w/v) potassium iodide until the brown color persisted. The aqueous phase was removed and the dichloromethane phase was washed 3 times with an aqueous solution of 1M sodium thiosulfate, and three times with water. The organic phase was filtered over cotton, dried over anhydrous magnesium sulfate, and concentrated under vacuum. The product was crystallized twice from benzene (or toluene), and dried for two days under high-vacuum, to give 3.3 g (46%) of white crystals. Mp is 70°C

### 3.3.2 7,7'-Dithiobis (succinimido-oxyheptanoate)



7,7'-Dithiodiheptanoic acid (388 mg, 1.2 mmol) was dissolved in 8 ml of 1,4-dioxane at room temperature. Subsequently, 290 mg (2.5 mmol) of N-hydroxysuccinimide was added under stirring. A solution of 505 mg (2.4 mmol) dicyclohexylcarbodiimide in 3 ml 1,4-dioxane was added drop-wise and the resulting solution was stirred for 16 h at room temperature. The precipitated dicyclohexylurea was removed by filtration over a glass filter and the filtrate was washed 2 times with 5 ml 1,4-dioxane, and dried (to a clear oil) under vacuum. The product was recrystallized twice from boiling 2-propanol, and dried for 1 day under high vacuum to give 384 mg (62%) of white crystals. Mp is 105-106 °C

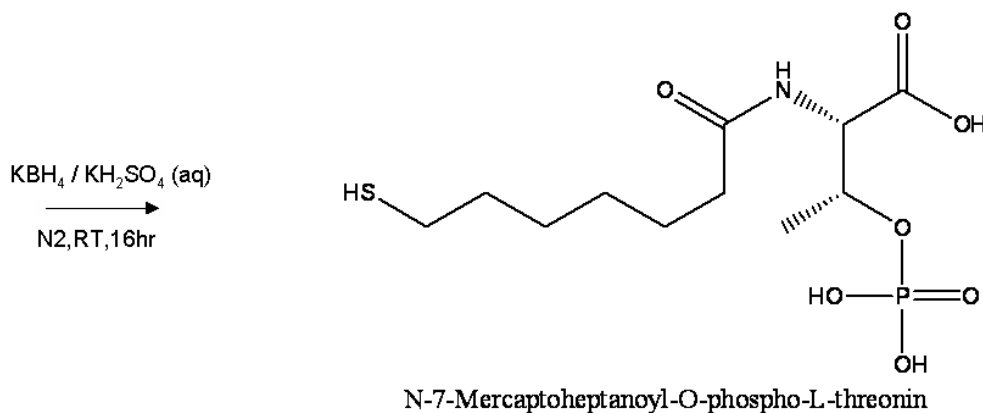
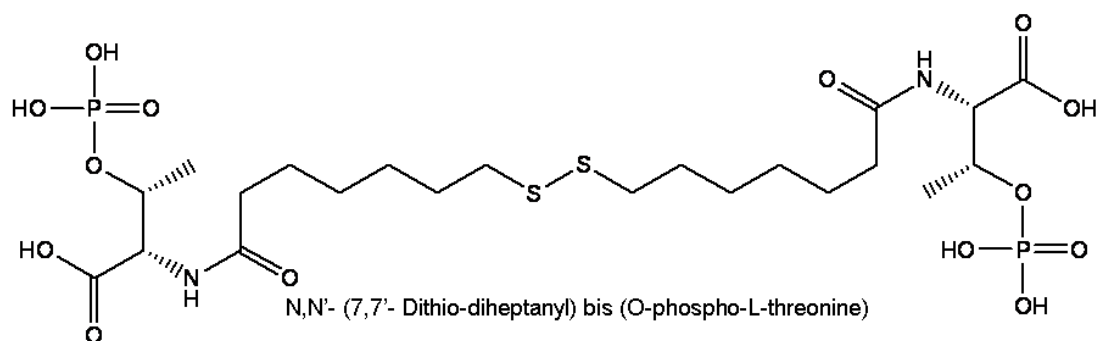
### 3.3.3 (+)-*N,N'*-(7,7'-Dithio-diheptyl) bis (*O*-phospho-L-threonine)



A solution of *O*-phospho-L-threonine (400 mg, 2 mmol) and triethylamine (0.56 ml, 4 mmol) in 4 ml water was added under stirring to a solution of 7,7'-dithiobis(succinimido-oxyheptanoate) (362 mg, 0.7 mmol l) in 18 ml tetrahydrofuran and 4 ml acetonitrile. After stirring at room temperature under nitrogen for 36 h, the solvents were removed under vacuum at 30°C. The resulting white residue was dissolved in 1 M HCl (25 ml) and washed three times with dichloromethane (3 × 8 ml). Traces of dichloromethane were removed from the aqueous phase under vacuum. The aqueous phase was applied to a 2 × 13 cm column of polystyrene XAD-2 (equilibrated with 1 M HCl). The column was washed with 100 ml of 1 M HCl, followed by 150 ml H<sub>2</sub>O. The product was eluted applying a methanol gradient (80 ml H<sub>2</sub>O/MeOH, 4:1; 120 ml

H<sub>2</sub>O/MeOH, 1:1; 80 ml H<sub>2</sub>O/MeOH, 1:4, 100 ml MeOH). TLC analysis (solvent system: n-butanol/acetic acid/H<sub>2</sub>O, 2:1:1) of the collected fractions (10 ml each) showed that HTP-S-S-HTP (R<sub>f</sub> = 0.35) had been completely separated from O-phosphothreonine (R<sub>f</sub> = 0.24) and less polar products (R<sub>f</sub> > 0.6). The combined fractions containing pure HTP-S-S-HTP were concentrated under vacuum (50°C) to 1/10 of the original volume, 2 ml 2 M ammonia was added to obtain the ammonium salt. After lyophilization 112 mg (20%) (+)-*N,N'*-(7,7'-dithiodiheptanoyl)bis(*O*-phospho-L-threonine), a white solid, was obtained. Mp is 105-106 °C.

### 3.3.4 (+)-(2*S*,3*R*)-*N*-[7-Mercaptoheptanoyl]-*O*-phospho-L-threonine



25 mg (32  $\mu\text{mol}$ ) CoB-S-S- CoB (Ammonium salt) is dissolved in 0.5 ml anaerobic 50 mM potassium phosphate buffer, pH 7.0, under a nitrogen atmosphere. Subsequently, 2 ml of an anaerobic  $\text{KBH}_4$ -solution (10% in 50 mM potassium phosphate buffer, pH 7.0) is added, and the solution is stirred for 16 h under nitrogen atmosphere at RT. Excess  $\text{KBH}_4$  is removed by addition of 0.5 ml 25% HCl (aq) and the acid solution (pH 0) is loaded on a Amberlite XAD-2 column (1 cm x 10 cm) equilibrated with anaerobic 1 M HCl (aq). The column is washed with anaerobic water and the H-S-CoB is eluted with anaerobic water/methanol (70:30; v/v). The collected H-S-CoB fractions were lyophilized, and the powder was dissolved in anaerobic 50 mM Tris/HCl buffer (pH 7,6). The pH is set to 7.0 with a 2 M NaOH solution. The H-S-CoB concentration was determined indirectly by determining the thiol concentration with Ellman's Reagent (see section 3.3.5). Generally, 17 mg (70% yield) coenzyme B was obtained.

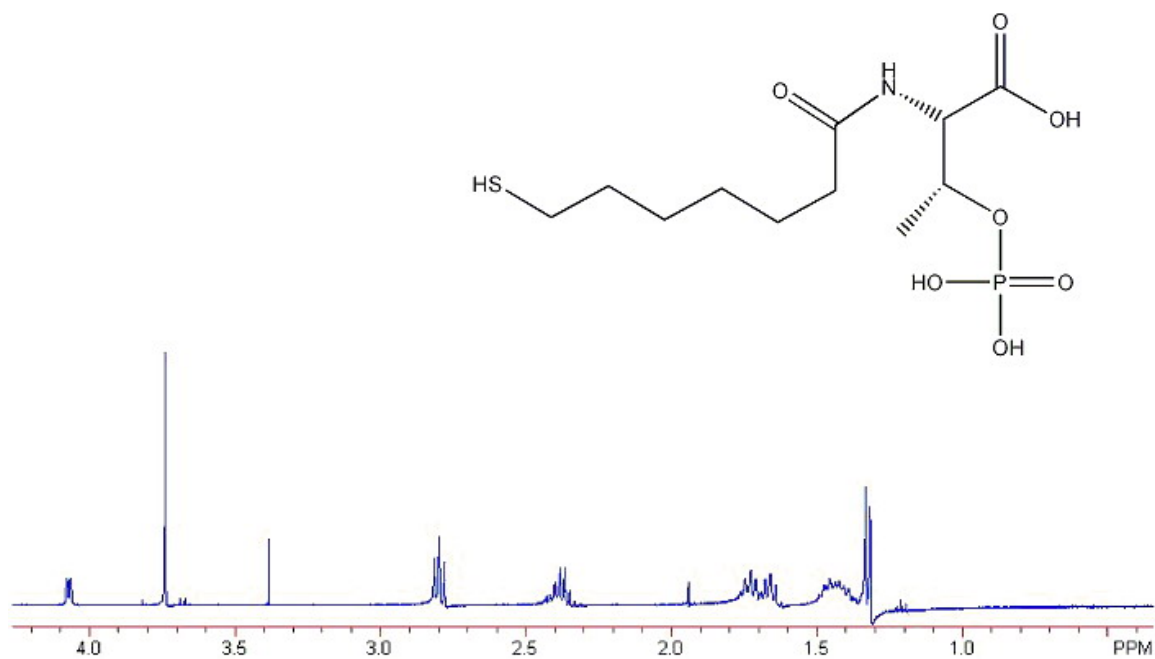
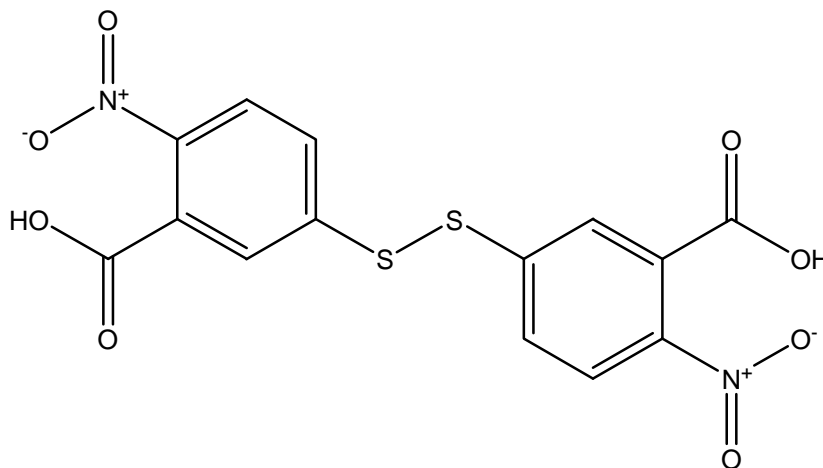


Figure 3-2: NMR spectra of coenzyme B.

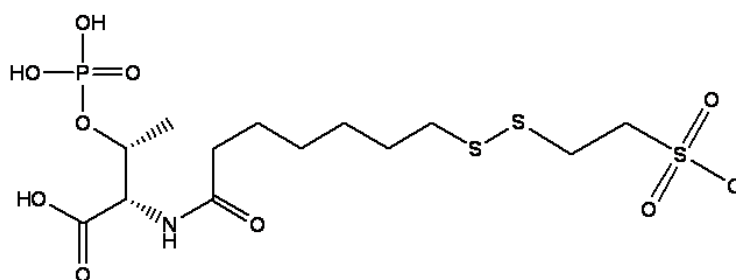
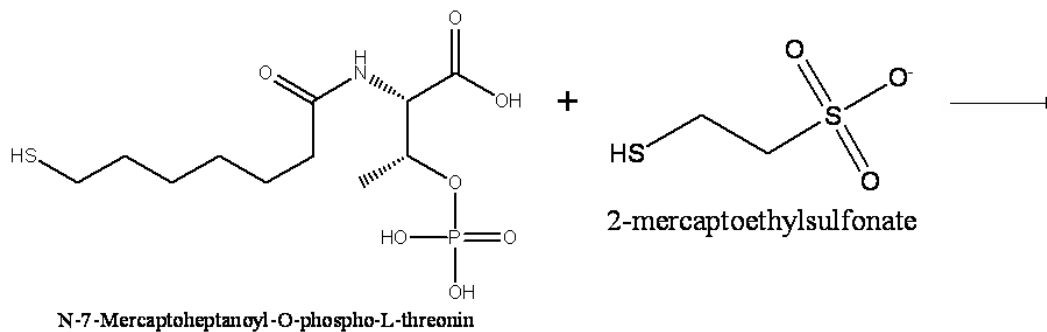
### 3.3.5 Determination of the Concentration of Coenzyme B



5,5'- dithiobis-(2-nitrobenzoic acid)

Ellman's reagent (5,5'-dithiobis-(2-nitrobenzoic acid)) or DTNB is an important reagent for quantization of thiols in proteins, cell and plasma by absorption measurement [120, 121]. It readily forms a mixed disulfide with protein thiols that are accessible to this water-soluble reagent [122-125]. In the disulfide exchange reaction one half of the DTNB molecule, 5-mercapto-2-nitrobenzoic acid, is released as a bright yellow-colored chromophore (absorption maximum 410 nm,  $\epsilon = 13,600 \text{ cm}^{-1}\text{M}^{-1}$  [125]).

### 3.4 Synthesis of CoM-S-S-CoB



100 mg (80.13  $\mu$ mol) CoB-S-S-CoB and 400 mg (2.4 mmol) CoM-SH are dissolved in 3 ml anaerobic 100 mM KPP pH 8.0. The CoB-S-S-CoB disulfide is reduced by CoM-SH and no borohydride is required for this reaction. The solution is incubated at 40 °C until the CoB-S-S-CoB is completely reduced to CoB-SH. The level of reduction is checked by HPLC. The sample is diluted to a volume of 10 ml with 10 mM KPP buffer pH 9.0. Subsequently, 0.5 mg FeSO<sub>4</sub> is added. The oxidation step takes place by exposure to atmospheric oxygen. The formation of CoM-S-S-CoB is checked by HPLC. The heterodisulfide is purified on an XAD-2 column. The CoM-S-S-CoB elutes from the XAD-2 column with 25% methanol.

### 3.5 Purification of MCR

*M. marburgensis* was grown at 65 °C in a 13 L glass fermenter (New Brunswick) containing 10 L of growth medium. The mineral-salt medium [126] contained 65 mM  $\text{KH}_2\text{PO}_4$ , 50 mM  $\text{NH}_4\text{Cl}$ , 30 mM  $\text{Na}_2\text{CO}_3$ , 0.5 mM nitrilotriacetic acid, 2 mM  $\text{MgCl}_2$ , 50  $\mu\text{M}$   $\text{FeCl}_2$ , 1  $\mu\text{M}$   $\text{CoCl}_2$ , 1  $\mu\text{M}$   $\text{Na}_2\text{MoO}_4$ , 5  $\mu\text{M}$   $\text{NiCl}_2$ , and 20  $\mu\text{M}$  resazurin. It was made anaerobic by gassing with 80%  $\text{H}_2$ /20%  $\text{CO}_2$ /0.1%  $\text{H}_2\text{S}$  at a rate of 1,200 ml/min. The resazurin was added to the medium to indicate when sufficient anaerobic conditions were reached. After 1 h of equilibration, the medium was inoculated with 150–200 ml of fresh cell culture. At a  $\Delta\text{OD}_{578}$  of  $\sim 4.5$ , the cells were harvested.

The gas phase was switched to 100%  $\text{H}_2$  for a period of 30 min before harvesting to induce the MCRred1 and MCRred2 forms in the cells (The MCRred2 signal is lost during purification due to removal of coenzyme B). The cells were cooled over a 10 min period to 10 °C under continuous gas flow and were then harvested anaerobically by centrifugation using a flow-through centrifuge (Hettich, centrifuge 17 RS). Approximately 50 g of wet cells was obtained. All the following steps were performed in an anaerobic chamber (Coy Instruments) with an atmosphere of 95%  $\text{N}_2$ /5%  $\text{H}_2$ .

After the cells were collected by centrifugation, the rotor was brought into the anaerobic tent. For the purification of the MCRred1 form, all buffers were supplemented with 10 mM coenzyme M [76]. The cell pellet was resuspended in 50 ml 10 mM Tris-HCl buffer, pH 7.6, and sonicated 3 times for 7 min each at 100% power, followed by ultra-centrifugation at 160,000 x g for 20 min at 4 °C. The supernatant was subjected to a

70% ammonium sulfate precipitation step by addition of the appropriate amount of a saturated ammonium sulfate solution. MCR stays in solution under these conditions. Precipitated protein was removed by ultra-centrifugation at 160,000 x g for 20 min at 4 °C. The supernatant was, subsequently, subjected to a 100% ammonium sulfate precipitation step by addition of the appropriate amount of solid ammonium sulfate. The 100% precipitation step separates MCR from small cofactors present in the cell extract of methanogens. After the 100% precipitation step, the pellet was resuspended in 100 ml 50 mM Tris-HCl pH 7.6 and subsequently loaded on a Q-Sepharose column. The column was developed with a step gradient using the same buffer containing 2 M NaCl. MCR eluted at about 0.52 M NaCl. This method generally yielded 150 mg MCRred1c (in 120 ml) with 0.5–0.9 spins per nickel (red1c indicates red1 state with coenzyme M present). The specific activity of the purified enzyme was 10–30 U per mg protein calculated for one spin per mol F<sub>430</sub> [76].

### **3.6 Induction of the MCRred1 forms in whole cells**

The MCRred1 form is induced in whole cells by changing the gas phase to 100% H<sub>2</sub>. The changes in the signals of the EPR-active species in whole cells were followed as a function of the incubation time to determine the required time needed to fully induce the MCRred1 form. In this experiment, aliquots of 50 ml were taken under exclusion of oxygen from a batch fermenter containing 10 L of cell suspension growing at 65°C. The 50 ml was immediately cooled to 4°C and the cells were spun down within 5 min. The

cell pellet was resuspended in 1 ml buffer and a 350  $\mu$ l sample was frozen in an EPR tube and stored in liquid nitrogen.

### **3.7 Protein Determination**

The protein concentration of MCR was determined by using the method of Bradford with bovine serum albumin (Serva) as standard [127, 128] or by measuring the absorbance difference of oxidized enzyme (MCRsilent) at 420 nm using an  $\epsilon = 44,000 \text{ M}^{-1}\text{cm}^{-1}$  for a molecular mass of 280,000 Da. Both methods yielded almost the same results.

### **3.8 Activity Assay**

MCR was assayed for methane formation from methyl-coenzyme M and coenzyme B at 60 °C as described previously [67, 129]. The standard assay mixture contained in addition to MCR, 50mM Tris-HCl Buffer, 0.5 mM Coenzyme B, 10-50nM Methyl-Coenzyme M, 15mM Ti(III) citrate, 15mM Cob(II)alamin. Samples were prepared in stoppered bottles in the anaerobic tent and kept on ice. The reaction was started by heating the vials to 60 °C (the optimal temperature for MCR activity). Each minute, a 100  $\mu$ l sample of the vials' gas space was injected into a gas chromatograph to determine the extent of methane formation. Standard solution of 0.5% and 1.0 %  $\text{CH}_4$  were used to

calibrate the gas chromatograph. Other potential gasses that could form like ethane were assayed similarly.

### **3.9 EPR Experiments**

EPR spectra at X-band (9.38 GHz) were obtained with a Bruker EMX-6/1 EPR spectrometer composed of the EMX 1/3 console, ER 041 X6 bridge with built-in ER-0410-116 microwave frequency counter, ER-070 6 inch magnet with 60 mm air gap, and ER-4119-HS, high sensitivity perpendicular-mode cavity. All spectra were recorded with a field modulation frequency of 100 kHz. Cooling of the sample was either performed with an Oxford Instruments ESR 900 cryostat with an ITC4 temperature controller or with a liquid nitrogen finger dewar at 77 K. Data acquisition was with the software supplied by Bruker (WINEPR Acquisition program, May 1, 1997, version 2.3.1.), data manipulation (determination of g-values, subtraction, base lining, integration and conversion to ASCII files for use with Origin) was done with the WINEPR program version 2.11. EPR tubes (Wilmad, 714-PQ-8) were 4 mm outer diameter (0.38 mm wall thickness) and 13.5 cm length, high purity quartz tubes. The samples were stored in the dark immersed in liquid nitrogen. To facilitate handling, the EPR probes were linked with pierced rubber tubing to polystyrene sticks with a label on it. Spin quantization were carried out under nonsaturating conditions using 10 mM copper perchlorate as the standard (10 mM  $\text{CuSO}_4$ ; 2 M  $\text{NaClO}_4$ ; 10 mM HCl). The measured signals were double integrated and the value was compared to that of the EPR signal of the standard. The programs of S.P.J. Albracht were used for computer simulations of the EPR signals [130].

### 3.10 ENDOR measurements

ENDOR studies were performed by J. Hammer, ETH Zurich. The X- and W-band (9.7 / 94 GHz) measurements were made on a Bruker E680 spectrometer, and at Q-band (34.83 GHz) on a instrument built at the ETH Zurich. Both instruments were equipped with a helium gas-flow cryostat from Oxford Inc. The W-band echo-detected EPR spectra were recorded by integrating the echo intensity created with the mw pulse sequence  $\pi/2$ - $\tau$ - $\pi$ - $\tau$ -*echo* with mw pulse lengths  $t_{\pi/2} = 100$  ns,  $t_{\pi} = 200$  ns, and a  $\tau = 500$ -700 ns. The first derivative of this spectrum was calculated numerically. The field was calibrated using the two central lines from a CaO sample containing manganese ions.

### 3.11 UV-visible spectroscopy

UV-vis spectra were recorded on a HP-8453 or HP-8452 diode-array spectrophotometer equipped with 1 cm cells and a Brinkman Lauda RM6 thermostated water bath to maintain the temperature at  $25.0 \pm 0.1$  °C. A concentration of approximately 20  $\mu$ M MCRred1 was used in the experiments.

### 3.12 X-ray absorption spectroscopy

X-ray absorption spectroscopy was used to check oxidation state and coordination of Ni in MCR-analog complexes. The group of Dr. Robert Scott at the University of

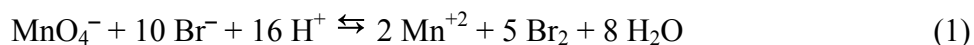
Georgia, Athens, GA, performed the X-ray absorption spectroscopy measurements. MCRred1c was prepared as described in section 3.5. The protein was concentrated to 0.5-1.5 mM, which equals 1.0-3.0 mM for nickel (checked by EPR and absorption spectroscopy). Actual nickel concentrations and spin intensities are listed in Table 3-1. For MCR-BES, the amount of this form present was derived from the initial amount of MCRred1 present in the sample. All samples contained 10 mM coenzyme M and 30% ethylene glycol. MCR-BPS samples contain 30 mM BPS. MCR-BES samples contain 5 mM coenzyme B and 30 mM BES. MCR-BrMe samples contain 25 mM BrMe.

Table 3-1: XAS samples

Sample	Concentration of Ni (mM)	Spin Intensit y	Other forms present
BPS I	0.56	0.34	
BPS II	1.0	0.67	MCRox1 (0.05)
BPS III	1.0	0.86	
BES I	1.6	0.67	MCRox1 (0.05)
BES II - washed	2.2	0.80	MCRox1 (0.05) - MCRred1 (0.05)
BES III	1.0	0.86	
BrMe	0.5	0.86	
BrMe	0.2	0.86	
BrMe	0.8	0.86	MCRox1 (0.04)

### 3.13 Assays for Bromide

The treatment of MCR in the red1 form with BrMe, BPS, and possibly also BES is expected to result in the formation of Br<sup>-</sup>. To detect and quantify the formed bromide a colorimetric assay was used based on the reduction of the permanganate ion:



Since coenzyme M also reacts with the permanganate ion, it is important to wash the protein extensively using the Amicon ultrafiltration units. Protein was washed 4x times with buffer that does not contain coenzyme M. Subsequently the protein was treated with BPS, BES and BrMe. The protein was concentrated using the ultrafiltration units (30 kDa cut off) and the filtrate was tested for the presence of bromide. The theoretical amount of bromide formed for each type of protein sample could be calculated by comparison of the signal intensities of the original MCRred1 signal and the formed MCR-BPS, MCR-BrMe species. In the case of BES the remaining MCRred1 signal was used.

### 3.14 Anaerobic saturated BrCH<sub>3</sub> solution

Anaerobic saturated BrCH<sub>3</sub> solution where made by placing 5 ml anaerobic buffer in a 50 ml bottle inside the anaerobic tent. The bottle was sealed and the gas phase replaced by BrCH<sub>3</sub>. The solubility of bromomethane in water is 15.2 g/l (161mM) at room temperature. [131].

## CHAPTER FOUR

### RESULTS

#### 4.1 Purification of MCR

*M. marburgensis* was grown at an optimal temperature of 65 °C in a 13 L glass fermenter containing 10 L medium. A complete growth curve is shown in Figure 4-1. Cells were generally harvested at a  $\Delta OD_{578}$  of  $\sim 4.5$ . To obtain MCR in the MCRred1 state, the gas phase was changed to 100% H<sub>2</sub> 30 min before harvesting. The cell culture was cooled down to  $\sim 10$  °C. The cells were harvested anaerobically using a flow-through centrifuge. The purification procedure was performed in the anaerobic chamber. Cell extract was subjected to fractionation by subsequent 70% and 100% ammonium sulfate precipitation steps. After resuspension of the precipitated MCR in low salt buffer, anion-exchange chromatography was performed on a Q-sepharose column, using a step gradient. Fractions were pooled together and concentrated using an Amicon concentration device with a 30 kDa cut-off filter (Millipore) to an enzyme concentration of  $\sim 200$   $\mu$ M. The purity of MCRsilent was judged by SDS-PAGE (Figure 4-2). The gel shows the increase in purity during the different steps of the purification procedure. Purified MCR shows three clear bands, implicating the presence of three subunits:  $\alpha$ ,  $\beta$ , and  $\gamma$ . By judging from SDS-PAGE, the purity of MCR was  $> 90\%$ .

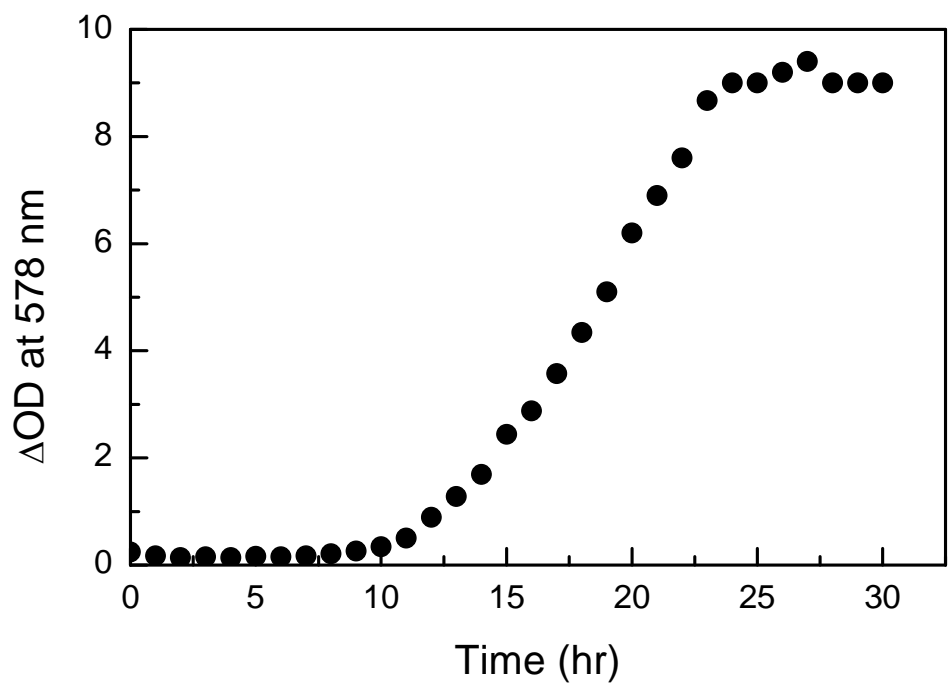


Figure 4-1: Growth curve of *Methanothermobacter marburgensis* grown in 10 L medium at 65°C.

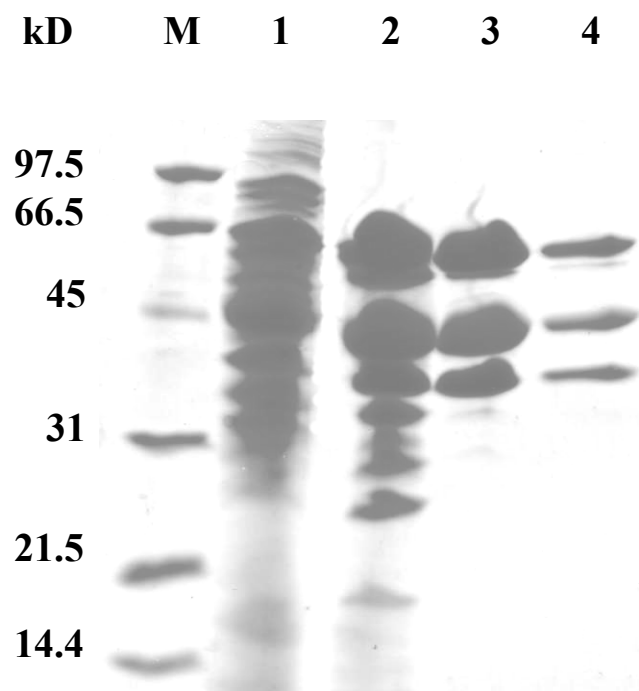


Figure 4-2: SDS-PAGE of MCR in different stages of the purification. Lane M: Molecular weight marker; Lane 1: Cell lysate; Lane 2: Sample from 100% ammonium sulfate precipitation; Lane 3: Sample after Q-sepharose column; Lane 4: Sample from Amicon Centrifugal Filter (30 kD cut-off).

#### 4.1.1 Induction of the MCRred1 Form

To be able to study the MCR enzyme, one must obtain either the stable inactive MCRox1 form which can be converted into the active MCRred1 form [85] or to obtain the MCRred1 form directly. The MCRred1 form can be induced in growing cells by changing the gas phase before the cells are harvested. By changing the gas phase to 100% H<sub>2</sub> a more reducing environment is created in the cells. Figure 4-3 shows the effects of this procedure on the EPR signals detected in whole cells of *M. marburgensis*. The top spectrum (0 min) is taken before the gas phase is changed from 80% H<sub>2</sub>/20% CO<sub>2</sub> to 100% H<sub>2</sub>. Under the regular growth conditions most of the MCR seems to be present in the red1 form. A small amount of the ox1 form is also detectable. Within 5 min of gassing with H<sub>2</sub> it can be detected that the ox1 form is gone, the red1 form has increased in intensity and even the red2 form is already present. After 15-20 min of incubation the spectral changes in the cells seem to have come to a completion. Generally, cells will be harvested after a 20-30 min incubation period. It is important, however, that the temperature is lowered below 20°C. Below this temperature all enzyme activity in the cells will stop, preventing changes in the reduction state of the enzymes in the cell extract after the cells are broken inside the clove box. The 5% H<sub>2</sub> concentration in the box would otherwise cause oxidation of the hydrogenase enzymes that in turn would cause the oxidation of enzymes in the hydrogenotrophic pathway.

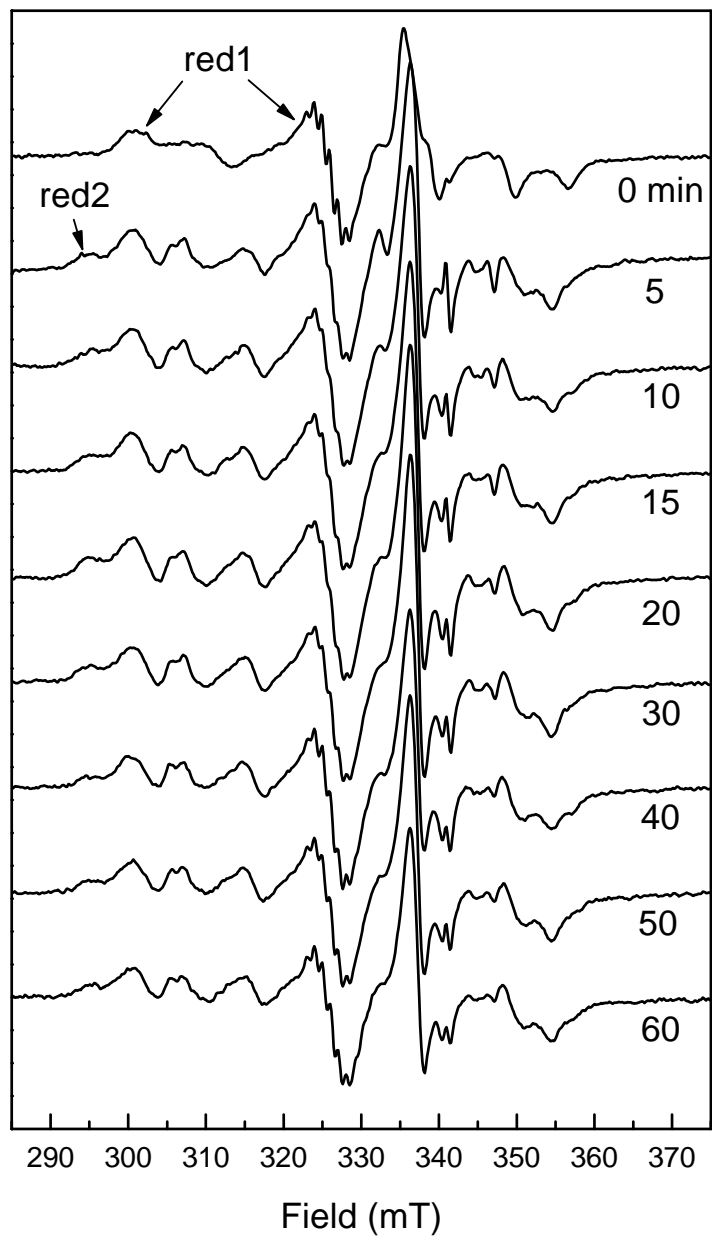


Figure 4-3: Time dependency of the induction of the MCRred1 and MCRred2 forms by changing the gas phase to 100% hydrogen gas.

*In vitro* the MCRred2 signal can be induced by adding coenzyme M and coenzyme B to MCR in the MCRred1 form. From this finding it can be explained what is happening in whole cells. The hydrogenase/heterodisulfide reductase complex in the cells must be using the H<sub>2</sub> to split the heterodisulfide into coenzyme M and coenzyme B. Apparently; these coenzymes are produced in high enough amounts to induce the MCRred2 signal. The MCRred2 form is lost during purification (due to the loss of coenzyme B and is converted into MCRred1) and the final purified enzyme normally has 70 to 90% in a red1 form [76, 84].

#### **4.1.2 Activity Assay**

The purified enzymes catalyzed the reduction of methyl-coenzyme M with coenzyme B to CH<sub>4</sub> and CoM-S-S-CoB at a specific rate of 78 nmol·min<sup>-1</sup>·mg protein<sup>-1</sup> when the assay mixture contained CH<sub>3</sub>-S-CoM, H-S-HTP, Ti(III) Citrate, Cob(II)alamin and enzyme (Fig. 4-4). This figure was made, however, with the enzyme that displayed a much lower activity.

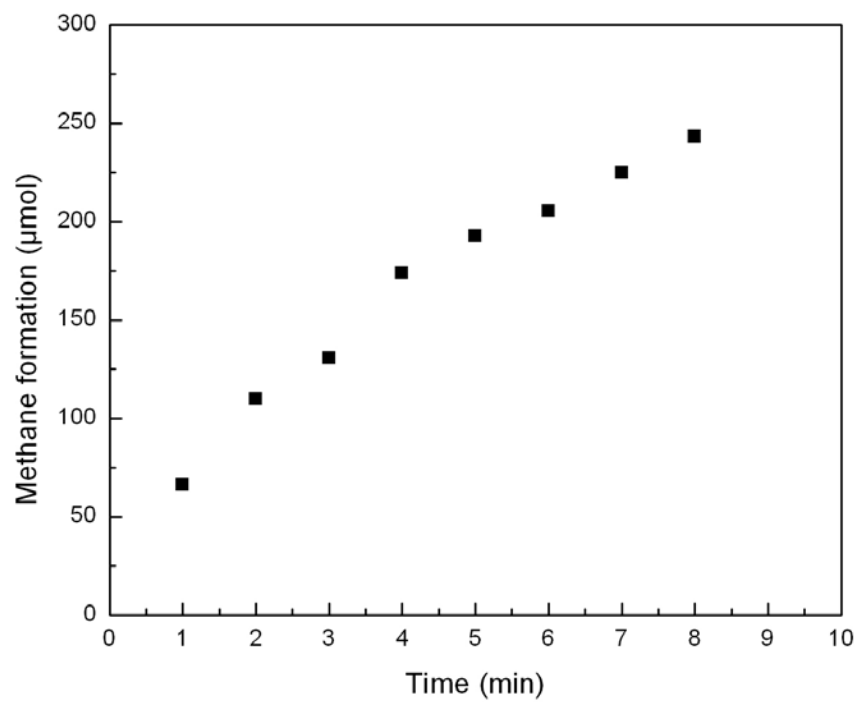


Figure 4-4: Activity assay of MCRred1. The 2 ml assay mixture contains: 50mM Tris-HCl Buffer, 0.5mM CoB, 10-50nM Methyl-CoM, 15 mM Ti(III) Citrate, 15 mM Cob(II)alamin and MCRred1 (31mg)

## 4.2 Observations on MCR Made under Turnover Conditions

The activity of MCR can be measured under different conditions. The current method where both Ti(III) citrate and cobalamin are added to the assay, has the advantage that the heterodisulfide that is formed during the reaction is immediately converted back into coenzyme M and coenzyme B. This is important since heterodisulfide is an inhibitor of MCR [58]. Removal of the inhibition allows the collection of data points over a longer time interval. Since the inhibition by heterodisulfide becomes a problem at relative high concentrations (see also Figure 4-6), kinetic parameters can in principle be obtained with only the two substrates present as long as enough points can be collected within a very short time range.

The proposed reaction mechanisms for MCR include several EPR-active species that appear and/or disappear during the reaction. Therefore the enzyme has been studied with the rapid-mix rapid-freeze technique. Surprisingly, the only signal that is detectable in these studies is the MCRred1 signal (Stephen Ragsdale, personal communication). Even at the shortest time intervals measured (~30 ms) no change is detected in the EPR signal or its intensity. From this it can be concluded that the first step in the reaction is probably the rate-limiting step. This limits the amount of kinetics studies that can be done considerably. As a result research efforts have been concentrated at finding substrate homologs that change the dynamics of the reaction mechanism and suicide inhibitors that allow trapping of paramagnetic inhibited forms. Some of these studies will be presented below.

In addition, MCR has been studied under steady state conditions. In Figure 4-5, panel A, a series of EPR spectra is shown that were taken at different time intervals when MCR (0.250 mM) is incubated at 65 °C with 25 mM methyl-coenzyme M and 25 mM coenzyme B. Methane formation was detectable as the formation of gas bubbles in the enzyme solution. Interestingly, the intensity of the active MCRred1 form is decreasing over time. At the same time, the appearance of the MCROx1 form is detected. Double integration of the areas underneath the signals show that the intensity of the MCROx1 signal after 30 min of incubation is about 50% of that of the original MCRred1 signal. Since the original MCR signal represented about 0.85 spin, it has to be concluded that the MCRred1 forms has been converted into 50% MCROx1 and 50% MCRsilent during the 30 min experiment. Figure 4-5, panel B, shows the formation of a radical species that reaches maximal intensity at around 15 min. The origin of this species is unknown.

As shown in Figure 1-8, MCRred2 can be converted into MCROx1 by addition of polysulfide. Since heterodisulfide is formed during the reaction it can be proposed that during the reaction small amounts of the MCRred2 form are present, that are converted into the MCROx1 form by the heterodisulfide. To investigate this, the effects of heterodisulfide on both the MCRred1 and the MCRred2 forms have been studied.

Figure 4-6, shows that increasing heterodisulfide concentrations lead to the quenching of the red1 signal. The same is observed for the red2 signal

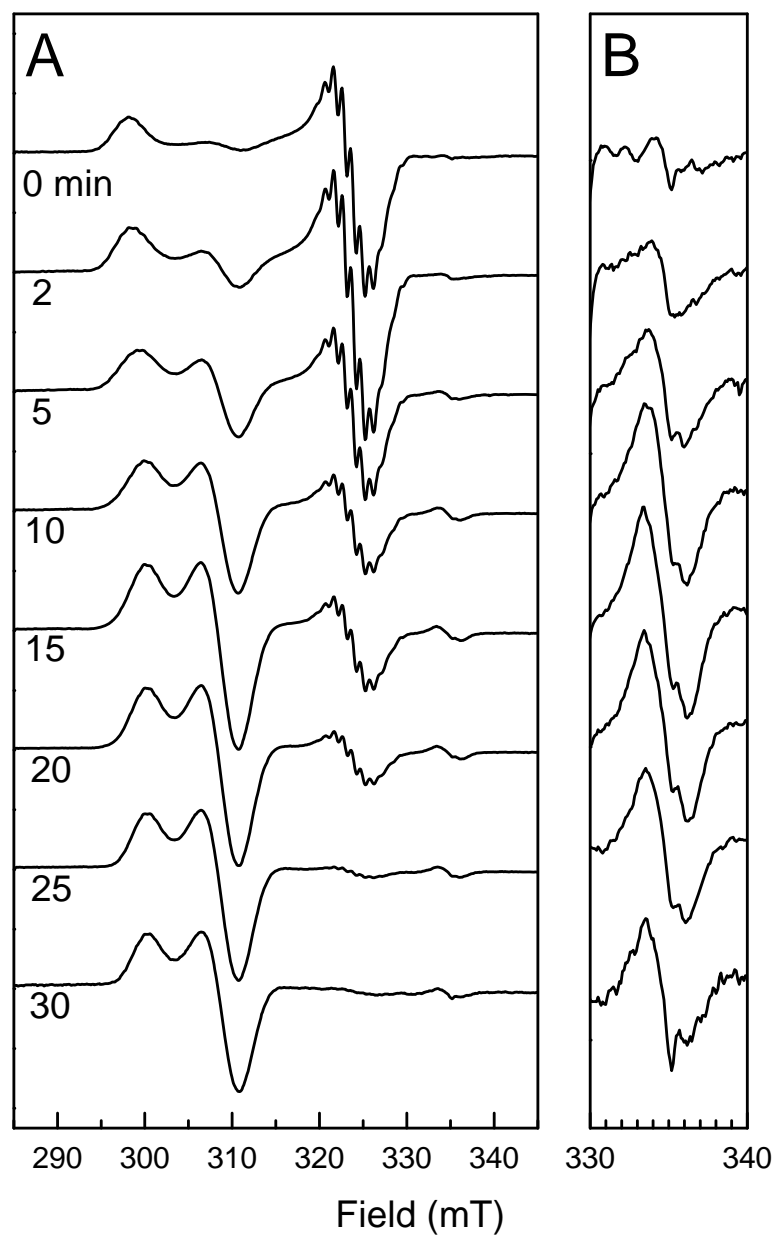


Figure 4-5: Change in EPR spectra detected for MCR under turn-over conditions. MCR (0.250 mM) was incubated at 65°C in the presence of 25 mM methyl-coenzyme M and 25 mM coenzyme B.

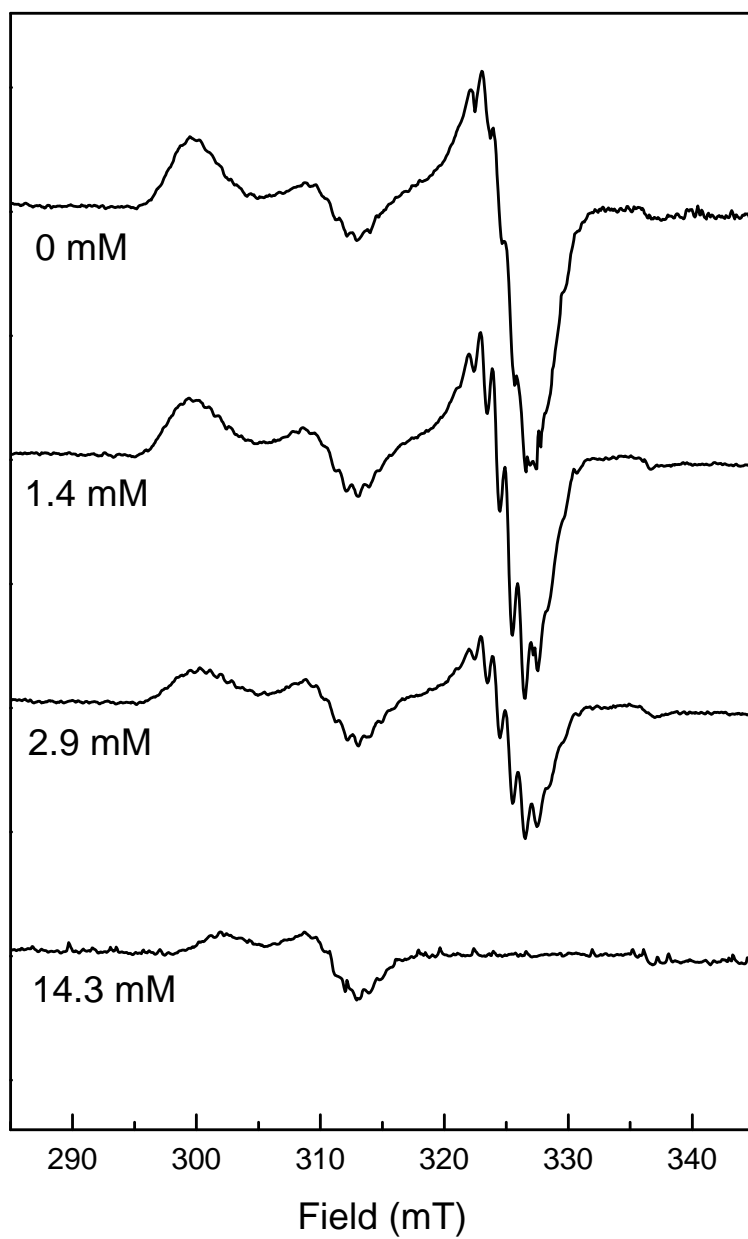


Figure 4-6: Effect of different concentration of heterodisulfide (CoM-S-S-CoB) on the MCRred1 form.

### 4.3 Using labeling studies to detect the positions of selected atoms of substrates and analogs that are bound in the active site of MCR

Figure 4-7 shows an overview of the EPR signals of different forms of MCR measured at W-band (94 GHz). At higher frequency the different peaks in the EPR spectra are placed further apart from each other. Although the actual line width of the signals does not change, to the eye it looks like the lines are much sharper and small differences in  $g$  values now become detectable. Spectrum **1** is the EPR signal for the MCRred1a form. In this case the signal is almost completely axial (the small shoulders are due to a small amount of MCRred1c). The addition of coenzyme M results in the formation of the MCRred1c form (Fig. 4-7, spectrum **2**), which shows a bit more anisotropy. The addition of coenzyme M and coenzyme B results in the formation of the two red2 forms, indicated in the figure with ‘▲’ for the MCRred2-rhombic form and ‘△’ for the MCRred2-axial form (Fig. 4-7, spectrum **8**). The red2 form is also detected when trifluoromethyl-coenzyme B (CF<sub>3</sub>-S-CoB) is used instead of methyl-coenzyme B (Fig. 4-7, spectrum **3**). ENDOR measurements showed that in this case the F atoms ( $I = \frac{1}{2}$ ) come within 3.5 Å of the nickel of F<sub>430</sub> [132]. This means that the thiol sulfur of coenzyme B should be able to come almost 2 Å closer to the nickel than was believed possible based on the crystal structure.

To first summarize what we know: (i) the combination of coenzyme M with either coenzyme B, methyl-coenzyme B, or trifluoromethyl-coenzyme B induces the two red2 states, red2-axial and red2-rhombic. In the red2-rhombic state the coenzyme M is bound to the nickel via its thiol sulfur. In the red2-axial state a strong coupled H atom is detected

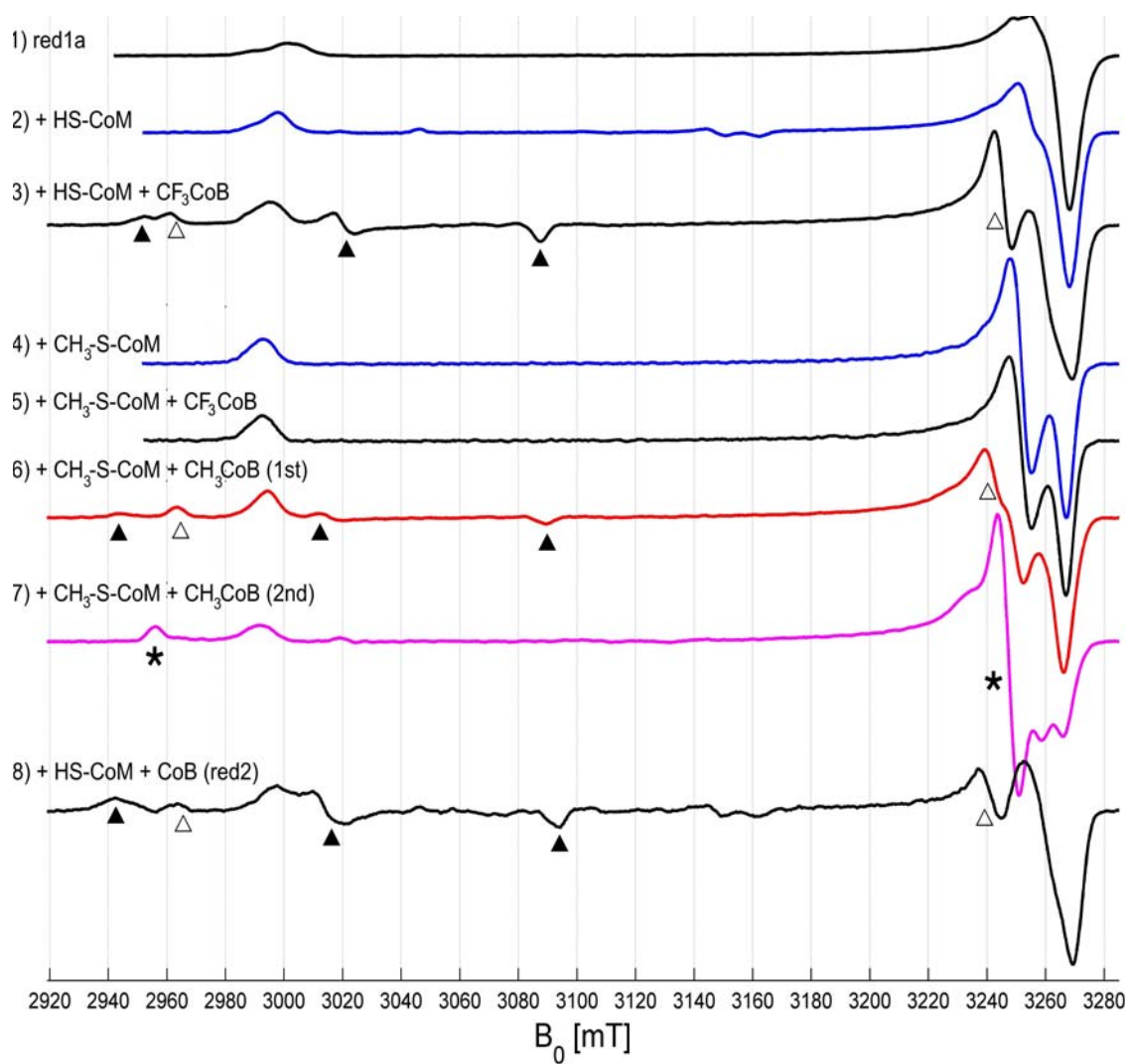


Figure 4-7: Overview of the EPR signals of the different MCR forms measured at W-band. The peak positions for different signal are indicated with symbols: MCRred2axial ( $\triangle$ ), MCRred2rhombic ( $\blacktriangle$ ), a new red1 signal ( $\star$ ). See text for details. Figure prepared by Dr. Jeffrey Harmer.

that is assigned to a Ni-H species (Jeffrey Harmer, personal communication) (ii) In the MCRred1m state, the thioether sulfur of methyl-coenzyme M approaches the nickel to a distance of 3.08 Å. (iii) No changes can be detected when both methyl-coenzyme M and coenzyme B are added to the MCRred1 form, at least not the first couple of minutes. The question was what would happen if both methyl-coenzyme M and methyl-coenzyme B were added, since the last compound is not a substrate of MCR. Would this result in the formation of the Ni-CH<sub>3</sub> species? The first set of samples for this experiment, were made by Dr. Duin's student in Germany, Meike Goenrich. With these samples the strange result was obtained that the combination of trifluoromethyl-coenzyme B with methyl-coenzyme M did not result in a change in EPR signal (Fig. 4-7, spectrum 5), while the combination of methyl-coenzyme B and methyl-coenzyme M resulted in the formation of low amounts of the MCRred2 species (Fig. 4-7, spectrum 6). Since this difference is very difficult to explain we repeated this experiment, taking extra care that the MCRred1 sample was extensively washed to remove all coenzyme M. The presence of small amounts of coenzyme M could explain why some MCRred2-axial/rhombic was formed.

Three samples were prepared for ENDOR experiments (three samples each for X-, Q- and W-band): MCRred1 with (i) HS-C-C-SO<sub>3</sub><sup>-</sup> (= coenzyme M) and methyl-coenzyme B, (ii) D<sub>3</sub>C-S-C-C-SO<sub>3</sub><sup>-</sup> and methyl-coenzyme B, and (iii) H<sub>3</sub><sup>13</sup>C-S-C-C-SO<sub>3</sub><sup>-</sup> and methyl-coenzyme B. To remove unlabeled coenzyme M, but to prevent loss of the MCRred1 form, the proteins samples were extensively washed with buffer containing 10 mM of the respective labeled coenzyme M.

Figure 4-8, shows the EPR signal of these and other samples measured at X-band (9 GHz). Figure 4-8, spectrum **1** is the MCRred1m form that is induced when methyl-coenzyme M is added to MCRred1a. Spectrum **2**, shows the EPR spectrum of MCR in the presence of both substrates methyl-coenzyme M and coenzyme B. Spectra **3** and **4** shows the spectra when methyl-coenzyme B is used instead of coenzyme B. Spectrum **3** is with  $^{13}\text{CH}_3\text{-S-CoM}$  and spectrum **4** is with  $\text{CD}_3\text{-S-CoM}$ . At the low field side of the  $g_z$  peak of the red1 signal a shoulder can be detected in both samples. Spectrum **5** shows the spectrum of MCR with methyl-coenzyme M and trifluoro-coenzyme B. This spectrum is identical to that of spectra **1** and **2**.

Similar spectra are shown in Figure 4-7, spectrum **4** is from MCRred1m. Spectrum **5** is the same sample but now with trifluoromethyl-coenzyme B present. These two spectra are identical. Figure 4-7, spectra **6** and **7**, shows the red1m form with methyl-coenzyme B present. Spectrum **6** is the old sample and clearly shows the presence of the red2 forms. Spectrum **7** is the new sample and does not show any red2 signals. The EPR signal that is detectable (indicated by ‘★’), however, does not resemble any of the MCRred1 forms. It does have some resemblance to MCRred2-axial, but 2D-ENDOR studies do not show the presence of the strongly coupled proton/hydride (Jeffrey Harmer, personal communication). This would make this a new red1-type signal.

Studies are under way to further characterize this species. In particular we hope to detect any coupling of the nickel-based free electron with either the  $^{13}\text{C}$  atom or the H/D atoms of the methyl group of methyl-coenzyme M.

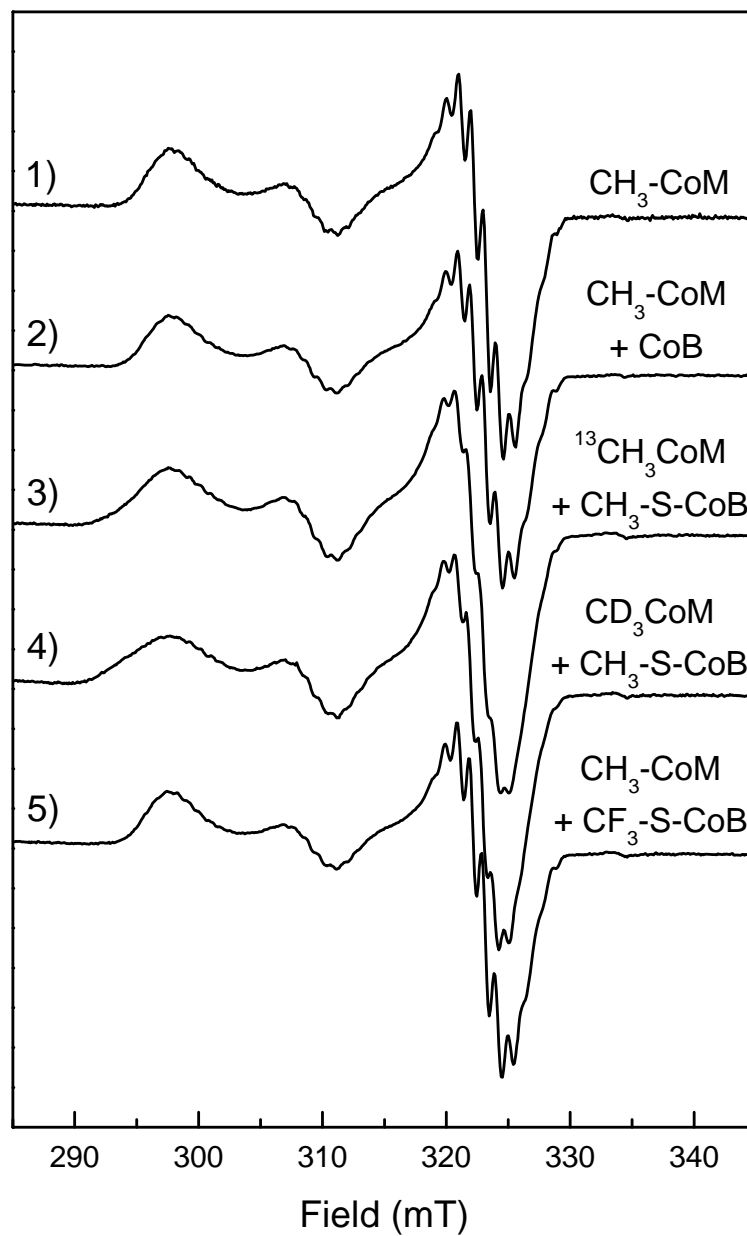
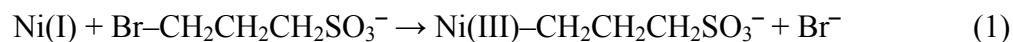


Figure 4-8. Effect of substrate analogs of MCRred1 (0.45 mM). Methyl- coenzyme M, 2.5 mM; coenzyme B, methyl-coenzyme B or trifluoromethyl-coenzyme B, 2.5 mM

#### 4.4 Studies with Bromo-alkyl Compounds

3-Bromopropane sulfonate (BPS) with an  $I_{50}$  of 50 nM is the most powerful inhibitor known for MCR. Figure 4-9 shows the effect of this compound on MCR. When sufficient BPS is added to MCR in the active red1 form, the complete red1 EPR signal disappears and a new signal, designated MCR-BPS appears. Extensive EPR and ENDOR studies [94] showed that in this state the nickel has the +3 oxidation state and has a C-atom as its sixth ligand, the C-3 carbon from BPS. The reaction that takes place was proposed to be:



This was the first indication that a Ni-C bond could be formed in MCR. Below we describe the studies of two similar compounds, 2-bromoethanesulfonate (BES) and bromomethane (BrMe). BrMe induces a similar EPR signal in MCR (Fig. 4-9) as BPS. BES on the other hand quenches the red1 signal and can under some conditions induce a small radical species (Fig. 4-9)

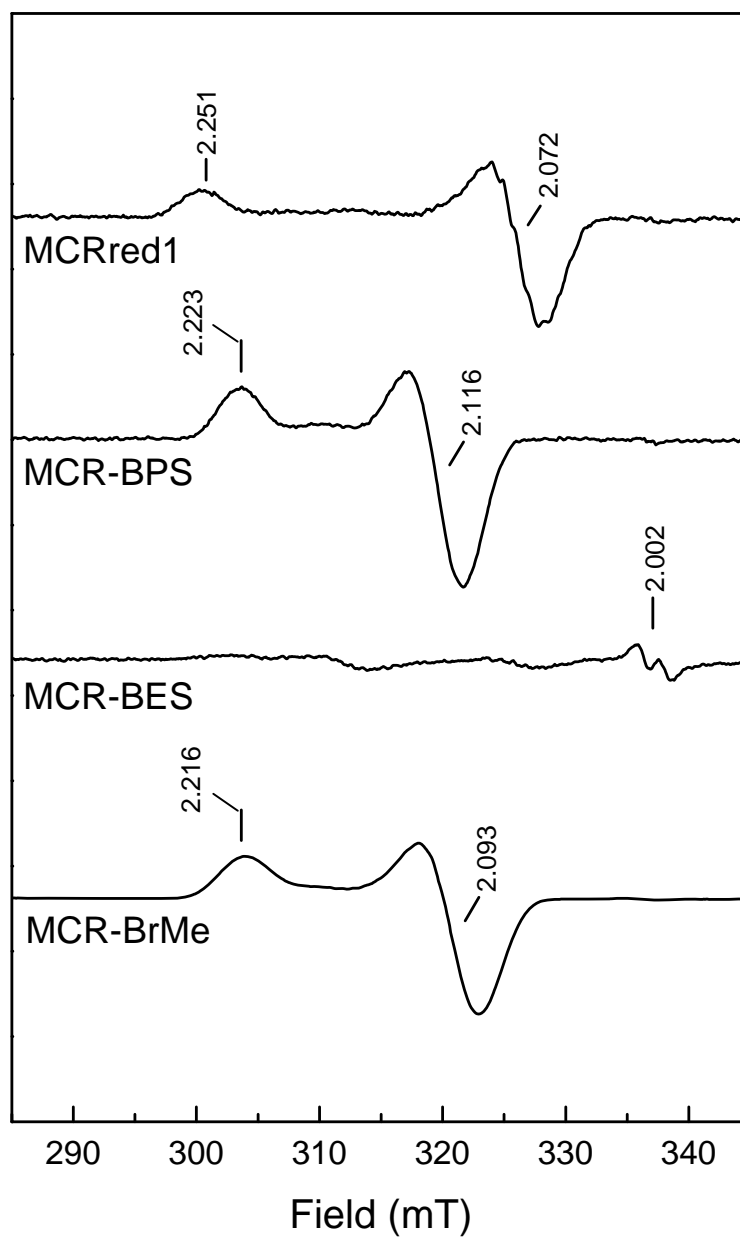


Figure 4-9: Effect of 3-bromopronesulfonate (BPS), 2-bromoethanesulfonate (BES), and bromomethane (BrMe) on MCR in the active MCRred1 form.

#### 4.4.1 EPR Studies with Bromomethane (BrMe)

The work described here has been done together with Dr. Na Yang. To obtain the  $I_{50}$  for BrMe, the conversion of the MCRred1 signal into the MCR-BrMe signal as a function of the BrMe concentration was studied by titrating MCR in the MCRred1 form with increasing amounts of BrMe (added as a saturated solution in 50 mM Tris-HCl, pH 7.6). For each BrMe concentration an EPR sample was prepared by freezing the enzyme solution in an EPR tube in liquid nitrogen after 1 min of incubation time. Figure 4-10 shows the results of the titration. With increasing concentration of BrMe more MCRred1 was converted into a new EPR signal, MCR-BrMe. Figure 4-11 shows the increase of the signal intensity of the MCR-BrMe EPR signal as a function of the BrMe concentration. A 50% conversion from MCRred1 to MCR<sub>BrMe</sub> was achieved at a concentration of 8 mM BrMe.

Just as with BPS, this work was followed up with  $^{13}\text{C}$ -labelling studies that showed that a nickel-methyl species was formed in MCR [133]:



The ENDOR studies, performed by Dr. Jeffrey Harmer, have already been described in detail in the Dissertation of Dr. Na Yang and will not be discussed here.

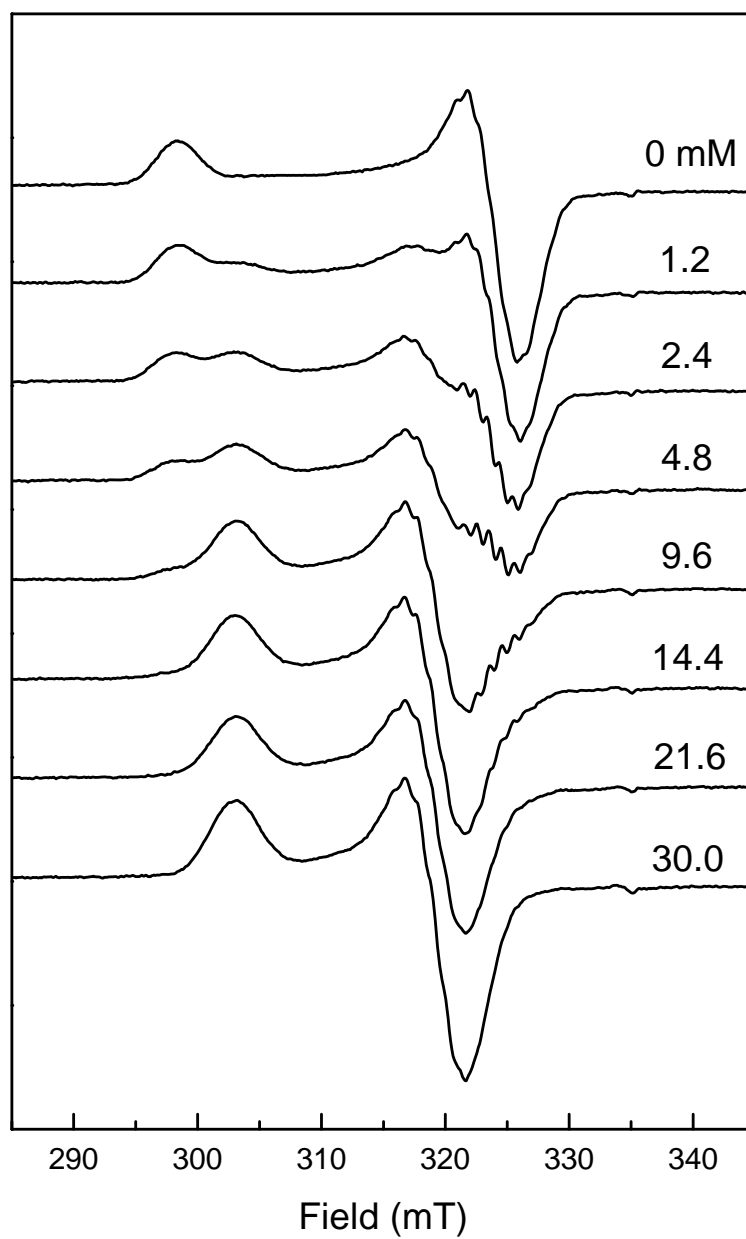


Figure 4-10: EPR spectra following the BrMe dependent conversion of MCRred1 into MCR-BrMe

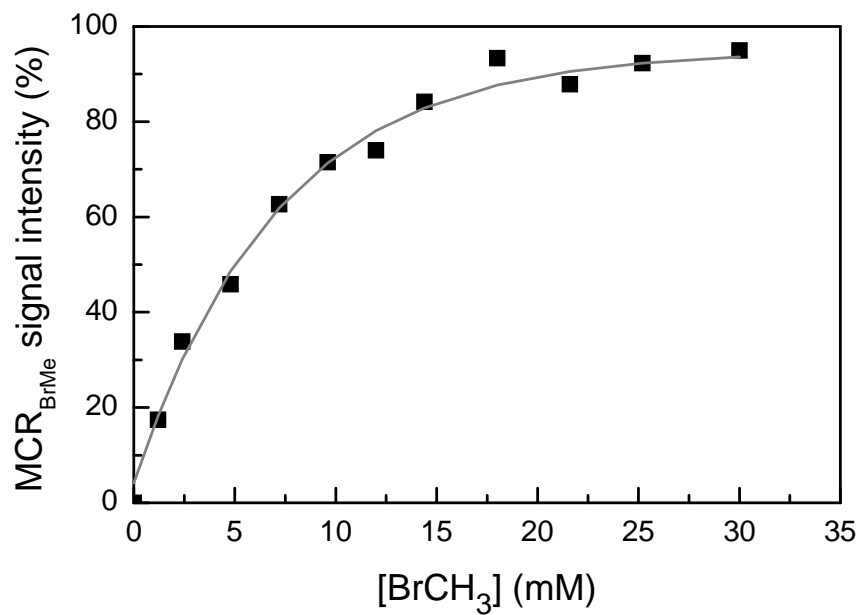


Figure 4-11: Titration curve showing the increase of the intensity of the MCR-BrMe EPR signal as a function of the BrMe concentration

#### 4.4.2 Stability of the MCR-BrMe Form

The addition of BrMe to MCR in the red1 form leads to the formation of the MCR-BrMe form. This form is relatively unstable and has a half-life of ~30 min at pH 7.6 (Figure 4-12). There are several possible causes that can explain this instability. The first possibility is that a proton reacts with the Ni(III)-CH<sub>3</sub> species forming Ni(II) and CH<sub>4</sub>. The second possibility is that due to the high BrMe concentration the Ni(III)-CH<sub>3</sub> species might react with a second BrMe molecule resulting in the formation of ethane.

To test the first possibility, it was investigated whether the signal stability was affected by the pH. The signal, however, showed the same half-life at pH 6.0, 7.0, 8.0 and 9.0 (data not shown). When the experiments were performed in stoppered bottles, examination of samples of the gas phase using a gas chromatograph did not indicate the formation of ethane.

To test if the excess BrMe would react with the nickel-methyl species, excess BrMe was removed by addition of KCN. No change in stability was observed (data not shown).

In an experiment where the enzyme sample was treated with BrMe and subsequently concentrated using an Amicon Centrifugal Filter device with a 30 kDa cut-off, it was found that the filtrate showed a yellow color. Examination with Absorption spectroscopy showed the presence of a clear band at 430 nm (not shown). The band is due to free F<sub>430</sub>. No precipitate was formed after the addition of nitric acid, indicative for the absence of protein.

In parallel experiments (see section 4.6) it was shown that F<sub>430</sub> is not released when MCR is treated with BPS or BES. This result indicates that the excess of BrMe present in the sample must slowly methylate amino acid residues in MCR resulting in a partial unfolding of MCR and release of the cofactor. Further evidence for this comes from the observation that in some cases precipitation of protein takes place immediately after addition of BrMe. This effect is mainly observed when coenzyme M is removed from the enzyme samples. Coenzyme M is removed in some cases since it will react with BrMe and form methyl-coenzyme M. In the absence of 10 mM coenzyme M in the buffer much less BrMe is needed for a full conversion of the MCR<sub>red1</sub> form. Note that the back reaction of the methyl group in MCR-BrMe with coenzyme M is much faster at high pH (> 9.0) and slow at lower pH (pH 7.0).

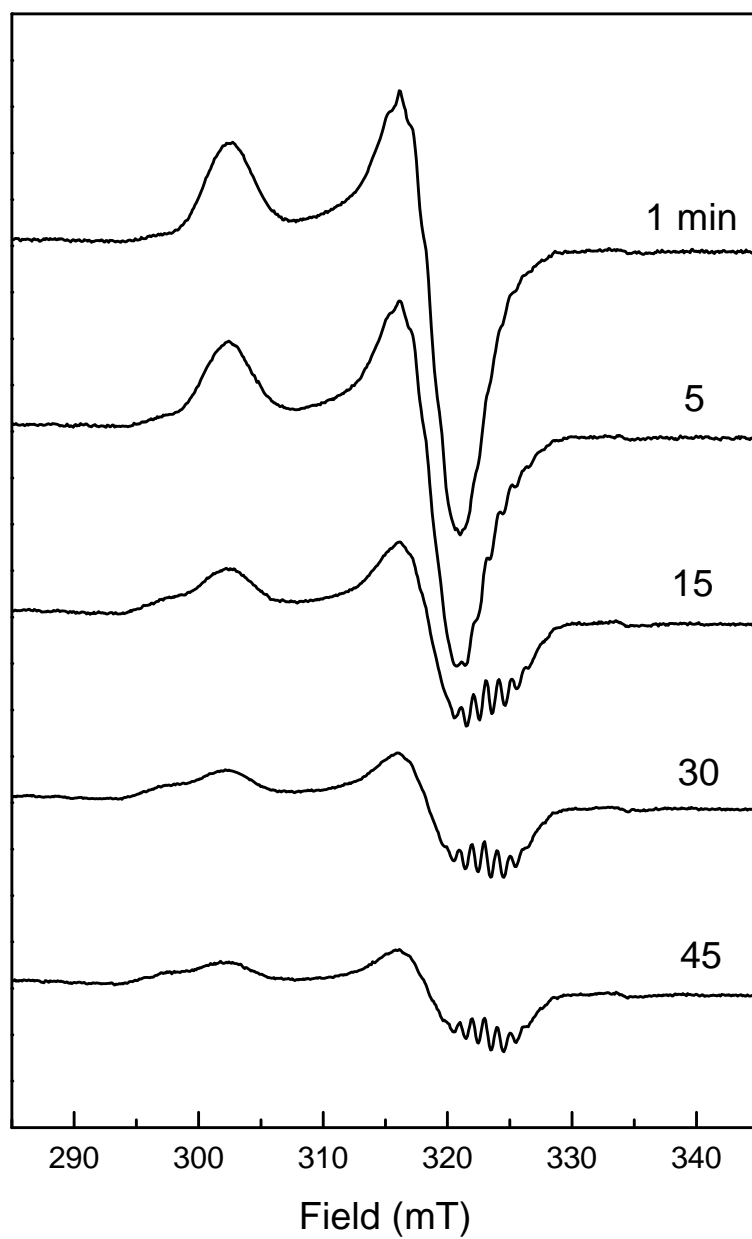


Figure 4-12: Decrease of the signal intensity of the MCR-BrMe EPR signal. Aliquots were taken from the enzyme solution 1, 5, 15, 30, and 45 min after the BrMe was added, and immediately frozen and stored in liquid nitrogen.

#### 4.4.3 Reactivity of the MCR-BrMe form

The results shown above demonstrate the formation of a nickel-methyl species in the MCR active site. Ni(I) of MCRred1 conducts a nucleophilic attack on BrMe to form MCR-BrMe and releases bromide. It adds plausibility to proposed mechanism models that proceed via such catalytic intermediates with the natural substrates. Since Ni(III) species are highly oxidative, species like  $\text{CH}_3\text{-Ni(III) F}_{430}$  may be crucial for the reverse reaction of MCR, the anaerobic oxidation of methane. It is expected that MCR-BrMe could react with HS-CoM or even heterodisulfide to convert MCR-BrMe back to MCRred1 and form  $\text{CH}_3\text{-S-CoM}$ . In the following experiment the effect of coenzyme M on the EPR signal of MCR-BrMe was studied (Fig. 4-13). MCRred1 was first washed extensively with 10 mM Taps pH 10.0 by ultrafiltration with Amicon Ultra Centrifugal Filter Units with a 100 kDa cut-off to make sure that all coenzyme M is removed. The MCR-BrMe signal was induced by addition of 50 mM BrMe. The MCRred1 EPR signal reappeared in part after addition of 20 mM HS-CoM. At least 50% conversion occurred. The remaining MCR-BrMe probably decayed into a MCRsilent form (Figure 4-13). NMR measurement by Dr. Na Yang and mass spectrometry measurements by Ragsdale and coworkers, showed that the formation of the red1 form coincides with the formation of methyl-coenzyme M [134].

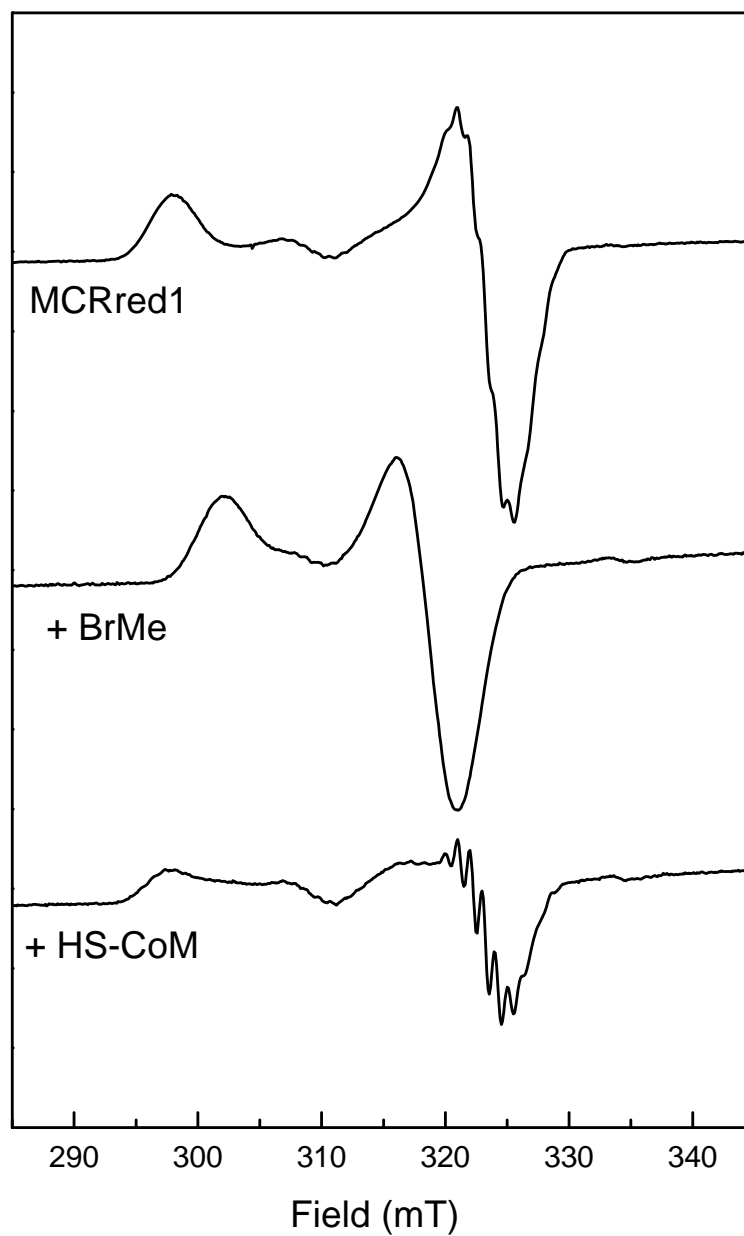


Figure 4-13: EPR spectra of the conversion of MCRred1 into MCR-BrMe with the addition of 50 mM BrMe. The MCR-BrMe signal is partly converted back into the MCRred1 form by addition of 20 mM coenzyme M.

#### 4.4.4 Studies with BPS

For XAS studies it is essential that more than 80% of the nickel ion is present in the desired form. In addition, concentrations of 1 mM or higher will be needed to obtain good data. The presence of coenzyme M in the enzyme samples will interfere with the inhibition of MCR by BrMe, BES and BPS. At the same time, however, the presence of coenzyme M in the buffers will stabilize the protein during the long concentration procedure. Therefore titration studies were performed to determine how much of the bromoalkyl compounds would be needed to get a full conversion of the MCRred1 and/or MCRred2 signals. Figures 4-14 and 4-15 show the data for the titration of MCRred1 and MCRred2 in the presence of 10 mM coenzyme M with increasing concentrations of BPS. In both cases the  $I_{50}$  increased from 50 nM to 3-4  $\mu$ M.

As shown by Ragsdale and coworkers, also the incubation of MCR-BPS with coenzyme M can result in the reformation of MCRred1 and formation of sulfonate propyl coenzyme M [134]. As shown in Figure 4-16, panel A, extensive washing with buffer containing 10 mM coenzyme M resulted in the formation of small amounts of MCRred1 at pH 7.0. This amount became larger at pH 9.0. Overall, the amount of red1 formed was much smaller than the original amount of MCR-BPS present. Most of this form became EPR-silent upon washing. Figure 4-16, panel B, shows a much different effect for the MCR-BPS form that is derived from MCRred2. In this case the washing procedure does not result in any loss of signal intensity of the MCR-BPS species and the formation of MCRred1 is not detected.

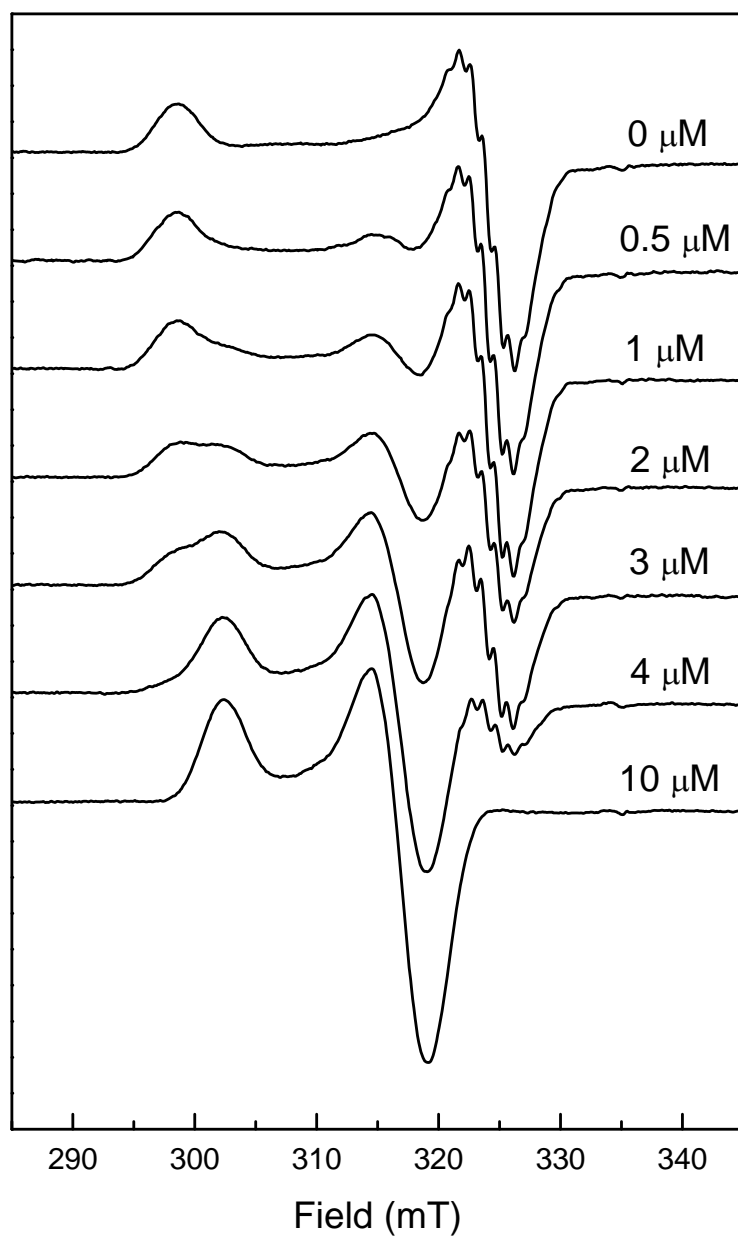


Figure 4-14: Titration of MCRred1 (10  $\mu\text{M}$ ) with different amounts of 3-bromopropane sulfonate (BPS). All samples contain 10 mM coenzyme M. Samples were incubated for 1 min before freezing.

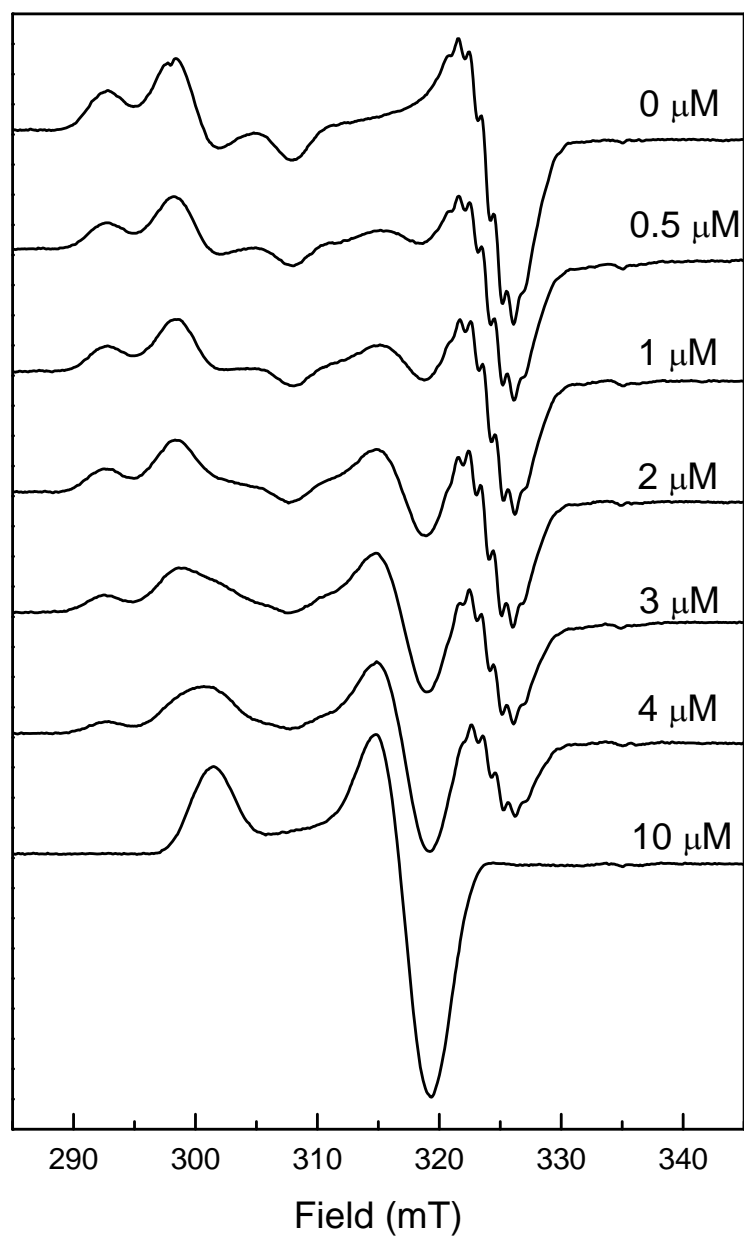


Figure 4-15: Titration of MCRred2 (10  $\mu\text{M}$ ) with different amounts of 3-bromopropane sulfonate (BPS). All samples contain 10 mM coenzyme M. Samples were incubated for 1 min before freezing.

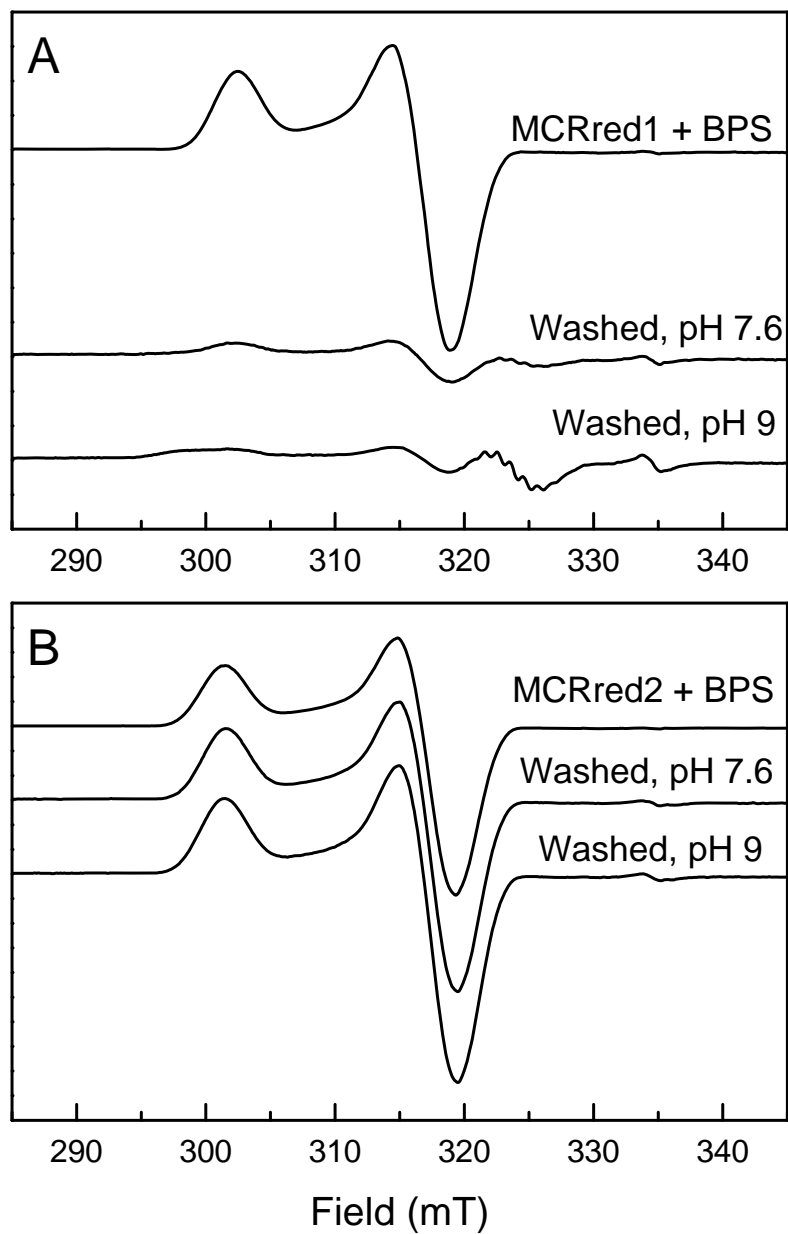


Figure 4-16: Effect of coenzyme M on MCR-BPS formed from MCRred1 (A) and MCRred2 (B). In both cases the samples were washed with buffer containing 10 mM coenzyme M at either pH 7.0 or 9.0.

#### 4.4.5 Studies with 2-Bromoethanesulfonate (BES)

2-Bromoethanesulfonate (BES) is also an inhibitor of MCR, but not as strong as BPS,  $I_{50} = 4 \mu\text{M}$  vs 50 nM. The effect of BES on MCR in the red1 state is completely different than that of both BPS and BrMe. Instead of the formation of a Ni(III) species, with a sixth axial ligand being a C-atom from either BPS or BrMe, an EPR-silent species is formed, indicating a +2 oxidation state for the nickel (Figure 4-17). Unfortunately, this prevents the characterization of this species by EPR spectroscopy. In section 4.5, we present the XAS studies on this form and compare these with data obtained for the MCR-BPS and MCR-BrMe species.

A close examination of Figure 4-17 shows that the EPR spectrum is not completely EPR silent. A weak signal can be detected that is due to MCROx1, showing that this form is not affected by the addition of BES, since this signal is also detectable in the original MCRred1 spectrum. A second signal is detectable in the spectrum that resembles a radical-type signal which is split into two. This radical signal is hardly detectable when BES is added to the red1 form. When BES is added to the red2 form, however, the same radical signal can be detected with much higher signal intensity. Figure 4-19 shows a close up of the radical. The radical shows a two-fold split, which is for example detected in glycy radicals, but two weaker wings are also detectable which makes this signal unique.

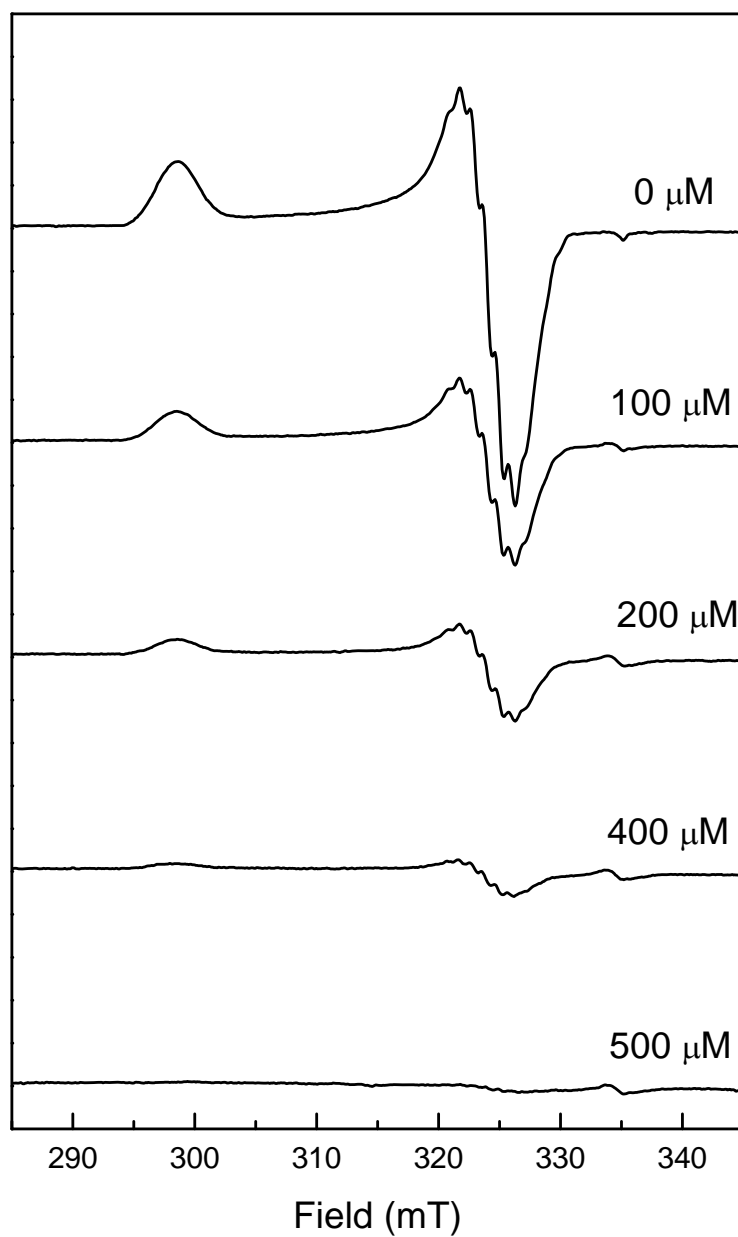


Figure 4-17: Titration of MCRred1 (60 μM) with different amounts of 2-bromoethane sulfonate (BES). All samples contain 10 mM coenzyme M.

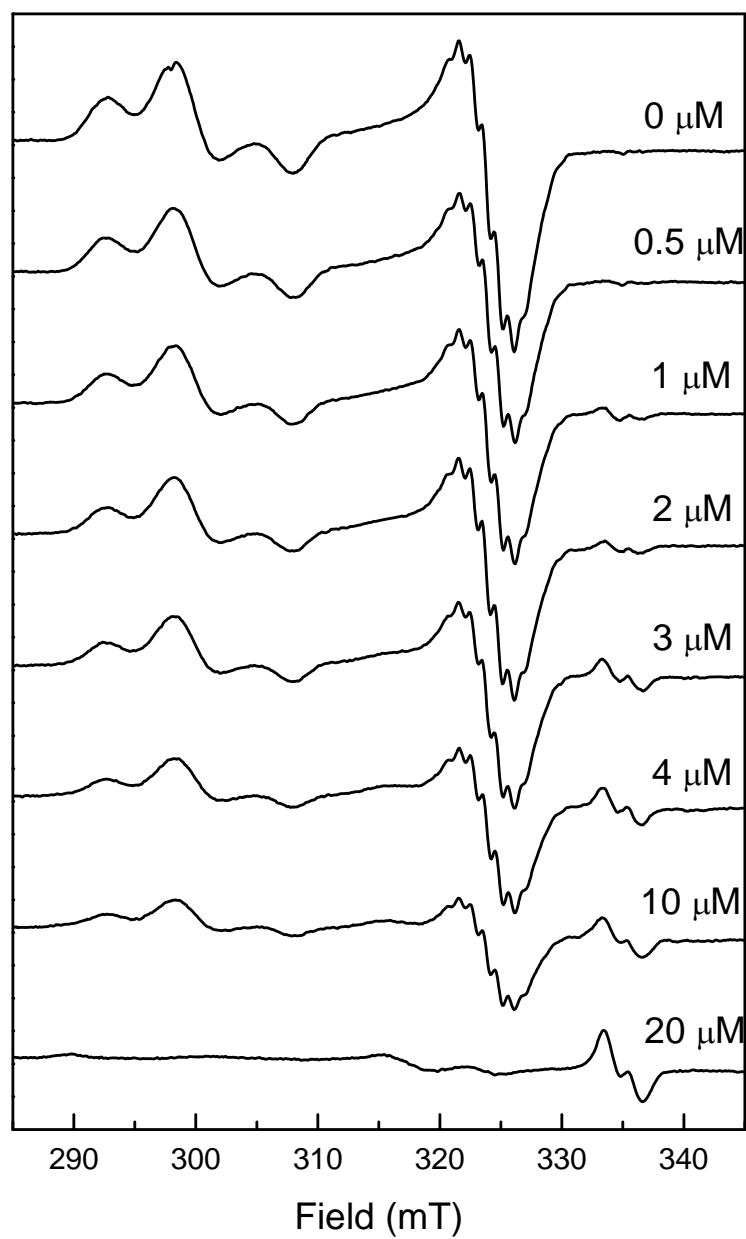


Figure 4-18. Titration of MCRred2 (10  $\mu\text{M}$ ) with different amounts of 2-bromoethane sulfonate (BES). All samples contain 10 mM coenzyme M.

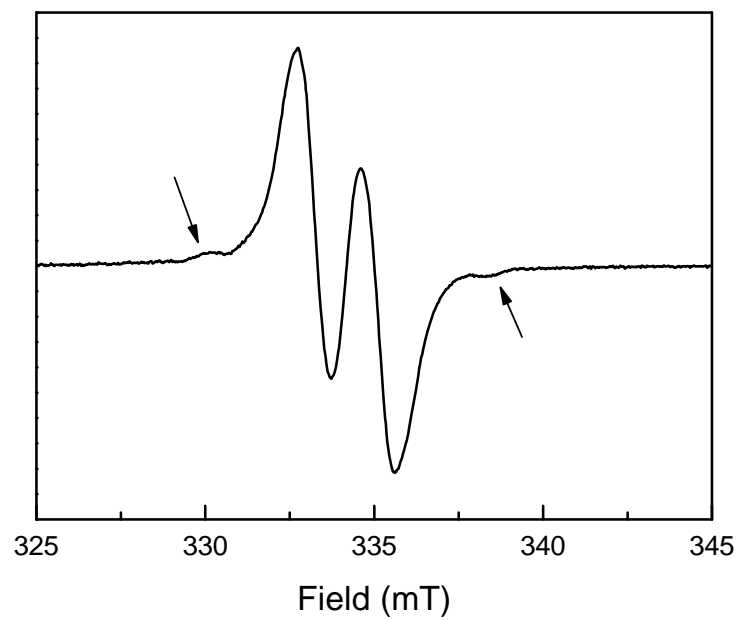
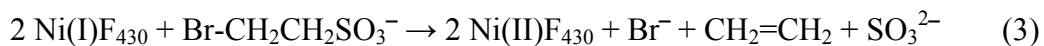
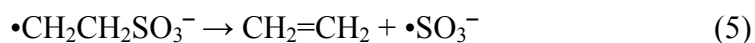
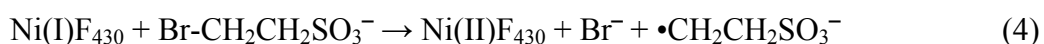


Figure 4-19: Detailed X-band EPR spectrum of the radical-type EPR signal detected after treatment of MCRred2 with 2-bromoethane sulfonate (BES).

It is unclear what the origin of this species is, but studies with the free  $F_{430}$  might give some hints: BES has been shown to react with free  $Ni(I)F_{430}$  to bromide, ethene and sulfite [135]:



Probably the following reaction sequence takes place:



Reaction of  $F_{430}$  in the active site of MCR with BES cannot proceed via the same sequence since a second  $F_{430}Ni(I)$  is needed for reaction (6), but only one  $F_{430}Ni(I)$  is present in the active site. It was proposed that the sulfite anion radical, being a strong oxidant, can probably generate other radicals within the active site [59]. Within the active site there is a thioglycine and two tyrosine residues that could be oxidized by the sulfite anion radical to a thioglycyl radical or a tyrosyl radical, respectively [136]. The split EPR signal is most similar to that reported for other glycyl radicals in proteins [137, 138]. The only glycine residue present in the active site is the thioglycine. Detailed ENDOR studies to address this issue are presented in section 4-7.

#### **4.5 X-ray Absorption Spectroscopy Measurements on the MCR-BPS, MCR-BES and MCR-BrMe Forms**

X-ray absorption measurements were performed to investigate the coordination number of the nickel of F<sub>430</sub> after treatment of the MCRred1 state with BES. One explanation for the formation of the radical species is that after the initial formation of a Ni(III)-C species, an electron is transferred to the alkylsulfonate group resulting in the formation of ethene, sulfonate and an amino-acid-based radical. This leaves the 6<sup>th</sup> axial site open and the nickel would be 5-coordinated. It is also possible that another process takes place that causes the nickel to become +2 but leaves the Ni-C bond in place. In this case the nickel would be 6-coordinated.

With this technique it is very difficult to tell the difference between a 5- and 6-coordinated metal. However, as shown for the red1 state sometimes these assignments can be made. When we started these types of experiments initially, we were actually testing if a Ni-Br bond was formed. This would have been very easy to show with this technique.

Figure 4-20 shows the data obtained for two samples that contained different amounts of the MCR-BPS EPR signal, 0.67 spin (solid line) and 0.34 spin (dotted line). The remainder of MCR was present in an EPR-silent form. Figure 4-21, shows the data for the MCR-BES species (solid line). The spectra data displayed with a dotted line is from an MCR-BES sample that has been extensively washed with buffer. This was initially done to remove the excess of BES so we would be able to measure Br-XAS to

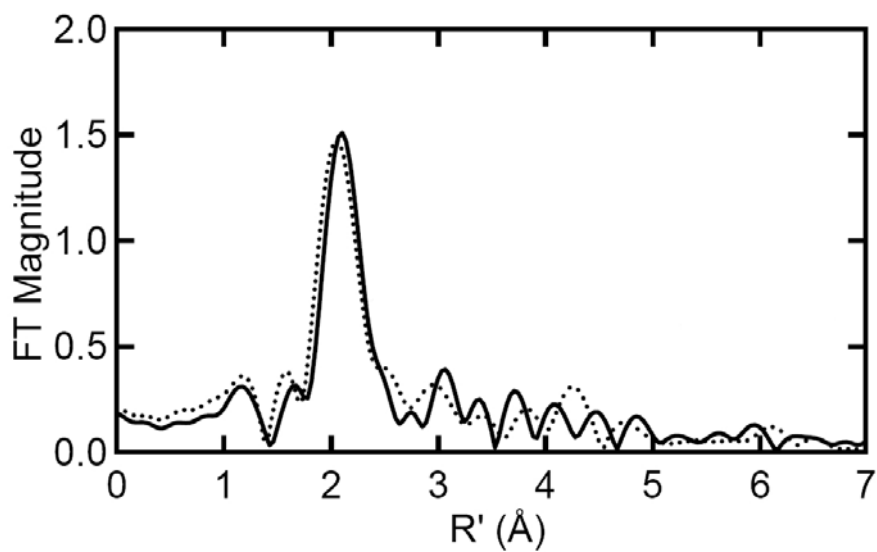
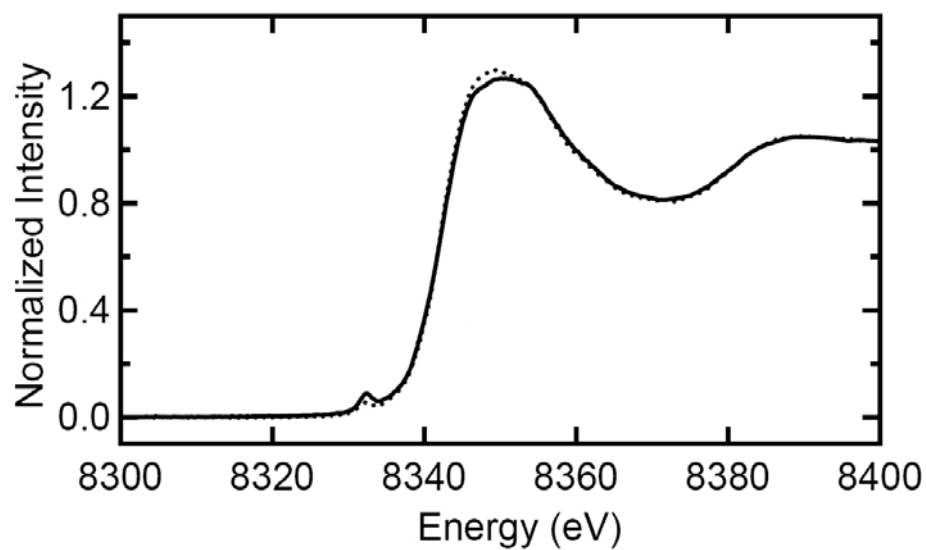


Figure 4-20: XAS data for MCR-BPS. The data were measured for two samples with different amounts of MCR-BPS present: 0.67 spin (BPS II, —) and 0.34 spin (BPS I, ⋯).

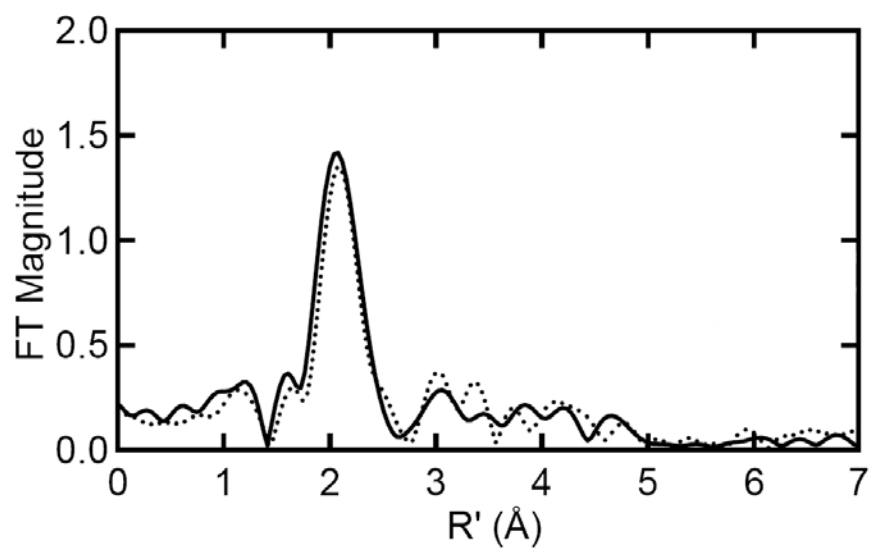
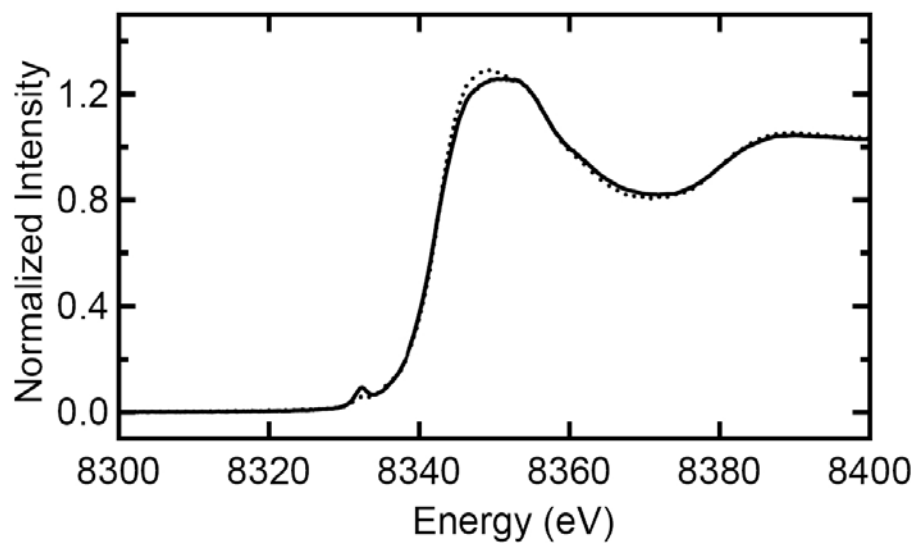


Figure 4-21: XAS data for MCR-BES as such (BES I, —), and extensively washed (BES II, ⋯).

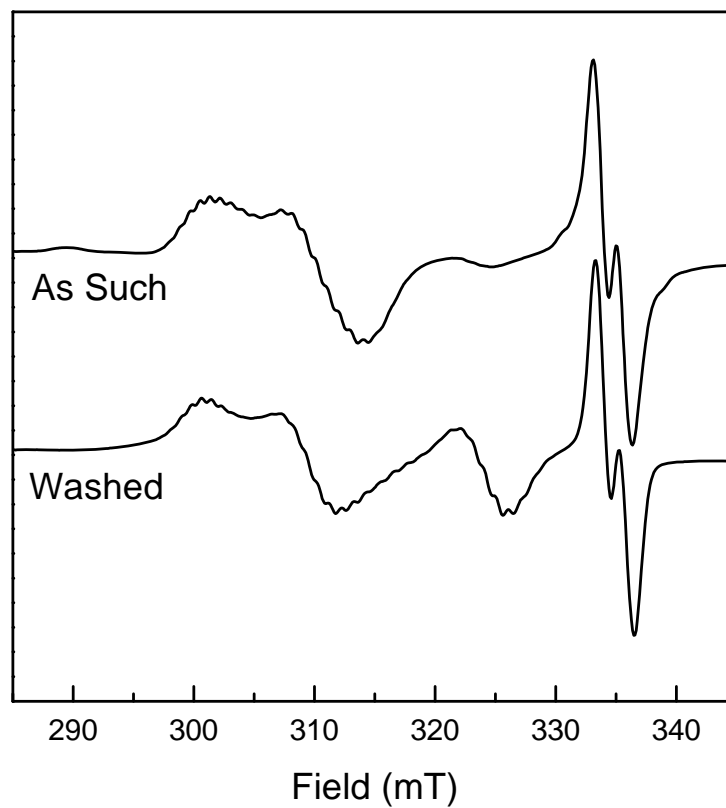


Figure 4-22: EPR data for the XAS samples from Figure 4-22, MCR-BES as such and extensively washed with buffer containing 10 mM coenzyme M. Signal intensity was corrected for the nickel concentration.

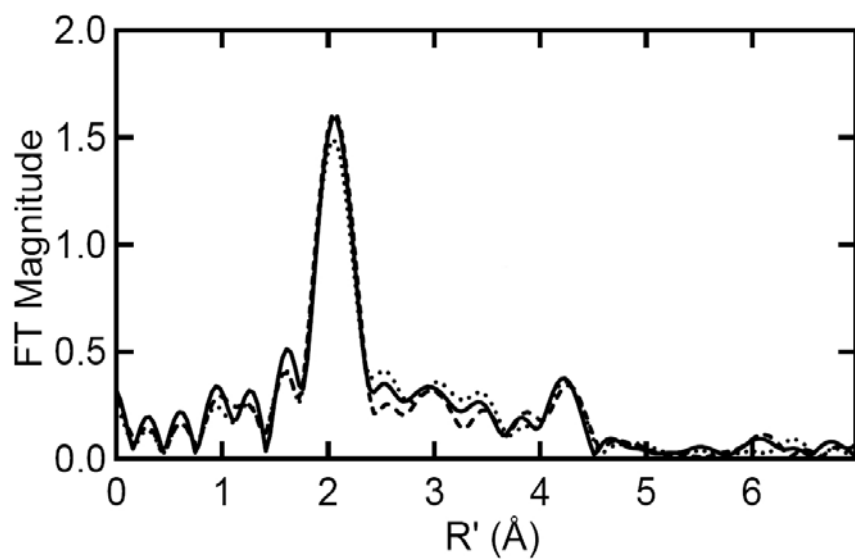
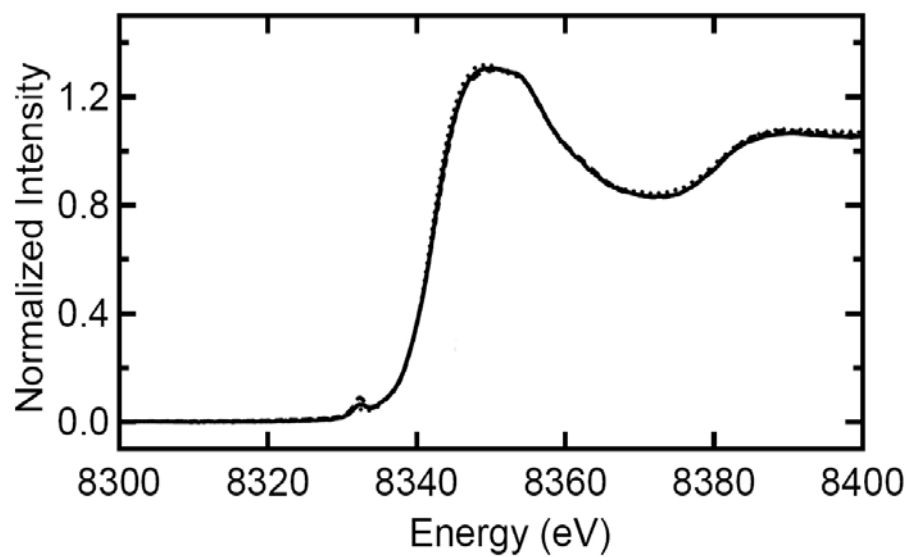


Figure 4-23: Overlay of the XAS data for MCR-BPS (BPS II, ---), MCR-BES (BES I, ···) and MCR-BrMe (BrMe III, —).

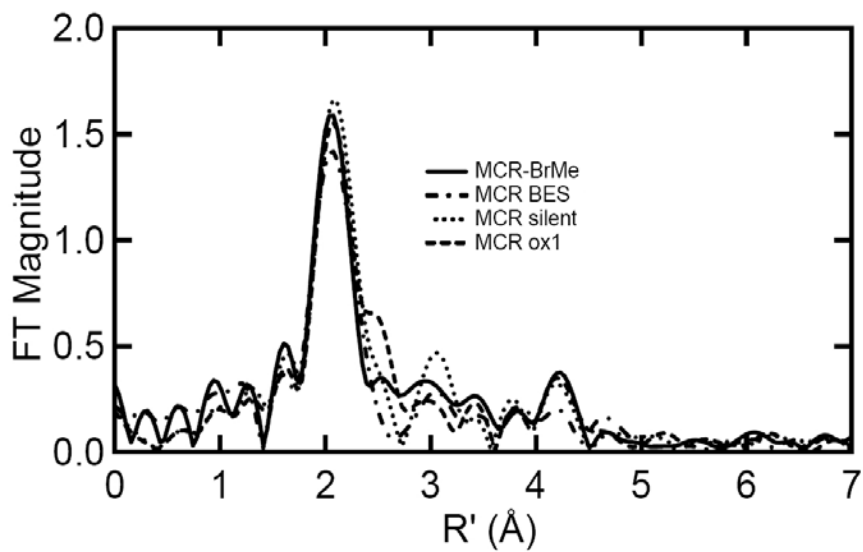
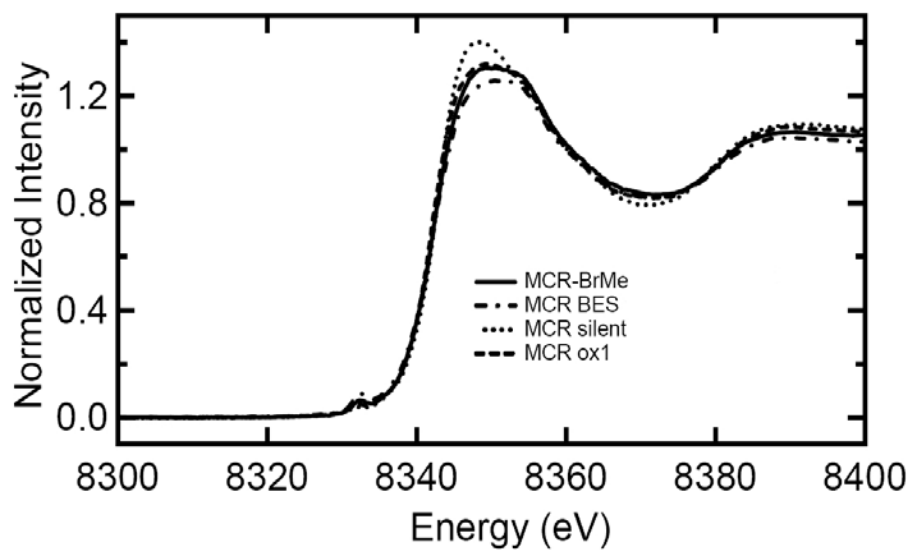


Figure 4-24: Overlay of the XAS data for MCR-BrMe (BrMe III, —), MCR-BES (BES I, ---), MCRsilent (····) and MCRox1 (---).

detect if a Ni-Br bond was formed. The intensity of the bromine signal as detected with Br-XAS was very low and could be attributed to traces of BES present in the sample (not shown). Figure 4-22 shows the EPR spectra that were measured of EPR samples made in parallel to the XAS samples. In this case the washing procedure did not result in a large change in the EPR spectra since the initial MCR-BES form was already EPR silent. However a small amount of MCRred1 is formed that was not present before the washing procedure.

Figure 4-23, show an overview of the MCR-BPS (dashed line), MCR-BES (dotted line) and MCR-BrMe (solid line) samples. The figure shows that the data obtained for all the species are very similar. Figure 4-24, shows an overlay of the data for MCR-BrMe (solid line), MCR-BES (dash-dot line), MCRsilent (dotted line) and MCRox1 (dashed line). The height of the FT magnitude (Fig. 4-24, bottom panel) is a measure for the amounts of ligands present. The MCR-BES sample shows the lowest value. However, the difference in FT Magnitude for the MCR-BES sample and the other samples are not as large as those observed for the MCRred1 forms (Fig. 1-8) and would not indicate a difference in coordination. From this it can be either concluded that in all three forms a 6-coordinated nickel ion is present, or that in this case we cannot tell the difference using this method. However, there is a part of the spectrum that at first did not seem to make sense but actually turned out to be very important. In the pre-edge region at -8332 eV the MCR-BPS samples show a small peak that is due to the 1s-3d transition. This transition should be forbidden for nearly centrosymmetric 6-coordinate sites, but will grow in for non-centrosymmetric 5-coordinate site (or tetrahedral) (Fig. 2-14) [108]. The intensity of

this feature is large for both MCR-BPS and MCR-BES. In the case of MCR-BPS the signal intensity of the 1s-3d transition becomes larger when the EPR spin intensity of the MCR-BPS signal increases. This seems to go against logic since the nickel in MCR-BPS is 6-coordinated. The ENDOR data for MCR-BPS and the DFT calculations for this species, however, showed that the Ni-C bond is bending away from the axis perpendicular to the plane of the tetrapyrrole ring. This could be the reason for the more non-centrosymmetric property of the nickel in MCR-BPS.

Although we cannot measure the spin intensity for the MCR-BES form, it can be assumed that the intensity should be related to the original amount of MCRred1 present. We do see that samples that initially had more red1 present show more of the 1s-3d feature in XAS which therefore can be assigned to the MCR-BES species. Interestingly, washing of the MCR-BES sample with coenzyme M containing buffer results in the loss of this pre-edge feature. Based on this it can be proposed that a Ni-C bond is present in MCR-BES. Similarly to the bond in MCR-BPS, the Ni-C bond must be bending away from the axis perpendicular to the plain of the F<sub>430</sub> ring. The washing procedure results in the breaking of the Ni-C bond in MCR-BES, but for an unknown reason only a small amount of MCRred1 is formed. Most protein ends up being EPR-silent.

#### 4.6 Detection of Bromide

The treatment of MCRred1 with either BPS or BrMe resulted in the formation of a Ni-C bond. It has been proposed that formation of this bond results in the displacement of the bromide atom as bromide ion. The XAS data presented above indicate that in the treatment of red1 with BES a Ni-C bond was also formed. That means that the treatment with BES should also result in the release of bromide ion. To test this, the formation of bromide ion was tested in a colorimetric assay using the reduction of the permanganate ion by the bromide ion.

In this experiment four samples were prepared. First of all the enzyme was washed extensively since coenzyme M also reacts with the permanganate ion. Sample 1 was MCR in the red1 form and served as a control for the washing step. Sample 2 was MCRred1 treated with BES, Sample 3 was MCRred1 treated with BPS. Sample 4 was MCRred1 treated with BrMe. All samples were concentrated using an Amicon ultrafiltration unit and the filtrate was tested for bromide ion.

In this experiment, it was found that in the case of BrMe-treated enzyme, the filtrate had a yellow color due to the presence of free F<sub>430</sub>. Therefore this sample could not be used in this assay. A second drawback of this method is that in the absence of coenzyme M, the red1 forms becomes unstable and during the washing step a large amount of the MCRred1 form is lost. As a result, only small changes were detected in the assay. Figure 4-25, bottom, shows the data obtained for one experiment. Control 1 is the spectrum of the permanganate solution. Control 2 is the filtrate obtained with untreated enzyme.

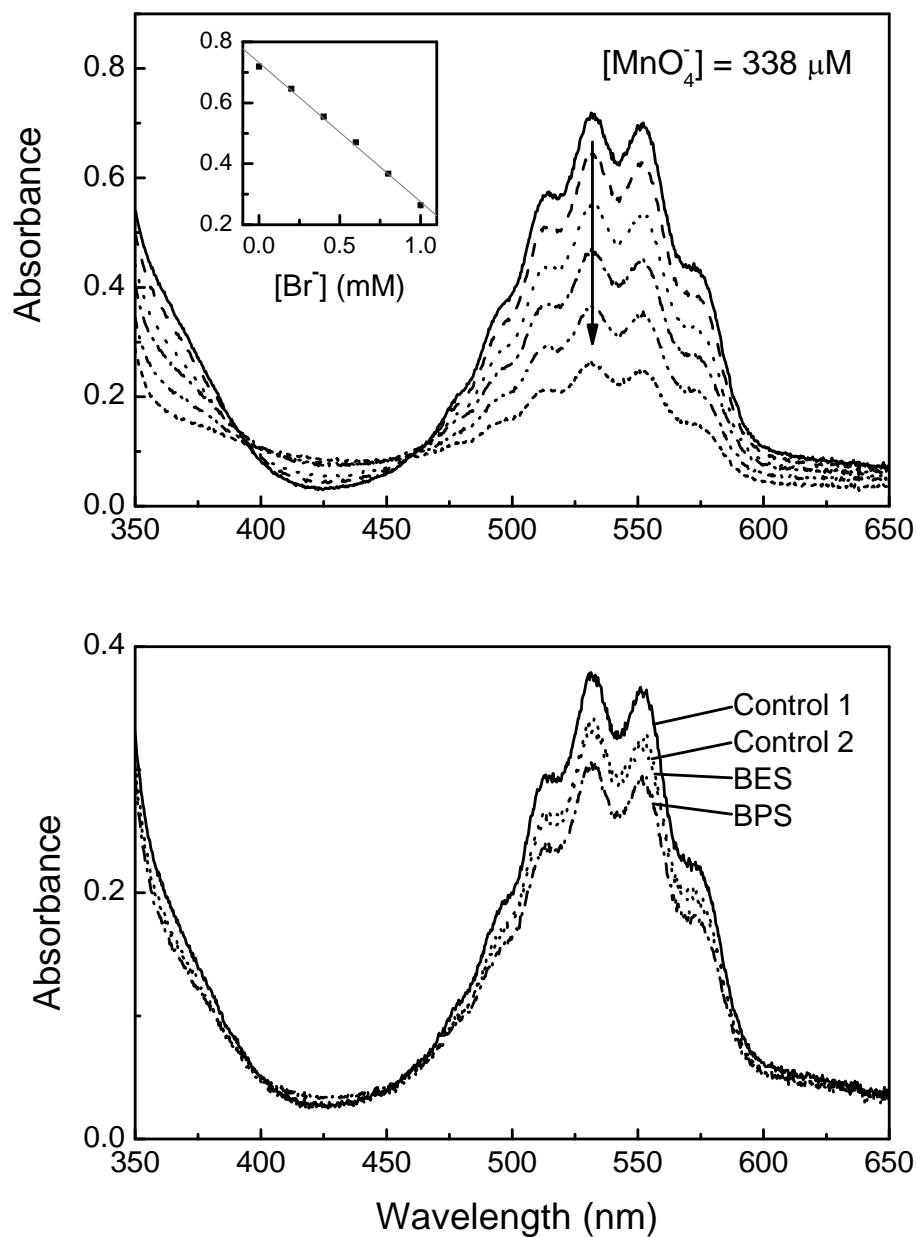


Figure 4-25: Assay for bromide. Top: Calibration curve for the reduction of permanganate ion with bromide ion. Bottom: Absorption spectrum for permanganate ion as such (control 1), plus filtrate of untreated enzyme (Control 2), plus filtrate of BES treated enzyme (BES), and plus filtrate of BPS treated enzyme (BPS).

Apparently there is still some coenzyme M left in the washed protein sample. The BPS sample shows a further decrease in absorption that can be attributed to bromide formed as a result of the addition of BPS. In this case, the amount of bromide calculated from the changes in the EPR spectra corresponded to the amount of bromide detected. The spectrum for BES sample, however, did not indicate the presence of bromide ion. Although the results are interesting, further attempts to repeat this assay showed that with the small amounts of the MCRred1 form left after the wash step and the relative low sensitivity of the assay, we are very close to the detection limit.

#### **4.7 ENDOR results of radical in MCR-BES**

Below is the X-band and W-band EPR spectrum of the radical detected MCR-BES (Fig. 4-26 and 4-27). The EPR parameters are:  $g_{\perp} = 2.0033 \pm 0.0005$ ,  $g_{\parallel} = 1.9990 \pm 0.0005$  with two detectable proton couplings:  $A_1(^1\text{H}) = [55\ 55\ 58]$  MHz,  $\pm 1$  MHz on all values and  $A_2(^1\text{H}) = 20$  MHz,  $\pm 2$  MHz (All these parameters are get from simulation program and provided by Dr. J. Hammer) . These values all seem to be a bit different than any of the known radical species (see table 5-1). All the known amino acid based radical species are rhombic; however, the MCR-BES radical species is axial. Also the coupling constants are also different between MCR-BES radical species and other known amino acid based radical species [139].

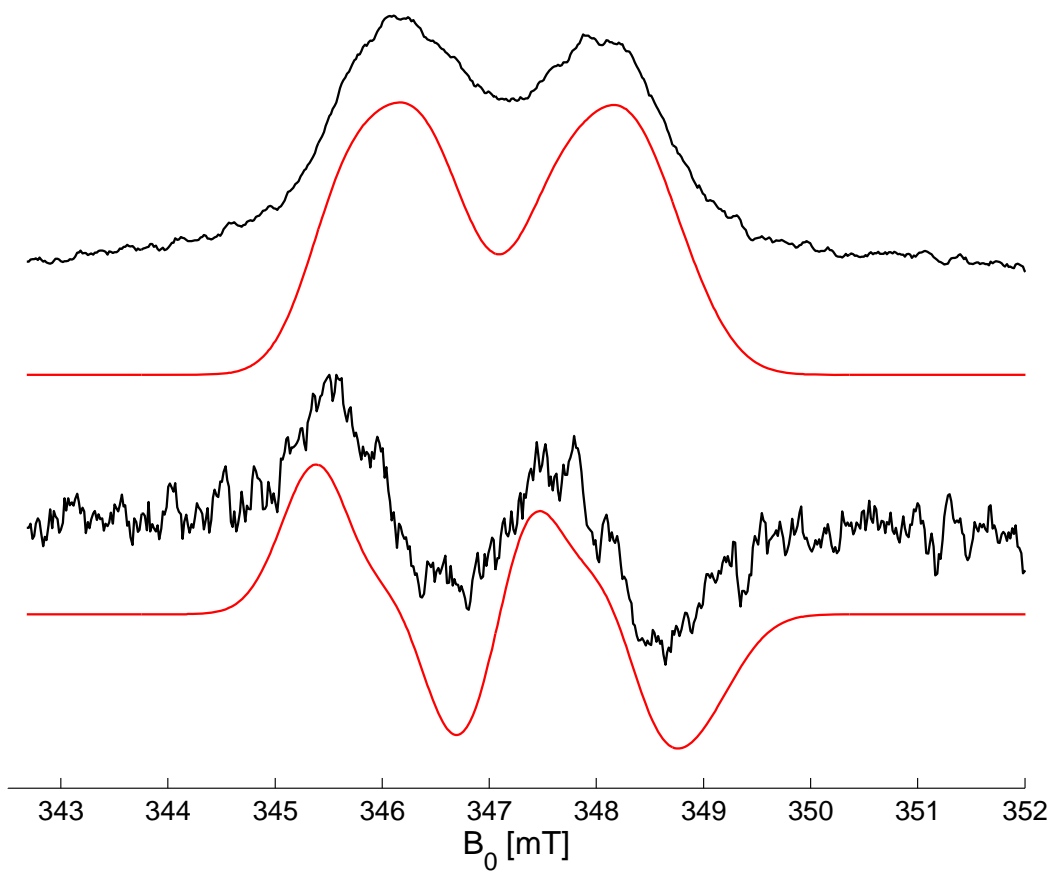


Figure 4-26 X-band ENDOR spectrum of MCR-BES radical (red line is the simulation signal) (provided by Dr. J. Hammer)

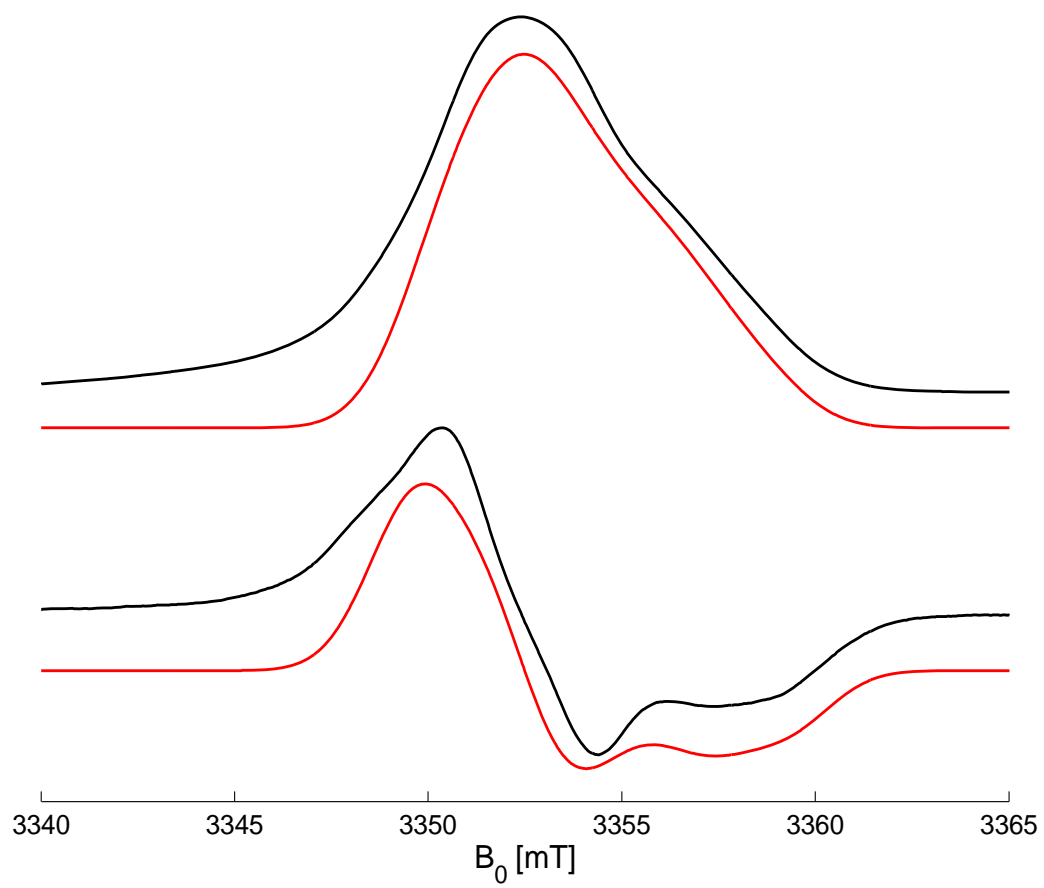
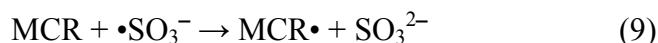
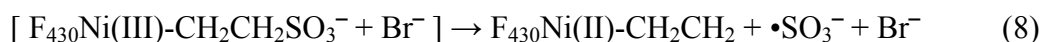
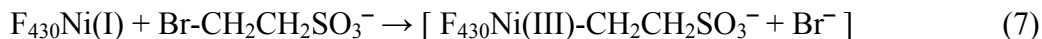


Figure 4-27 W-band ENDOR spectrum of MCR-BES radical (red line is the simulation signal) (provided by Dr. J. Hammer)

#### 4.8 Effect of other substrate analogs on the red1 and red2 forms of MCR

Based on the XAS and EPR data presented above it can be concluded that a Ni-C bond is present in the MCR-BES form. An alternative set of reactions can be given to explain the formation of the radical:



We propose that a Ni(III)-alkylsulfonate species is formed that immediately breaks apart at the weak C-S bond, forming the sulfonate radical and finally the amino acid-based radical. To test this hypothesis we incubated the MCRred2 with bromopropionic acid (Br-CH<sub>2</sub>CH<sub>2</sub>CO<sub>2</sub><sup>-</sup>). In this case there is no labile C-S bond present and a stable Ni(III)-alkyl species should be formed. Figure 4-28, however, shows that also in this case a radical species is formed instead of a stable Ni(III)-alkyl species. The radical species shows the same two-fold split but some more ‘wings’ are detectable indicating additional interactions with surrounding nuclei.

As shown in section 1.5.3, several inhibitors and substrate analogs are known for MCR. In this study we tested the effect of these inhibitors on the MCRred1 form in the presence and absence of coenzyme B. No MCRred2 is detectable due to the removal of coenzyme M by extensive washing of the protein. The effects on both forms are almost identical, with the exception that several compounds quench the MCRred1 signal, while

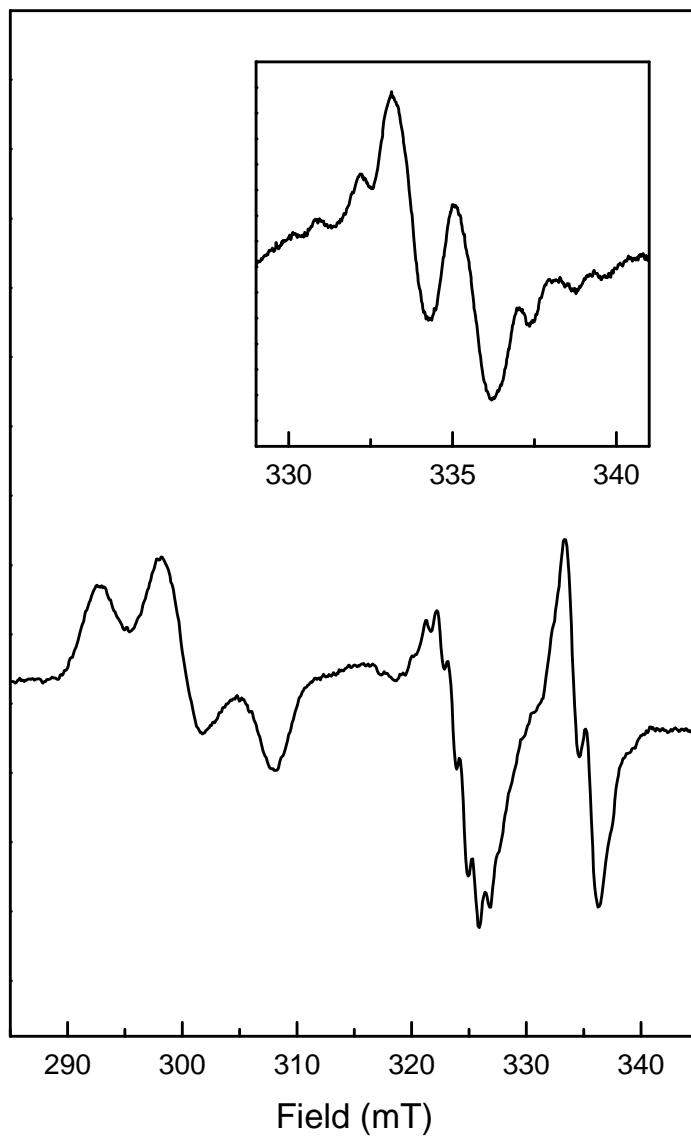


Figure 4-28: Effect of bromopropionic acid on MCRred2. The insert shows the radical signal measured under non-saturating conditions. MCR concentration, 50  $\mu\text{M}$ ; coenzyme M, 10 mM; coenzyme B, 5 mM; bromopropionate, 5 mM. Sample was incubated for 10 min with bromopropionate.

in the presence of coenzyme B a small two-fold radical is induced (Fig. 4-29). Ethylsulfonate ( $\text{C-C-SO}_3^-$ ) and propylsulfonate ( $\text{C-C-C-SO}_3^-$ ) are actually not inhibitors and as expected no effect is detected when these compounds are added to MCRred1 in the presence and absence of coenzyme B. Allyl-coenzyme M also does not have any effect. Surprisingly, BES, selenocoenzyme M ( $\text{HSe-C-C-SO}_3^-$ ), cyanocoenzyme M ( $\text{NC-S-C-C-SO}_3^-$ ) and trifluoromethyl-coenzyme M ( $\text{CF}_3\text{-S-C-C-SO}_3^-$ ) all quench the MCRred1 EPR signal in the absence of coenzyme B and induce the small two-fold split radical EPR signal when coenzyme B is present.

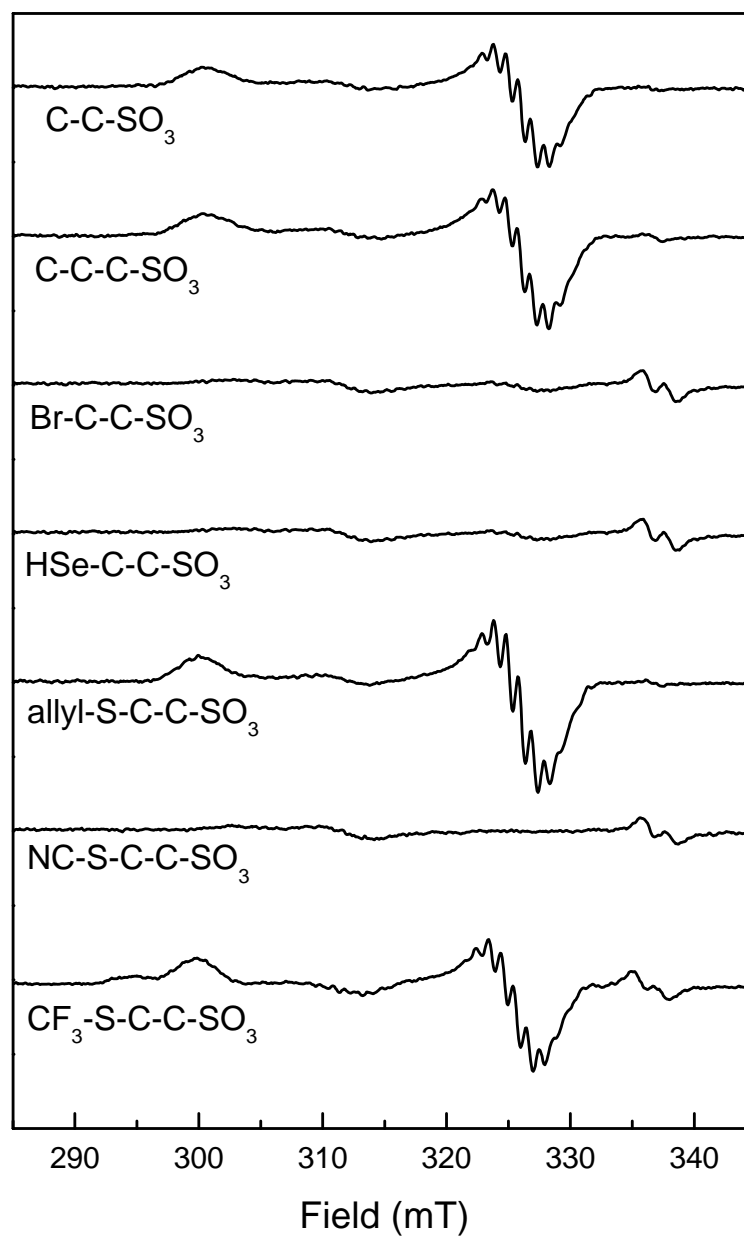


Figure 4-29: Effect of several substrate analogs and inhibitors on the MCRred1 form in the presence of 5 mM coenzyme B. Coenzyme M was removed by washing. See text for details.

## CHAPTER FIVE

### DISCUSSION AND CONCLUSION

#### 5.1 Studies with Bromo-alkyl Species

The studies with BPS and BrMe showed that it is possible to form a Ni-C bond in the active site of MCR. In particular the formation of a Ni-CH<sub>3</sub> is very interesting. The formation of this species, however, is achieved in a very artificial way. Therefore it is not proven that a Ni-CH<sub>3</sub> species is actually formed during the reaction mechanism. The species, however, is relatively stable which shows that such a species could be formed. This finding is very important since several groups have proposed theoretical models that include such a reaction intermediate. On top of that the ‘back reaction’ of the MCR-BrMe form with coenzyme M could be a good model for the AMO reaction.

The MCR-BPS and MCR-BrMe species have been studied in detail [59, 94, 133] and are well understood. About the MCR-BES form less is known, mainly because this species is EPR silent. In this work we showed that all three species showed very similar XAS spectra. The high intensity of the pre-edge feature for MCR-BPS and MCR-BES would be more in line with a 5-coordinated nickel in these forms. ENDOR, however, shows the present of a Ni-C bond in MCR-BPS. The fact that the 6-coordinated nickel is not centrosymmetric could be related to the fact that the Ni-C bond is not perpendicular

to the plain of the  $F_{430}$  ring. DFT calculation shows that there is an angle between the Ni-C bond and the axis (Fig. 5-1, B). In addition, all three forms show a partial ‘back reaction’ with coenzyme M, where part of the Ni-alkyl species are converted back into MCRred1. From these similarities it can be concluded that there is a Ni-C bond present in the MCR-BES form. It is not clear why this form is EPR silent. Apparently, it is possible to have ‘Ni(III)-C’ and ‘Ni(II)-C’ species present in MCR just like it is possible to have a ‘Ni(III)-S’ species in MCRox1, a ‘Ni(II)-S’ species in MCRox1silent, and even a ‘Ni(I)-S’ species in MCRred2-rhombic. The question that remains is the fate of the free electron in the conformation of the Ni(I) in MCRred1 into Ni(II) in MCR-BES. This will be discussed in the next section.

The incubation of MCRred1 with BPS and MCRred2 with BPS results in identical EPR signals (Figure 4-17 and 4-18). After washing with buffer, containing 10 mM CoM some MCRred1 is formed back in the sample that originally was MCRred1; however it does not happen with the sample that was MCRred2. It indicates that coenzyme B has a very important effect during this reaction. It may be due to the structure of the active site. The crystal structures of the MCRox1-silent form and MCRsilent form (Fig. 1-5) show that coenzyme B binds at the mouth of the active site channel. Washing the MCRred1+BPS sample results in the formation of MCRred1 because there is no coenzyme B blocking the reaction channel. But in the MCRred2+BPS sample, there is coenzyme B present. In the MCRred2 form coenzyme M and coenzyme B are present in the channel, but the binding is not very strong. Even with both compounds present BPS can enter the

channel and react with the nickel. However, after this reaction, the binding of coenzyme B becomes much stronger, maybe even irreversible.

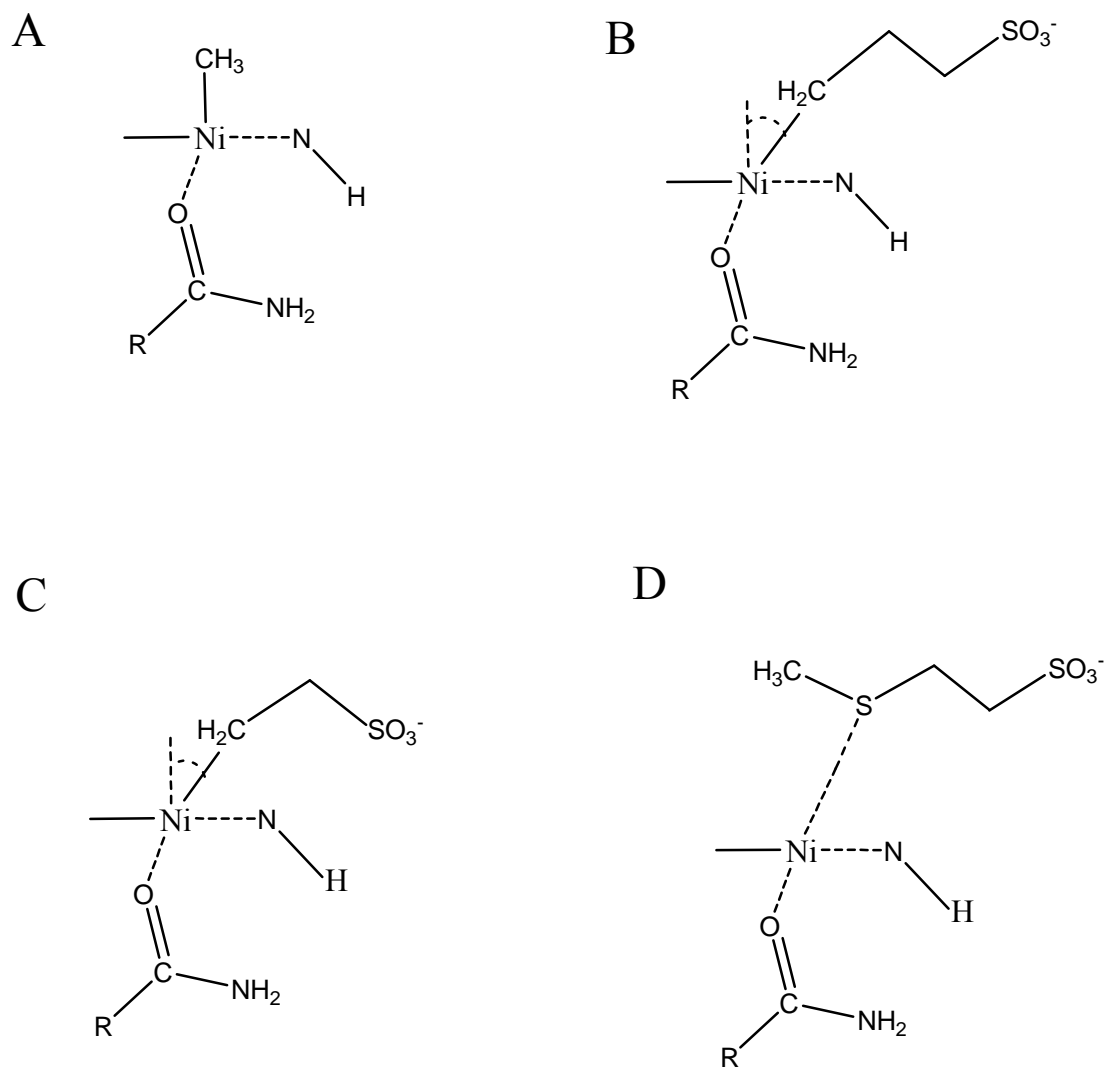


Figure 5-1: Models for the coordination around the nickel ion in MCR-BrCH<sub>3</sub> (A), MCR-BPS (B), MCR-BES (C), and MCR-CH<sub>3</sub>-CoM (D)

## 5.2 Origin of the radical species

Treatment of MCRred1 with BES in the presence of coenzyme B results in the quenching of the Ni(I) signal and the formation of a radical species. It was proposed that initially a Ni(III)-C bond was formed but that instability of this bond would result in a cascade of reactions with the final formation of an amino-acid-based radical species (see reactions on p. 127). Here, however, we have shown that the Ni-C bond probably stays intact.

One possibility is that instead of the Ni-C bond the C-SO<sub>3</sub><sup>-</sup> bond will break to form a •SO<sub>3</sub><sup>-</sup> radical. This radical can then be transferred to a nearby amino acid (see reactions on p. 142). Bromopropionic acid, (Br-C-C-CO<sub>2</sub><sup>-</sup>), however, induces a radical species instead of a Ni(III)-alkyl species. We need a different explanation for this reactivity since the C-CO<sub>2</sub><sup>-</sup> bond would be too strong to break up, and we would not expect the formation of a •CO<sub>2</sub><sup>-</sup> radical.

BES and bromopropionic acid are not the only compounds that can induce the radical signal. Figure 4-29 shows that selenocoenzyme M (HSe-C-C-SO<sub>3</sub><sup>-</sup>), cyanocoenzyme M (NC-S-C-C-SO<sub>3</sub><sup>-</sup>) and trifluoromethyl-coenzyme M (CF<sub>3</sub>-S-C-C-SO<sub>3</sub><sup>-</sup>) all quench the MCRred1 EPR signal in the absence of coenzyme B and induce the small two-fold-split radical EPR signal when coenzyme B is present. These compounds are all very different. The bromo alkyl species react and form a Ni-C bond. CH<sub>3</sub>-Se-CoM is a very good substrate and it could be expected that in analogy to HS-CoM, HSe-CoM would form a Ni-Se bond. CF<sub>2</sub>-S-CoM is still a substrate; CF<sub>3</sub>-S-CoM is not. Still

addition of CF<sub>3</sub>-S-CoM to MCR could result in either a Ni-C or a Ni-S bond. It is not clear how these different modes of binding could result in the formation of the same radical species. To come up with a unifying mechanism it can be proposed that all these compound could bind to the nickel via a sulfonate oxygen as shown in Figure 5-2, structure A. However a quenching of the Ni(I) signal is not detected with either ethyl sulfonate or propyl sulfonate (Fig. 4-29). Based on an alternative reaction mechanism, as described below, it is also possible that the electron density is transferred from the nickel to the coordinating glutamine residue (Figure 5-2 B).

From the ENDOR spectra of this species (Fig. 4-26 and 4-27), it is not possible to draw a strong conclusion. The data is in line with both a (thio) glycil species and a tyrosyl species (Table 5-1). The lack of interaction from nitrogen would make a glutamine based radical less likely.

Table 5-1. Comparison of g-Values and Isotropic Hyperfine Values of the RNR, PFL, and BSS Glycyl Radical with Those of the N-Acetyl Glycine Radical, Tyrosyl Radical, and Tryptophan Radical [140]

	$g_x$	$g_y$	$g_z$	$\Delta(g_z-g_x)$
RNR	2.0043	2.0033	2.0023	0.0020
PFL	2.0047	2.0039	2.0025	0.0022
BSS	2.0045	2.0036	2.0022	0.0023
N-acetyl glycin radical	2.0045	2.0031	2.0020	0.0025
tyrosyl radical	2.0091-2.0076	2.0046-2.0044	2.0021	0.0070-0.0055
tryptophan radical	2.0035-2.0033	2.0024-2.0025	2.0023-2.0021	0.0018-0.0011

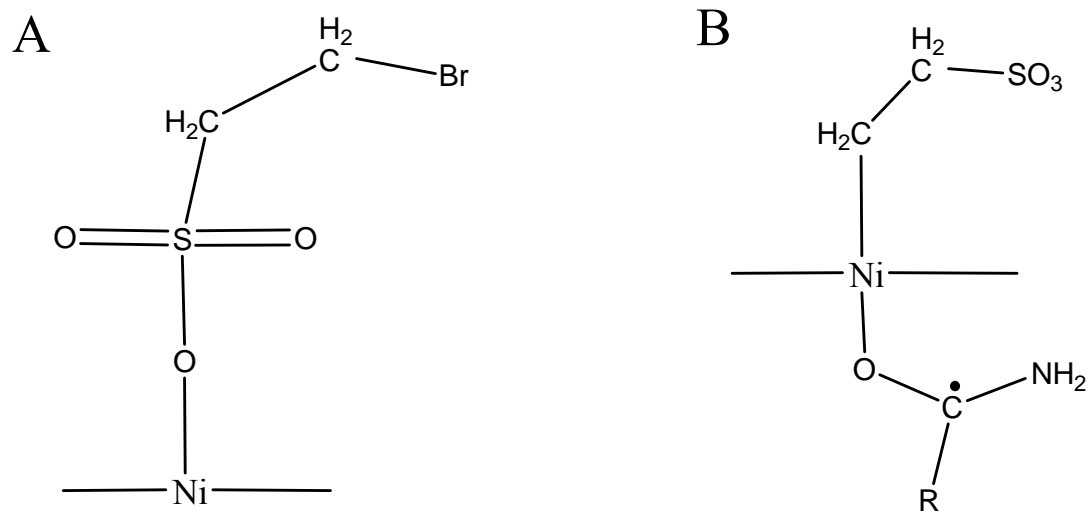


Figure 5-2: Two proposed structures of MCR-BES species

### 5.3 Effect of coenzyme B

Coenzyme B plays a very important role in the study of MCR, not only because coenzyme B is one of the substrates, but also because it can help us with the study of different forms of MCR, especially the MCRred2 form. The MCRred2 form is induced from the MCRred1 form by incubation with coenzyme M and coenzyme B.

ENDOR evidence [141] showed that in the red1 form all four nitrogens are equal, but in the red2-rhombic form there are two sets of nitrogens where one set shows a much smaller superhyperfine coupling constant (Table 5-2). This effect could just be electronic, but could also indicate a considerable conformational change around the nickel.

Crystallization studies also hinted at conformational changes induced by coenzyme B binding. In one structure, the MCRred1-silent structure (Figure 5-3) induced from the active MCRred1 state after air exposure, two superimposed states could be detected: one state devoid of both HS-CoM and HS-CoB and one state with a structure identical to the MCRox1-silent state [34]. The absence of the substrates leads to a conformational change of a glycine rich loop between residues  $\beta$ 366 and  $\beta$ 371 contacting both substrates in the MCRox1silent state (Figure 1-5A). The peptide bonds of residues  $\beta$ 367,  $\beta$ 368 and  $\beta$ 369 are flipped and Tyr $\beta$ 367 no longer points to the axial nickel ligand. Meantime, Tyr $\beta$ 367 forms a hydrogen bond with coenzyme M. In the substrate free state the sixth coordination site of F<sub>430</sub> is empty or loosely occupied by a water molecule in agreement with EXAFS studies on the MCR-red1 state [40]. The conformation of F<sub>430</sub> in the state without substrates is the same as that of the MCRox1silent state except for a rotation of

Table 5-2:  $^{14}\text{N}$  hyperfine parameters of the pyrrole nitrogens of  $\text{F}_{430}$  of MCRred1 and MCRred2

complex		$A_1$	$A_2$	$A_3$
MCR-red1		27.7	28.7	28.6
MCR-red2	$\text{N}_{\text{B,C,D}}$	26.6	23.2	24.0
	$\text{N}_{\text{A}}$	16.0	13.5	11.8

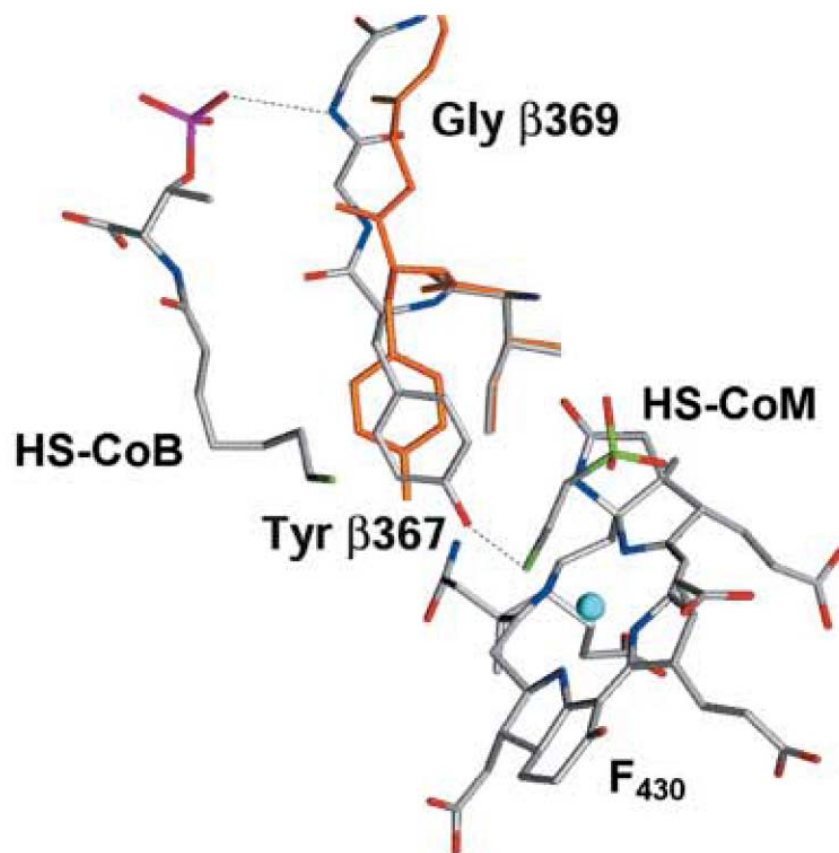


Figure 5-3: The active site of the MCR-red1-silent structure[90]. (We got the permission to use this figure from Dr. U. Ermler)

the lactam ring. Therefore HS-CoB binding to the active site channel might induce a conformational change, necessary to initiate the methane forming reaction.

Previous studies showed that the thiol sulfur atom of coenzyme B is important for the induction of the MCRred2 form. Adding a -CH<sub>3</sub> or -CF<sub>3</sub> group did not change this effect. It was expected (or hoped for) that using CH<sub>3</sub>-S-CoB or CF<sub>3</sub>-S-CoB together with CH<sub>3</sub>-S-CoM would result in the formation of a Ni-CH<sub>3</sub> species or a Ni-S(CH<sub>3</sub>)(CoM) species. However, a new MCRred1 signal is formed by incubating MCRred1 with methyl-coenzyme M and methyl coenzyme B (Figure 4-8, Spectrum 7). This new signal was not detected previously in similar samples because there were small amounts of coenzyme M present, which can induce the MCRred2 signal with coenzyme B. Samples were prepared with labeled substrates. The coupling constants of the nickel-based free electron with either the <sup>13</sup>C atom or the H/D atoms of the methyl group of methyl-coenzyme M should be able to tell us where the methyl group is located in these samples.

## 5.4 A new mechanism

A new catalytic mechanism for MCR has been proposed by Duin and McKee [142]. The main goal was to find a mechanism that would be chemically reversible. As showed in Figure 5-4 the mechanism has six steps. In the first step a protonation of F<sub>430</sub> takes place, (**complex 2**) the proton comes from the N-atom of the coordinating Gln residue. The proton is replenished via a water channel that connects the Gln residue with the bulk of water outside the protein (Fig. 5-5). The protonation results in a weakening of the bond between the nitrogen atom and the nickel. The sulfur atom from Me-CoM moves close to the Nickel atom to about 3.08 Å and forms a loose Ni-S bond (**complex 3**). This brings the methyl group in position to be transferred to the nickel (**complex 4**). Ni is oxidized from Ni(I) to Ni(III) during this step. Next, CoB will react with CoM; forming CoM-S-S-CoB (**complex 5**). Now the hydrogen atom bound to the F<sub>430</sub>-N-atom gets closer to the methyl group ready to form methane (**complex 6**). In the last step Methane is released and Ni goes back to the Ni(I) form (**complex 1**) ready to start the next cycle.

Two alternative reactions are possible starting from **complex 3** [142]. Rather than adding CH<sub>3</sub>S<sup>-</sup> from coenzyme M, **complex3** can lose methane (Figure 5-4, alt. 2), forming **complex 8**. The high activation barrier for this step (53.7 kcal/mol) strongly suggests that the addition of SCH<sub>3</sub><sup>-</sup> (followed by loss of CH<sub>3</sub>-S-S-CoB<sup>-</sup>) precedes methane formation. Another possible reaction that **complex3** can undergo is the elimination of HSCoM<sup>-</sup> where the SCoM<sup>2-</sup> ligand abstracts the proton attached to the C-ring nitrogen (Fig. 5-4, alt. 1). The activation barrier for this process is 21.4 kcal/mol, and the product of the reaction (**complex7**) is more stable by 37.1 kcal/mol.

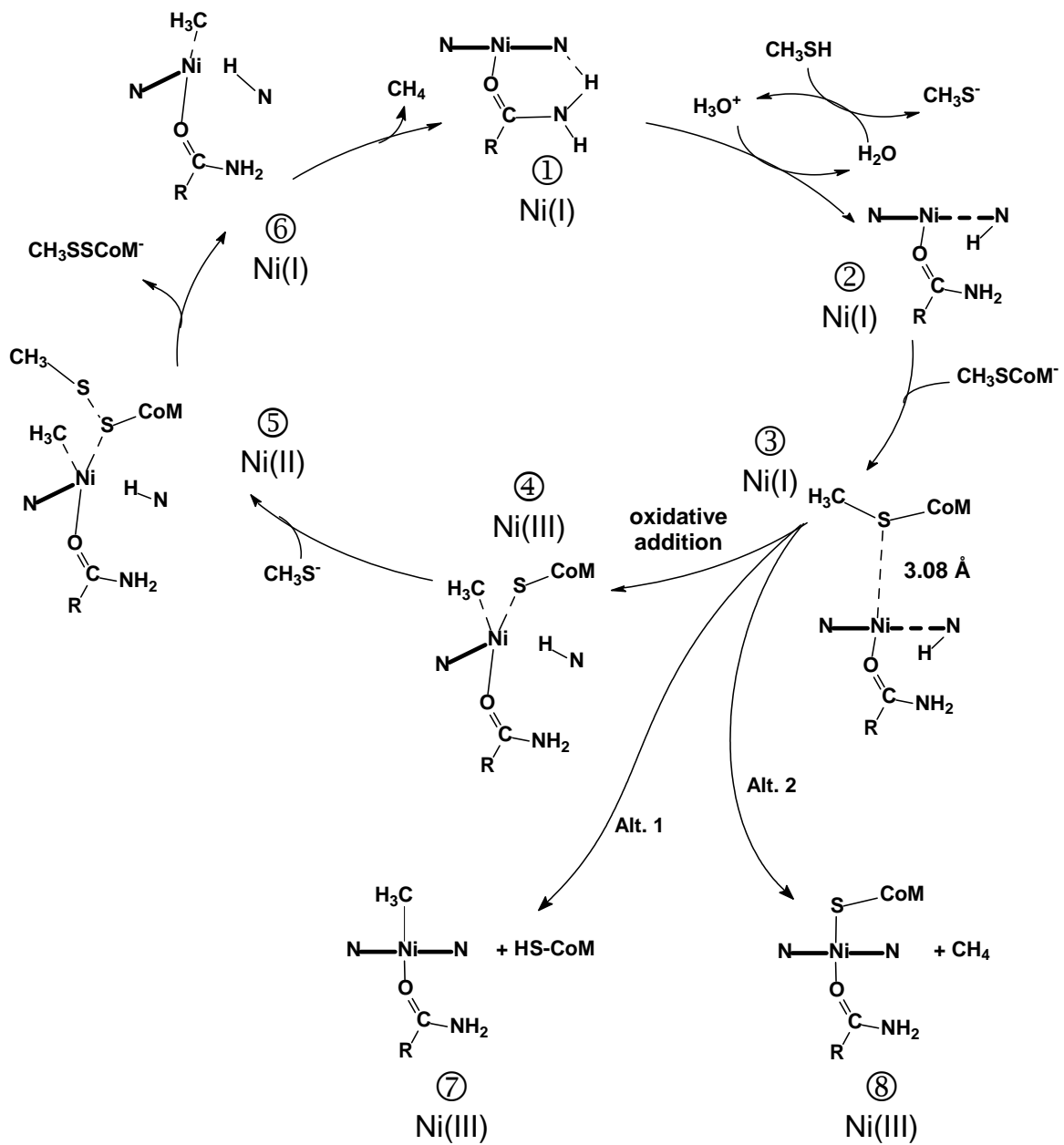


Figure 5-4: Proposed mechanism III

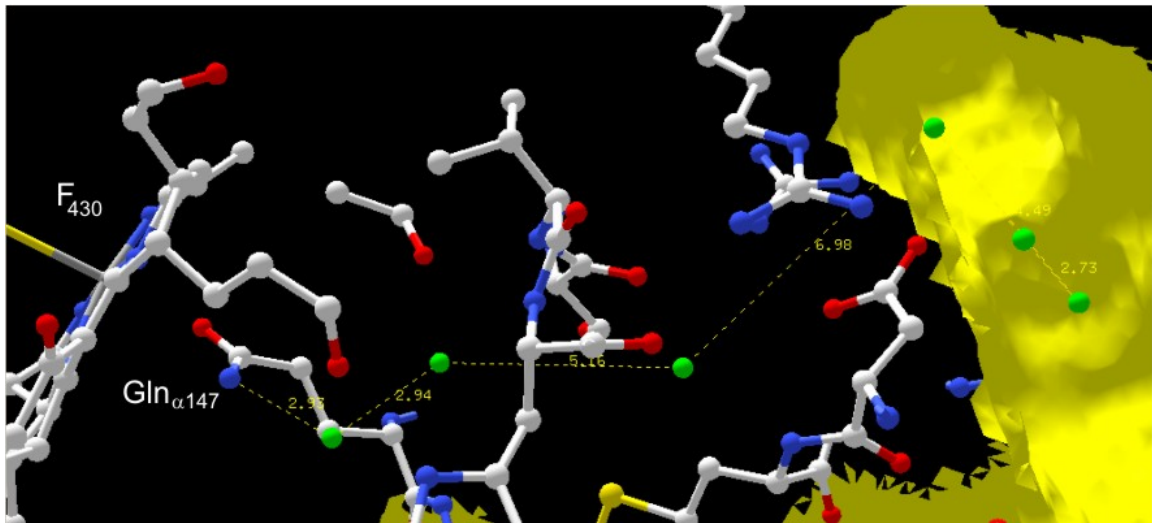


Figure 5-5: Water channel present in the crystal structure of MCR. The water molecules are represented as green spheres.

As mentioned before, freeze-quench experiments failed in trapping any reaction intermediates. Therefore no direct evidence is available to support this new hypothetical reaction mechanism. However, there is other evidence that seem to support this mechanism:

- (i) The detection of a Ni(III)-CH<sub>3</sub> species in MCR-BrMe supports the possible formation of such a species in this reaction mechanism (**complex 4 -6**).
- (ii) Figure 5-5 shows that there is a water channel that end very closely to the distal site of the F<sub>430</sub> ring. Since this channel is present on the distal site it never received much attention. There is no report about a possible function. Now we think this water channel may help with the proton transfer during the reactions. This new mechanism shows that the hydrogen for the protonation of the methyl group comes from the distal Gln<sup>147</sup>. Therefore to keep the reaction cycle going this proton has to be replenished. Although there is another water channel on proximal site of the F<sub>430</sub> ring, both this channel and the active site channel are blocked after coenzyme B is bound, and no proton can enter the active site from that direction. The distal water channel is a reasonable and convenient way to transfer protons to the active site.
- (iii) ENDOR studies show that there might be a Ni-H (or a N-H) species present in the MCRred2-rhombic form (J. Harmer, personal communication). The DFT calculations show that for the formation of a Ni-H bond the same energy is needed as for the formation of a N-H bond. In the model it would not make much difference if the protonation takes place on the Ni or a N of

F<sub>430</sub>. Protonation of a N of the F<sub>430</sub> ring could explain the other ENDOR data (Table 5-1) that shows that one nitrogen on the F<sub>430</sub> ring displays a very different coupling constant. It could indicate that this nitrogen is involved in this reaction.

- (iv) The DFT-based model (Fig. 5-7) predicts different outcomes of the reaction mechanism that seems to be in line with our observation of the formation of MCRox1 and an EPR-silent form under turn-over condition (Fig. 4-5). Alternate reaction 1 where HS-CoM and a Ni-CH<sub>3</sub> species is formed, could eventually result in the formation of an EPR-silent species. Alternate reaction 2 where methane is formed before coenzyme M reacts with CoB, results in the formation of a species that is identical to MCRox1.
- (v) At last, the back reaction of MCR-BrMe with coenzyme M shows that a reversible reaction is possible. According to the model a similar back reaction would occur with heterodisulfide. These experiments are still under way.

## REFERENCES

1. *IPCC Third Assessment Report.*
2. *IPCC Fourth Assessment Report.*
3. *Trace Gases: Current Observations, Trends, and Budgets. Climate Change 2001. United Nations Environment Programme.*
4. Telser, J., *Nickel in  $F_{430}$  Structure and Bonding*, 1998. **91**: p. 31-63.
5. Jaun, B., *Coenzym  $F_{430}$  aus Methan-Bakterien: Zusammenh nge zwischen der Struktur des hydroporphinoiden Liganden und der Redoxchemie des Nickelzentrums.* *Chimia*, 1994. **48**: p. 50-55.
6. Whitman, W.B., *Methanogenic bacteria.* The bacteria, 1985. **8**: p. 3-84.
7. Daniels, L., R. Sparling, and G.D. Sprott, *The bioenergetics of methanogenesis.* *Biochimica et Biophysica Acta*, 1984. **768**: p. 113-163.
8. Wolfe, R.S., *Unusual coenzymes of methanogenesis.* *Trends in Biochemical Sciences*, 1985. **10**(10): p. 396-399.
9. Jaun, B., H. Sigel, and A. Sigel, *Methane formation by methanogenic bacteria: Redox chemistry of coenzyme  $F_{430}$* , in *Metal ions in biological systems*. 1993, Marcel Dekker Inc.: New York. p. 287-337.
10. DiMarco, A.A., T.A. Bobik, and R.S. Wolfe, *Unusual Coenzymes of Methanogenesis.* *Annual Reviews of Biochemistry*, 1990. **59**: p. 355-394.
11. Hartzell, P.L. and R.S. Wolfe, *Comparative studies of component C from the methylreductase system of different methanogens.* *Systematic and Applied Microbiology* 1986. **7**(2-3): p. 376-382.
12. Wolfe, R.S., *My Kind of Biology.* *Annual Reviews of Microbiology*, 1991. **45**: p. 1-35.
13. Thauer, R.K., *Nickelenzyme im Stoffwechsel von methanogenen Bakterien.* *Biol.Chem.Hoppe-Seyler*, 1985. **366**: p. 103-112.

14. Thauer, R.K., *Biochemistry of methanogenesis: a tribute to Marjory Stephenson*. Microbiology, 1998. **144**: p. 2377-2406.
15. Ankel-Fuchs, D., et al., *Structure and function of methyl-coenzyme M reductase and of factor F<sub>430</sub> in methanogenic bacteria*. Systematic and Applied Microbiology, 1986. **7**: p. 383-387.
16. Deppenmeier, U., et al., *Reduced Coenzyme F<sub>420</sub>: Heterodisulfide Oxidoreductase, a Proton-Translocating Redox System in Methanogenic Bacteria*. Proceedings of the National Academy of Sciences of the United States of America, 1990. **87**: p. 9449-9453.
17. Lienard, T. and G. Gottschalk, *Cloning, sequencing and expression of the genes encoding the sodium translocating N<sub>5</sub>-methyltetrahydromethanopterin:coenzyme M methyltransferase of the methylotrophic archaeon Methanosarcina mazei Go1*. FEBS Letters, 1998. **425**(2): p. 204-208.
18. Lienard, T., et al., *Sodium ion translocation by N<sub>5</sub>-methyltetrahydromethanopterin: coenzyme M methyltransferase from Methanosarcina mazei Go1 reconstituted in ether lipid liposomes*. European journal of biochemistry / FEBS 1996. **239**(3): p. 857-864.
19. Won, H., et al., *F<sub>430</sub>-dependent biocatalysis in methanogenic archaeobacteria*. Comments on Inorganic Chemistry, 1993. **15**(1): p. 1-26.
20. Wackett, L.P., et al., *Methyl- S -coenzyme-M reductase: a nickel-dependent enzyme catalyzing the terminal redox step in methane biogenesis*, in *The Bioinorganic Chemistry of Nickel*. 1988, VCH Verlagsgesellschaft mbH: Weinheim, Germany. p. 249-274.
21. Hartzell, P.L. and R.S. Wolfe, *Requirement of the nickel tetrapyrrole F<sub>430</sub> for in vitro methanogenesis: reconstitution of methylreductase component C from its dissociated subunits*. Proceedings of the National Academy of Sciences of the United States of America, 1986. **83**(18): p. 5.
22. Halcrow, M.A. and G. Christou, *Biomimetic chemistry of nickel*. Chemical Reviews, 1994. **94**: p. 2421-2481.
23. Hausinger, P.R., *Nickel enzymes in microbes*. The Science of the total environment, 1994. **148**(2-3): p. 156-166.
24. Hausinger, P.R., ed. *Biochemistry of Nickel*. 1993, Plenum, New York, N. Y.
25. Walsh, C.T. and W.H. Orme-Johnson, *Nickel enzymes*. Biochemistry, 1987. **26**: p. 4901-4905.

26. Jaun, B.a.T., R.K., *Methyl-coenzyme M Reductase and Its Nickel Corphin Coenzyme F<sub>430</sub> in Methanogenic Archaea*. Met. Ions Life Sci., 2007. **2**: p. 323-356.
27. Smith, D.R., et al., *Complete genome sequence of Methanobacterium thermoautotrophicum ΔH: Functional analysis and comparative genomics*. Journal of Bacteriology, 1997. **179**(22): p. 7135-7155.
28. Diekert, G., et al., *Incorporation of 8 succinate per mol nickel into factors F<sub>430</sub> by Methanobacterium thermoautotrophicum* Archives of Microbiology, 1980. **128**: p. 256-262.
29. Ellefson, W.L., W.B. Whitman, and R.S. Wolfe, *Nickel-containing factor F<sub>430</sub> : Chromophore of the methylreductase of Methanobacterium* Proceedings of the National Academy of Sciences of the United States of America, 1982. **79**: p. 3707-3710.
30. Hoehler, T.M., et al., *Anaerobic methane oxidation by a methanogen-sulfate reducer consortium: geochemical evidence and biochemical considerations*, in *Microbiol growth on C<sub>1</sub> compounds*. 1996, Kluwer Academic Publishers: Dordrecht. p. 326-333.
31. Valentine, D.L. and W.S. Reeburgh, *New perspectives on anaerobic methane oxidation*. Environmental Microbiology, 2000. **2**(5): p. 477-484.
32. Shima, S. and R.K. Thauer, *Methyl-coenzyme M reductase and the anaerobic oxidation of methane in methanotrophic Archaea*. Current Opinion in Microbiology, 2005. **8**(6): p. 643-648.
33. Ellefson, W.L. and R.S. Wolfe, *Component C of the methylreductase system of Methanobacterium* Journal of Biological Chemistry, 1981. **256**(9): p. 4259-4262.
34. Grabarse, W., et al., *On the mechanism of biological methane formation: structural evidence for conformational changes in methyl-coenzyme M reductase upon substrate binding*. Journal of Molecular Biology, 2001. **309**: p. 315-330.
35. Klein, A., et al., *Comparative analysis of genes encoding methyl coenzyme M reductase in methanogenic bacteria*. Molecular and General Genetics, 1988. **213**: p. 409-420.
36. Ermler, U., et al., *Crystal structure of a 300 kDa methyl-coenzyme M reductase, the key enzyme of biological methane formation, at 1.45Å resolution*. Science, 1997. **278**: p. 1457-1462.

37. Rospert, S., et al., *Methyl-coenzyme M reductase preparations with high specific activity from H<sub>2</sub>-preincubated cells of Methanobacterium thermoautotrophicum* FEBS Letters, 1991. **291**(2): p. 371-375.
38. Rospert, S., et al., *Two genetically distinct methyl-coenzyme M reductases in Methanobacterium thermoautotrophicum strain Marburg and ΔH*. European Journal of Biochemistry, 1990. **194**: p. 871-877.
39. Shima, S., et al., *Crystallization and preliminary X-ray diffraction studies of methyl-coenzyme M reductase from Methanobacterium thermoautotrophicum* J.Biochem., 1997. **121**: p. 829-830.
40. Duin, E.C., et al., *Coordination and geometry of the nickel atom in active methyl-coenzyme M reductase from Methanothermobacter marburgensis as detected by X-ray absorption spectroscopy*. Journal of Biological Inorganic Chemistry, 2003. **8**: p. 141-148.
41. Duin, E.C., M.J. Warren, and A. Smith, *Role of coenzyme F<sub>430</sub> in methanogenesis*, in *Tetrapyrroles: their birth, life and death*. 2008, Landes Bioscience: Georgetown. p. Online.
42. Grabarse, W., et al., *Comparison of three methyl-coenzyme M reductases from phylogenetically distant organisms: unusual amino acid modification, conservation and adaptation*. Journal of Molecular Biology, 2000. **303**: p. 329-344.
43. Selmer, T., et al., *The biosynthesis of methylated amino acids in the active site region of methyl-coenzyme M reductase*. Journal of Biological Chemistry, 2000. **275**(6): p. 3755-3760.
44. Gunsalus, R.P. and R.S. Wolfe, *Methyl Coenzyme M Reductase from Methanobacterium thermoautotrophicum* Journal of Biological Chemistry, 1980. **255**(5): p. 1891-1895.
45. Nagle, D.P., Jr. and R.S. Wolfe, *Component A of the methyl coenzyme M methylreductase system of Methanobacterium : Resolution into four components*. Proceedings of the National Academy of Sciences of the United States of America, 1983. **80**: p. 2151-2155.
46. Ellefson, W.L. and R.S. Wolfe, *Role of component C in the methylreductase system of Methanobacterium* Journal of Biological Chemistry, 1980. **255**(18): p. 8388-8389.

47. Ankel-Fuchs, D. and R.K. Thauer, *Methane formation from methyl-coenzyme M in a system containing methyl-coenzyme M reductase, component B and reduced cobalamin*. European Journal of Biochemistry, 1986. **156**: p. 171-177.
48. Ellermann, J., et al., *The final step in methane formation*. European Journal of Biochemistry, 1988. **172**: p. 669-677.
49. Blaut, M. and G. Gottschalk, *Evidence for a chemiosmotic mechanism of ATP synthesis in methanogenic bacteria*. Trends in Biochemical Sciences, 1985. **10**: p. 486-489.
50. Kaesler, B. and P. Scheaheit, *Methanogenesis and ATP synthesis in methanogenic bacteria at low electrochemical proton potentials*. European Journal of Biochemistry, 1988. **174**: p. 189-197.
51. Ossmer, R., et al., *Immunocytochemical localization of component C of the methylreductase system in Methanococcus voltae and Methanobacterium thermoautotrophicum* Proceedings of the National Academy of Sciences of the United States of America, 1986. **83**: p. 5789-5792.
52. Mayer, F., et al., *Immunoelectron Microscopic Demonstration of ATPase on the Cytoplasmic Membrane of the Methanogenic Bacterium Strain Go1*. J Bacteriol. 1987. **169**(5): p. 2307-2309.
53. Lancaster, J.R., *A unified scheme for carbon and electron flow coupled to ATP synthesis by substrate-level phosphorylation in methanogenic bacteria*. FEBS Lett. , 1986. **199**: p. 12-18.
54. Jussofie, A., F. Mayer, and G. Gottschalk, *Methane formation from methanol and molecular hydrogen by protoplasts of new methanogenic isolates and inhibition by dicyclohexylcarbodiimide*. Arch. Microbiol. , 1986. **146**: p. 245-249.
55. Mayer, F., et al., *The methanoreductosome: a high-molecular-weight enzyme complex in the methanogenic bacterium strain Go1 that contains components of the methylreductase system*. Journal of Bacteriology, 1988. **170**(4): p. 1438-1444.
56. Gunsalus, R.P. and R.S. Wolfe, *ATP activation and properties of the methyl coenzyme M reductase system in Methanobacterium thermoautotrophicum* Journal of Bacteriology, 1978. **135**(3): p. 851-857.
57. Wackett, L.P., et al., *Substrate analogues as mechanistic probes of methyl-S-coenzyme M reductase*. Biochemistry, 1987. **26**: p. 6012-6018.

58. Ellermann, J., et al., *Methyl-coenzyme-M reductase from Methanobacterium thermoautotrophicum (strain Marburg)*. European Journal of Biochemistry, 1989. **184**: p. 63-68.
59. Goenrich, M., et al., *Probing the reactivity of Ni in the active site of methyl-coenzyme M reductase with substrate analogues*. Journal of Biological Inorganic Chemistry, 2004. **9**: p. 691-705.
60. Schonheit, P., J. Moll, and R.K. Thauer, Arch. Microbiol., 1979. **123**: p. 105-107.
61. Diekert, G., B. Klee, and R.K. Thauer, *Nickel, a component of factor F<sub>430</sub> from Methanobacterium thermoautotrophicum* Archives of Microbiology, 1980. **124**: p. 103-106.
62. Diekert, G., R. Jaenchen, and R.K. Thauer, *Biosynthetic evidence for a nickel tetrapyrrole structure of factor F<sub>430</sub> from Methanobacterium thermoautotrophicum* FEBS Letters, 1980. **119**(1): p. 118-120.
63. Jaenchen, R., G. Diekert, and R.K. Thauer, *Incorporation of methionine-derived methyl groups into factor F<sub>430</sub> by Methanobacterium thermoautotrophicum* FEBS Letters, 1981. **130**(1): p. 133-136.
64. Pfaltz, A., et al., *Zur Kenntnis des Faktors F<sub>430</sub> aus methanogenen Bakterien: Struktur des porphinoïden Ligandensystems*. Helvetica Chimica Acta, 1982. **65**(3): p. 828-865.
65. Jaun, B., *Coenzyme F<sub>430</sub> from methanogenic bacteria: Oxidation of F<sub>430</sub> pentamethyl ester to the Ni(III) form*. Helvetica Chimica Acta, 1990. **73**: p. 2209-2217.
66. Jaun, B. and A. Pfaltz, *Coenzyme F<sub>430</sub> from methanogenic bacteria: Reversible one-electron reduction of F<sub>430</sub> pentamethyl ester to the nickel(I) form*. Journal of the Chemical Society, Chemical Transactions, 1986: p. 1327-1329.
67. Holliger, C., et al., *A spectroelectrochemical study of factor F<sub>430</sub> nickel(III/I) from methanogenic bacteria in aqueous solution*. Journal of the American Chemical Society, 1993. **115**: p. 5651-5656.
68. Rospert, S., et al., *Substrate-analogue-induced changes in the nickel-EPR spectrum of active methyl-coenzyme-M reductase from Methanobacterium thermoautotrophicum* European Journal of Biochemistry, 1992. **210**: p. 101-107.
69. Albracht, S.P.J., et al., *A new EPR signal of nickel in Methanobacterium thermoautotrophicum* Biochimica et Biophysica Acta, 1986. **870**: p. 50-57.

70. Ragsdale, S.W., et al., *Biochemistry of methyl-CoM reductase and coenzyme F<sub>430</sub>*, in *Porphyrin Handbook*. 2003, Elsevier Science: San Diego. p. 205-228.
71. Telser, J., et al., *On the assignment of nickel oxidation states of the ox1, ox2 forms of methyl-coenzyme M reductase*. *Journal of the American Chemical Society*, 2000. **122**: p. 182-183.
72. Duin, E.C., et al., *Spectroscopic investigation of the nickel-containing porphinoic cofactor F<sub>430</sub>. Comparison of the free cofactor in the +1, +2 and +3 oxidation states with the cofactor bound to methyl-coenzyme M reductase in the silent, red and ox forms*. *Journal of Biological Inorganic Chemistry*, 2004. **9**: p. 563-576.
73. Craft, J.L., et al., *Spectroscopic and computational characterization of the nickel-containing F<sub>430</sub> cofactor of methyl-coenzyme M reductase*. *Journal of Biological Inorganic Chemistry*, 2004. **9**(1): p. 77-89.
74. Craft, J.L., et al., *Nickel oxidation states of F<sub>430</sub> cofactor in methyl-coenzyme M reductase*. *Journal of the American Chemical Society*, 2004. **126**: p. 4068-4069.
75. Albracht, S.P.J., et al., *Direct evidence for sulphur as a ligand to nickel in hydrogenase: an EPR study of the enzyme from Wolinella succinogenes enriched in <sup>33</sup>S*. *Biochimica et Biophysica Acta*, 1986. **874**: p. 116-127.
76. Mahlert, F., et al., *The nickel enzyme methyl-coenzyme M reductase from methanogenic archaea: in vitro interconversions among the EPR detectable MCR-red1 and MCR-red2 states*. *Journal of Biological Inorganic Chemistry*, 2002. **7**: p. 101-112.
77. Ma, L., *Spectroscopic characterization of nickel-containing F<sub>430</sub> and S-methyl coenzyme M reductase*. 1993, University of Georgia.
78. Eidsness, M.K., et al., *Structural diversity of F<sub>430</sub> from Methanobacterium thermoautotrophicum. A nickel X-ray absorption spectroscopic study*. *Journal of the American Chemical Society*, 1986. **108**: p. 3120-3121.
79. Shiemke, A.K., J.A. Shelnut, and R.A. Scott, *Coordination chemistry of F<sub>430</sub>*. *Journal of Biological Chemistry*, 1989. **264**(19): p. 11236-11245.
80. Furenlid, L.R., M.W. Renner, and J. Fajer, *EXAFS studies of nickel(II) and nickel(I) factor<sub>430</sub> M*. *Journal of the American Chemical Society*, 1990. **112**: p. 8987-8989.
81. Furenlid, L.R., et al., *Structural consequences of nickel versus macrocycle reductions in F<sub>430</sub> models: EXAFS studies of a Ni(I) anion and Ni(II) π anion radicals*. *Journal of the American Chemical Society*, 1990. **112**: p. 1634-1635.

82. Furenlid, L.R., et al., *EXAFS studies of Ni II, Ni I, and Ni I-CO tetraazamacrocycles and the crystal structure of (5,7,7,12,14,14-hexamethyl-1,4,8,11-tetraazacyclotetradeca-4,11-diene)nickel(I) perchlorate*. Journal of the American Chemical Society, 1991. **113**: p. 883-892.
83. Renner, M.W., et al., *Models of factor<sub>430</sub>. Structural and spectroscopic studies of Ni(II) and Ni(I) hydrophyrins*. Journal of the American Chemical Society, 1991. **113**: p. 6891-6898.
84. Mahlert, F., et al., *The nickel enzyme methyl-coenzyme M reductase from methanogenic archaea: in vitro induction of the nickel-based MCR-ox EPR signals from MCR-red2*. Journal of Biological Inorganic Chemistry, 2002. **7**: p. 500-513.
85. Goubeaud, M., G. Schreiner, and R.K. Thauer, *Purified methyl-coenzyme-M reductase is activated when the enzyme-bound coenzyme F<sub>430</sub> is reduced to the nickel(I) oxidation state by titanium(III) citrate*. European Journal of Biochemistry, 1997. **243**: p. 110-114.
86. Kreaer, M., et al., *A conspicuous nickel protein in microbial mats that oxidize methane anaerobically*. Nature, 2003. **426**: p. 878-881.
87. Moran, J.J., et al.,, Archaea, 2004. **1**: p. 303-309.
88. Shilov, A.E., et al.,, Dokl. Akad. Nauk, 1999. **367**: p. 557-559.
89. Bonacker, L.G., et al., *Properties of the two isoenzymes of methyl-coenzyme M reductase in Methanobacterium thermoautotrophicum* European Journal of Biochemistry, 1993. **217**: p. 587-595.
90. Ermler, U., *On the mechanism of methyl-coenzyme M reductase*. Dalton Trans., 2005: p. 3451-3458.
91. Berkessel, A., *Methyl-coenzyme M reductase: Model studies on pentadentate nickel complexes and a hypothetical mechanism*. Bioorganic Chemistry, 1991. **19**: p. 101-115.
92. Signor, L., et al., *Methane formation by reaction of a methyl thioether with a photo-excited nickel thiolate - A process mimicking methanogenesis in Archaea*. Chem.Eur.J., 2000. **6**(19): p. 3508-3516.
93. Ahn, Y., J.A. Krzycki, and H.G. Floss, *Steric course of the reduction of ethyl coenzyme M to ethane catalyzed by methyl coenzyme M reductase from Methanosarcina barkeri* Journal of the American Chemical Society, 1991. **113**: p. 4700-4701.

94. Hinderberger, D., et al., *A nickel-alkyl bond in an inactivated state of the enzyme catalyzing methane formation*. *Angewandte Chemie*, 2006. **45**: p. 3602-3607.
95. Jaun, B. and A. Pfaltz, *Coenzyme F<sub>430</sub> from methanogenic bacteria: Methane formation by reductive carbon-sulphur bond cleavage of methyl sulphonium ions catalysed by F<sub>430</sub> pentamethyl ester*. *Journal of the Chemical Society, Chemical Transactions*, 1988: p. 293-294.
96. Lin, S.K. and B. Jaun, *Coenzyme F<sub>430</sub> from methanogenic bacteria: Detection of a paramagnetic methylnickel(II) derivative of the pentamethyl ester by <sup>2</sup>H-NMR spectroscopy*. *Helvetica Chimica Acta*, 1991. **74**: p. 1725-1738.
97. Goenrich, M., et al., *Temperature dependence of methyl-coenzyme M reductase activity and of the formation of the methyl-coenzyme M reductase red2 state induced by coenzyme B*. *Journal of Biological Inorganic Chemistry*, 2005. **10**: p. 333-342.
98. Pelmeshnikov, V., et al., *A mechanism from quantum chemical studies for methane formation in methanogenesis*. *Journal of the American Chemical Society*, 2002. **124**(15): p. 4039-4049.
99. Pelmeshnikov, V. and P.E.M. Siegbahn, *Catalysis by methyl-coenzyme M reductase: A theoretical study for heterodisulfide product formation*. *Journal of Biological Inorganic Chemistry*, 2003. **8**(6): p. 653-662.
100. Horng, Y.C., D.F. Becker, and S.W. Ragsdale, *Mechanistic studies of methane biogenesis by methyl-coenzyme M reductase: evidence that coenzyme B participates in cleaving the C-S bond of methyl-coenzyme M*. *Biochemistry*, 2001. **40**: p. 12875-12885.
101. Finazzo, C., et al., *Coenzyme B induced coordination of coenzyme M via its thiol group to Ni(I) of F<sub>430</sub> in active methyl-coenzyme M reductase*. *Journal of the American Chemical Society*, 2003. **125**: p. 4988-4989.
102. Palmer, G. and L. Que, Jr., *Electron Paramagnetic Resonance of Metalloproteins*, in *Physical Methods in Bioinorganic Chemistry*. 2002, University Science Books: Sausalito, California. p. 121.
103. Brudvig, G.W., *Electron Paramagnetic Resonance Spectroscopy*, in *Methods in Enzymology*. 1995.
104. Pilbrow, J.R. and G.R. Hanson, *Electron Paramagnetic Resonance*. *Methods in Enzymology*, 1993. **227**: p. 330-352.
105. Carrington, A.e.a., *Introduction to Magnetic Resonance*. 1967, New York.

106. Weil, J.A., J.R. Bolton, and J.E. Wertz, *Electron Paramagnetic Resonance: elementary theory and practical applications*. 1995, New York / Wertz, J.E., Bolton, J.R. (1972) Chapman and Hall, New York: John Wiley & sons, inc.
107. Gordy, W.e.a., *Theory and Applications of Electron Spin Resonance*. 1980, New York.
108. Scott, R.A. and L. Que, Jr., *X-ray Absorption Spectroscopy*, in *Physical Methods in Bioinorganic Chemistry*. 2000, University Science Books: Sausalito, California. p. 465.
109. Feher, G., Phys. Rev., 1956. **103**: p. 834-835.
110. Eisenberger, P.a.p., P. S., J. Chem. Phys., 1967. **47**: p. 3327-3334.
111. Derose, V.J.a.H., B.M., *Protein Structure and Mechanism Studied by Electron Nuclear Double Resonance Spectroscopy*. Methods in Enzymology, 1995. **246**: p. 554-589.
112. Hoffman, B.M., *Electron nuclear double resonance (ENDOR) of metalloenzymes*. Accounts of Chemical Research, 1991. **24**: p. 164-170.
113. Swartz, H.M., et al., *Biological Applications of Electron Spin Resonance*. 1972, New York: Wiley-Interscience.
114. Atherton, N.M., *Electron Spin Resonance*. 1973, New York: Wiley.
115. Dorio, M.M.a.F., J. H., *Multiple Electron Resonance Spectroscopy*. 1979, New York: Plenum.
116. Schweiger, A., *Structure and Bonding*. Vol. 51. 1982. 1-128.
117. Abragam, A.a.P., M. H. L., Proc. R. Soc. Lond. A, 1951. **205**: p. 135-153.
118. Van Doorslaer, S. and E. Vinck, *The strength of EPR and ENDOR techniques in revealing structure-function relationships in metalloproteins*. Physical Chemistry Chemical Physics, 2007. **9**(33): p. 4620-4638.
119. Gunsalus, R.P., J.A. Romesser, and R.S. Wolfe, *Preparation of coenzyme M analogues and their activity in the methyl coenzyme M reductase system of Methanobacterium thermoautotrophicum* Biochemistry, 1978. **17**(12): p. 2374-2377.

120. Deakin, H., M.G. Ord, and L.A. Stocked, *Glucose 6-phosphate-dehydrogenase Activity and Thiol Content of Thymus Nuclei from Control and X-irradiated Rats*. *Biochemistry J*, 1963. **89**: p. 296.
121. Ellman, G.L., *Arch. Biochem. Biophys.*, 1959. **82**: p. 70-77.
122. Riddles, P., R. Blakeley, and B. Zerner, *Reassessment of Ellman's reagent*. *Methods Enzymol*, 1983. **91**: p. 49-60.
123. Jocelyn, P.C., *Spectrophotometric assay of thiols*. *Methods in Enzymology*, 1987. **143**: p. 44-67.
124. Hu, M.L., *Measurement of protein thiol groups and glutathione in plasma*. *Methods Enzymol*, 1994. **233**: p. 380-385
125. Bulaj, G., T. Kortemme, and D.P. Goldenberg, *Biochemistry*, 1998. **37**: p. 8965-8972.
126. Schoenheit, P., J. Moll, and R.K. Thauer, *Growth parameters ( $K_s$ ,  $\mu_{max}$ ,  $Y_s$ ) of methanobacterium thermoautotrophicum*. *Archives of Microbiology*, 1980. **127**: p. 59-65.
127. Bradford, M., *A rapid and sensitive for the quantitation of microgram quantities of protein utilizing the principle of protein-dye binding*. *Analytical Biochemistry*, 1976. **72**: p. 248-254.
128. Stoscheck, C., *Quantitation of Protein*. *Methods in Enzymology*, 1990. **182**: p. 50-69.
129. Hanson, R.S. and T.E. Hanson, *Methanotrophic bacteria*. *Microbiological Reviews*, 1996. **60**: p. 439-471.
130. Beinert, H. and S.P.J. Albracht, *New insights, ideas and unanswered questions concerning iron-sulfur clusters in mitochondria*. *Biochimica et Biophysica Acta*, 1982. **683**: p. 245-277.
131. *Merck Index, 11th Edition, 5951*.
132. Duin, E., B. Jaun, and J. Harmer, *manuscript in preparation*.
133. Yang, N., et al., *Formation of a Nickel-Methyl Species in Methyl-Coenzyme M Reductase, an Enzyme Catalyzing Methane Formation*. *Journal of the American Chemical Society*, 2007. **129**(36): p. 11028-11029.

134. Kunz, R.C., Y.C. Horng, and S.W. Ragsdale, *Spectroscopic and kinetic studies of the reaction of bromopropanesulfonate with methyl-coenzyme M reductase*. Journal of Biological Chemistry, 2006. **281**(45): p. 34663-34676.
135. Holliger, C., et al., *Methyl-coenzyme M reductase of Methanobacterium thermoautotrophicum  $\Delta H$  catalyzes the reductive dechlorination of 1,2-dichloroethane to ethylene and chloroethane*. Journal of Bacteriology, 1992. **174**(13): p. 4435-4443.
136. Stubbe, J. and W.A. Van der Donk, *Protein radicals in enzyme catalysis*. Chemical Reviews, 1998. **98**: p. 705-762.
137. Wagner, A.F.V., et al., *The free radical in pyruvate formate-lyase is located on glycine-734*. Proceedings of the National Academy of Sciences of the United States of America, 1992. **89**(3): p. 996-1000.
138. Knappe, J. and A.F. Wagner, *Stable glycy radical from pyruvate formate-lyase and ribonucleotide reductase (III)*. Adv. Protein Chem., 2001. **58**: p. 277-315.
139. Young, P., et al., *Bacteriophage T4 anaerobic ribonucleotide reductase contains a stable glycy radical at position 580*. Journal of Biological Chemistry, 1996. **271**(34): p. 20770-20775.
140. Carole Duboc-Toia, et al., *Very High-Field EPR Study of Glycyl Radical Enzymes*. Journal of the American Chemical Society, 2003. **125**(1): p. 38-39.
141. Telser, J., et al., *Cryoreduction of methyl-coenzyme M reductase: EPR characterization of forms, MCR oxI and MCR redI* Journal of the American Chemical Society, 2001. **123**(25): p. 5853-5860.
142. Duin, E.C. and M.L. McKee, *A New Mechanism for Methane Production from Methyl-Coenzyme M Reductase As Derived from Density Functional Calculations*. Journal of Physical Chemistry B, 2008. **112**(8): p. 2466-2482.